UNIVERSITY OF CALGARY

Multicomponent seismic analysis from an oil sands field, Alberta, Canada

by

Robert James Gunning

A THESIS

SUBMITTED TO THE FACULTY OF GRADUATE STUDIES

IN PARTIAL FULFILMENT OF THE REQUIREMENTS FOR THE

DEGREE OF MASTER OF SCIENCE

GRADUATE PROGRAM IN GEOLOGY AND GEOPHYSICS

CALGARY, ALBERTA

June, 2017

Abstract

Seismic acquisition in the Athabasca Oil Sands increasingly utilizes three-component geophones. However, the vertical component data are generally are processed and interpreted, but the horizontal component data are often left unprocessed. In this project, we demonstrate that there are many geological interpretations that can be improved through joint analysis and inversion of the vertical and radial geophone component data. In this study, the processing of the vertical and radial geophone component data from an Alberta oil sands field yielded good quality PP and PS seismic volumes. The main reservoir interval, the McMurray Formation, was found to have marginal reflection quality on the PP seismic data and good reflection quality on the PS seismic data. Post-stack, pre-stack and joint inversion provided data volumes which, when correlated to geological control and yielded spatial distributions of good reservoir facies.

Acknowledgements

My graduate supervisor Dr. Don Lawton deserves immense thanks for his leadership and teaching. I improved my technical abilities in seismic methods and I learned both writing and presentation skills through Don’s guidance and support.

I would like to thank CREWES staff, especially Helen Isaac and Laura Baird; Helen for her technical support and work on my projects and Laura for always having an open door. I appreciate my fellow CREWES students for topical conversations and friendship. CREWES industrial sponsors and the Natural Science and Engineering Research Council of Canada made this project and my graduate degree financially viable.

I am grateful for the opportunity to use industrial seismic datasets from the providing company Canadian Natural Resourced Limited. Software license providers: SeisWare, CGG Hampson-Russell, Schlumberger Vista, Halliburton ProMAX and Matlab deserve special recognition.

Table of Contents

List of Figures and Illustrations

List of Symbols, Abbreviations and Nomenclature

Symbol	Definition
°API	American Petroleum Institute gamma ray unit
°C	Degree Celsius
°	Degrees
~	Roughly
$\approx$	Approximately
α	P-wave velocity
β	S-wave velocity
Δt_{pp}	PP travel time
Δt_{ps}	PS travel time
θ	Angle
ν	Poisson Ratio
ρ	Density
φ	Angle
ϕ_D	Density porosity
ϕ_N	Neutron porosity
Ωm	Ohm meters
1D	One dimensional
2D	Two dimensional
3D	Three dimensional
AVO	Amplitude versus offset
Bbl	Barrel
Bbl/d	Barrel per day
CSS	Cyclic steam stimulation
CDP	Common depth point
cP	Centipoise
CMP	Common midpoint
CHOPS	Cold heavy oil production with sand
cos	Cosine
dB	Decibel
E	Young's modulus
Fm	Formation
g/cm^3	Grams per cubic centimeter
GLI	Generalized linear inversion
Gp	Group
GPa	Gigapascal
GR	Gamma ray
HTI	Horizontal transverse isotropy
Hz	Hertz
ILD	Deep induction log
kg	Kilogram
km	Kilometer
km^2	Square Kilometer
m	Meter
ms	Milliseconds

m/s	Meters per second
N	North
NMO	Normal Moveout
PP	Seismic wave reflection with downgoing P wave and upgoing P wave
PNN	Probabilistic neural network
PS	Seismic wave reflection with downgoing P wave and upgoing S wave
P-wave	Compressional seismic wave
RMS	Root mean square
R_{pp}	PP reflection coefficient
R_{ps}	PS reflection coefficient
R-T	Radial trace domain
s	Second
SAGD	Steam-assisted gravity drainage
sin	Sine
S-wave	Shear seismic wave
TTI	Tilted transverse isotropy
TVD	True vertical depth
VTI	Vertical transverse isotropy
V_p	P wave velocity
V_p/V_s	P to S velocity ratio
V_s	S wave velocity

CHAPTER 1: INTRODUCTION

1.1 Project motivation

Total Canadian oil production was 3.7 million bbl/d in 2014, forecast to grow to 5.3 million bbl/d by 2030 (Canadian Association of Petroleum Producers, 2015). Oil sands production makes up the majority of Canada's oil production at 2.2 million bbl/d, which is 59% of total oil production (Canadian Association of Petroleum Producers, 2015). Proven recoverable crude oil reserves in Canada were 172 billion barrels in 2015, of which 95% are in the oil sands (Energy Information Administration, 2007; 2015). The overwhelming majority of oil production growth will come from Alberta's oil sands; 1.8 million bbl/d is predicted to be added to oil sands production by 2030 (Canadian Association of Petroleum Producers, 2015). The oil sands resources of Canada are either surface mineable, or produced in-situ. In-situ production generally is used for reservoirs deeper than 80 m. Steam assisted gravity drainage (SAGD) and cyclic steam stimulation (CSS) are thermal enhanced oil recovery methods commonly used in the oil sands. In this project, multicomponent seismic reflection data are used to characterize an oil sands reservoir before in-situ thermal oil production.

Three-component seismic data are an effective tool for understanding subsurface conditions in the Athabasca region (Isaac, 1996; Stewart et al., 1999; Stewart et al., 2003; Gray et al., 2006; Kelly, 2012; Gray et al, 2016). Much of the seismic processing in this study follows from the work of Isaac (1996) and Kelly (2012). Both Isaac (1996) and Kelly (2012) processed multicomponent seismic data from the Northeast region of the Western Canada Sedimentary basin. Processing flows followed the procedures described by Margrave, (2006) and Yilmaz, (2001). Gray et al. (2006) predicted the concentration of non-reservoir shale facies in the Athabasca Oil Sands using multicomponent 3D seismic data. A similar application of multicomponent interpretation and inversion is used in this project in an attempt to understand the distribution of mudstones within the main reservoir interval. Some of the applications of converted-wave seismic data proposed by Stewart et al. (2003), include: imaging through gas chimneys, enhanced fault detection, improved near surface resolution, imaging interfaces with low P-impedance contrasts, lithology determination and monitoring. In the oil sands, the two most useful of these applications are imaging interfaces with low P-impedance contrasts and lithology determination.

1.2 Thermal oil sands extraction

Producing hydrocarbons from the oil sands reservoirs is not a trivial process. The saturating fluid is primarily bitumen, a dense, high viscosity fluid that cannot be produced by means of primary production. Two main enhanced oil recovery methods are utilized in the oil sands: SAGD and CSS. In SAGD oil production, two horizontal wellbores are drilled, one 5-10 meters above the other. Steam is injected into the upper wellbore and water emulsified with bitumen is produced from the lower wellbore (Figure 1-1). SAGD operations are optimal where reservoirs are relatively uniform, thick, unconsolidated sands with little to no shale interbedding. CSS utilizes a single wellbore with an injection phase and a production phase. In CSS, steam is injected into the reservoir and after heat soaking and viscosity reduction, water-bitumen emulsion is produced from the same wellbore. CSS is colloquially called the “huff and puff,” method. CSS oil production is ideal in lower quality or thinner reservoir conditions, where shale interbeds and heavily brecciated clastics exist. CSS methods are used in both vertical and horizontal wells, whereas SAGD wells are always horizontal. Both methods require a competent sealing “caprock,” to prevent fluid escape upwards, above the reservoir.

Understanding the distribution and quality of the reservoir rock and caprock is very valuable in thermal oil sands operations. Traditionally, PP seismic data are used to study the oil sands. Converted-wave (PS) seismic data add a second independent dataset to interpret jointly with the PP data. Converted-wave data are useful in several ways in the oil sands: imaging through gas, imaging interfaces with low P-impedance contrast but high S-impedance contrast, improved shallow section imaging and discrimination of lithology through V_p/V_s analysis (Stewart et al., 2000; Gray et al., 2006).

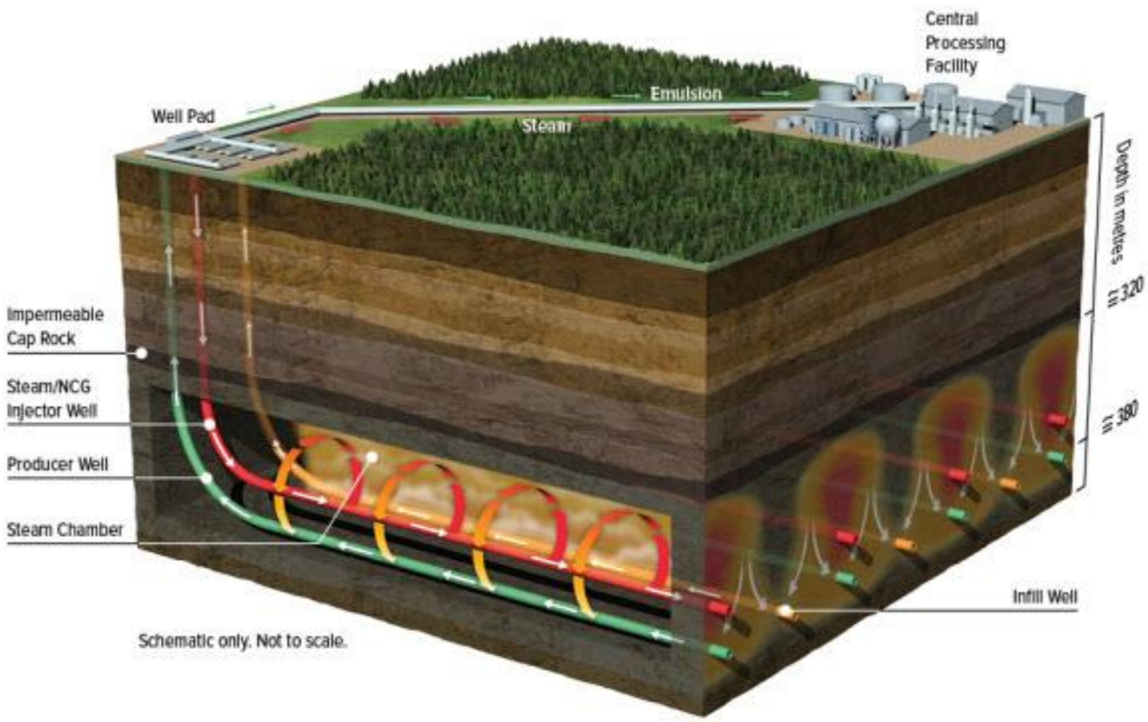

Figure 1-1. SAGD field operation schematic (from MEG Energy Corp., 2016).

1.3 Overview of converted-wave seismic exploration

Conventional PP seismic data are recorded with vertical component geophones. In order to recover the complete vector wavefield, three-component geophones are used, for converted-wave surveys. Three orthogonal geophone elements record all particle motion in 3 dimensions. In the field, the geophones all have same orientation such that the two horizontal elements all have the same frame of reference. The Zoeppritz equations describe how seismic energy is distributed at an impedance interface (Figure 1-2). An incident P-wave yields 4 modes: a reflected P-wave, a reflected S-wave, a transmitted P-wave and a transmitted S-wave. In converted-wave exploration a specific wave mode conversion is studied. A downward propagating P wave that converts to an S wave upon reflection is imaged in converted-wave acquisition (Figure 1-3). In PP seismic data analysis, 1D synthetic seismograms are commonly used to determine which seismic reflection events represent geological formation boundaries. Lawton and Howell (1992) developed a method to create 1D synthetic seismograms, for converted-waves, from compressional, shear sonic and density logs.

In multicomponent seismic processing, the two horizontal geophone elements are mathematically rotated such that one is oriented in the source-geophone direction and the other one is perpendicular, yielding radial and transverse traces. In isotropic media, only the radial component will contain converted S-wave data. This effect is due to a polarized shear wave being generated from an incident P wave (Figure 1-2). In anisotropic media, shear waves will have more than a single polarization. In transversely isotropic media (Figure 1-4), there will be two shear polarizations: one fast and one slow. If a polarized shear wave in an isotropic medium enters a transversely isotropic medium it will split into the fast and slow shear modes (Ando et al., 1980). For shear waves travelling in the x_3 direction in Figure 1-4: the fast shear will have particle motion in the x_2 direction and the slow shear will have particle motion in the x_1 direction. There are two common types of anisotropic media in sedimentary basins: vertical transverse isotropy (VTI) and horizontal transverse isotropy (HTI). Layer-cake sedimentary rocks are considered VTI at relatively long wavelengths. Unidirectional fracture networks or unequal horizontal stresses are examples of HTI in rocks (Figure 1-4). There exists also tilted transverse isotropy (TTI), which contains all non-vertical and non-horizontal transverse isotropic media (eg. dipping beds).

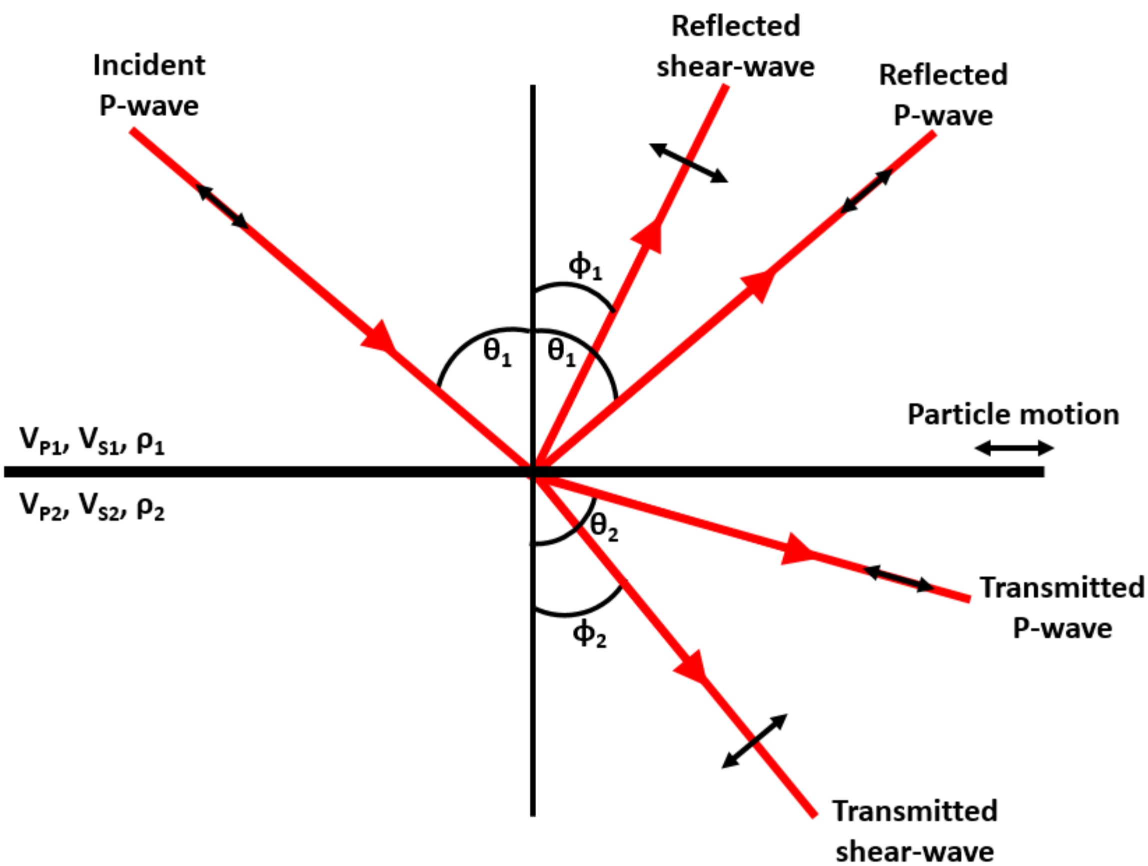

Figure 1-2. Mode conversions for an incident P wave at an acoustic impedance interface

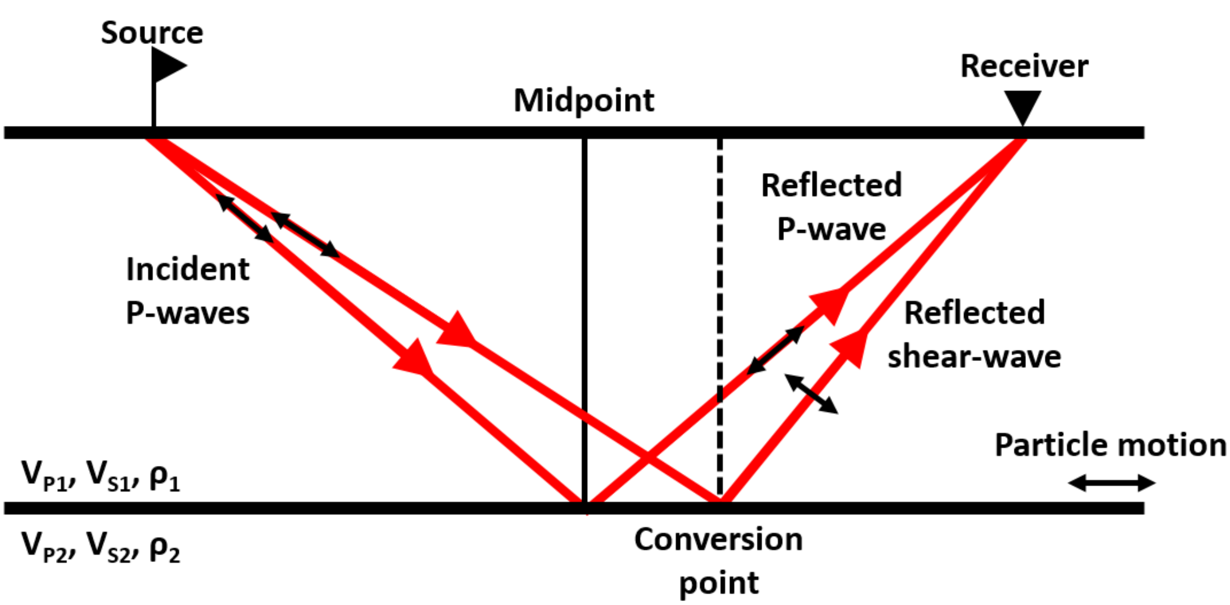

Figure 1-3. Reflection geometries for a PP raypath and a PS raypath.

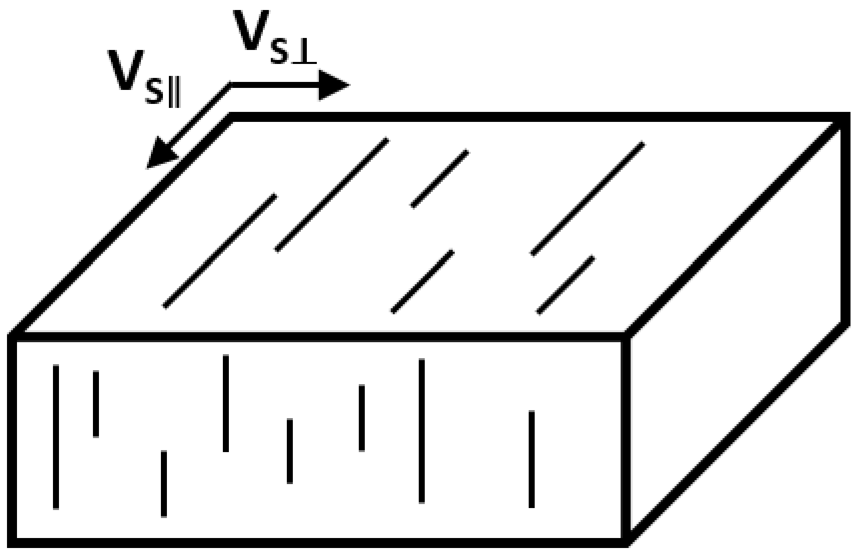

Figure 1-4. Schematic of transversely isotropic media, specifically HTI media.

1.4 Study area and data

An extensive set of geological and geophysical data were made available for this project. A 17 km^2 3D seismic volume, acquired in 2013, from the Athabasca region in Northeast Alberta is the primary dataset. The raw vertical, inline and crossline geophone components as well as a professionally processed PP seismic dataset were available. The survey was acquired with an orthogonal survey design; the source lines were oriented East-West with 125 m spacing and the receiver lines were oriented North-South, also with 125 m spacing. Sources and receivers were placed at 25 m intervals along source lines and receiver lines. The 3D survey utilized ¼ kg dynamite sources buried at 6 m. 648 channels were live for 4 seconds for each source. No oil sands production has yet occurred within the project area. The main depth of interest is between 350m and 500m.

Within the area covered by 3D seismic data there exist 14 vertical wells (Figure 1-5), all 14 wells have a standard suite of well logs including: compressional sonic, density, gamma ray and deep resistivity. Three of the wells have shear sonic logs. Other well logs common in the project dataset include: Neutron porosity, caliper, photoelectric effect, spontaneous potential and other depth-of-investigation resistivity logs. Sonic and density logs were used to tie geological information to geophysical logs through synthetic seismograms. Gamma ray logs were used mainly as a lithological indicator, generally used to discriminate sands from shales. Reservoir fluids were determined by resistivity logs as well as neutron and density porosity logs.

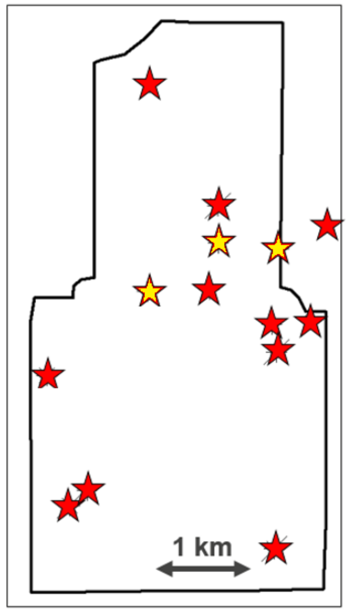

Figure 1-5. 3D seismic data outline and well log positions. Yellow and red stars indicate dipole sonic log positions.

1.5 Thesis objectives

Characterization of the main hydrocarbon reservoir, the McMurray Formation, through the joint processing and interpretation of the multicomponent 3D seismic volume is a primary goal of this research. Making detailed conclusions, relevant to the hydrocarbon system, from the processed P-P and P-S seismic volumes as well as inversion volumes is an objective. I also strive to prove that it is worthwhile to acquire, process and interpret converted wave seismic data in an oil sands play.

1.6 Software

Schlumberger's Vista was used as the main processing software, with some processing completed in Halliburton's ProMAX software. Seismic interpretation was done in SeisWare, CGG Hampson-Russell and Matlab. The Microsoft Office software: Word, Excel and PowerPoint were used for preparing figures, processing text documents and analyzing data.

CHAPTER 2: ATHABASCA GEOLOGY

The oil sands deposits of Alberta house 40% of the global bitumen supply, with bitumen-in-place totaling over 1.7 trillion barrels (Masson and Remillard, 1995). Daily production from in situ and surface mineable oil sands operations was 2.2 million barrels per day in 2014 with a predicted growth of 168 000 barrels per day annually through 2019 (Canadian Association of Petroleum Producers, 2015). Alberta's oil sands resource will be the primary driver in the growth of Canada's hydrocarbon production industry. The three main oil sands deposits are the Peace River oil sands, the Cold Lake oil sands and the Athabasca Oil sands (Figure 2-1).

Figure 2-1. Location of Alberta's bituminous sand deposits (from Hein et al., 2001).

2.1 Stratigraphy and sedimentation

There exist three main sedimentary sequences in the Athabasca oil sands. Paleozoic carbonates, shales and evaporites, Cretaceous sands and shales and Quaternary glacial and fluvial sediments make up the make up the sedimentary package. Figures 2-2 and 2-3 show the stratigraphic column for the Western Canada Sedimentary Basin in the Athabasca oil sands subsurface.

The lowermost stratigraphic units of interest are the Devonian Beaverhill Lake and Elk Point groups (Figures 2-2 and 2-3). These unit lie beneath the Pre-Cretaceous Unconformity and are made up of carbonates, evaporites and shales. These Devonian-aged units subcrop as an angular unconformity below the Cretaceous clastic rocks. The pre-cretaceous units underwent structural deformation and karstification related to the dissolution of the Prairie Evaporites (Schneider et al., 2012). The top of the Beaverhill Lake Group exhibits topographic variability. Post-Devonian erosion resulted in complex pre-McMurray topography (Schneider et al., 2012). The topography of the McMurray-Beaverhill Lake interface has a significant impact on the thickness and structure of the McMurray Formation, which is the primary bitumen reservoir in this hydrocarbon system.

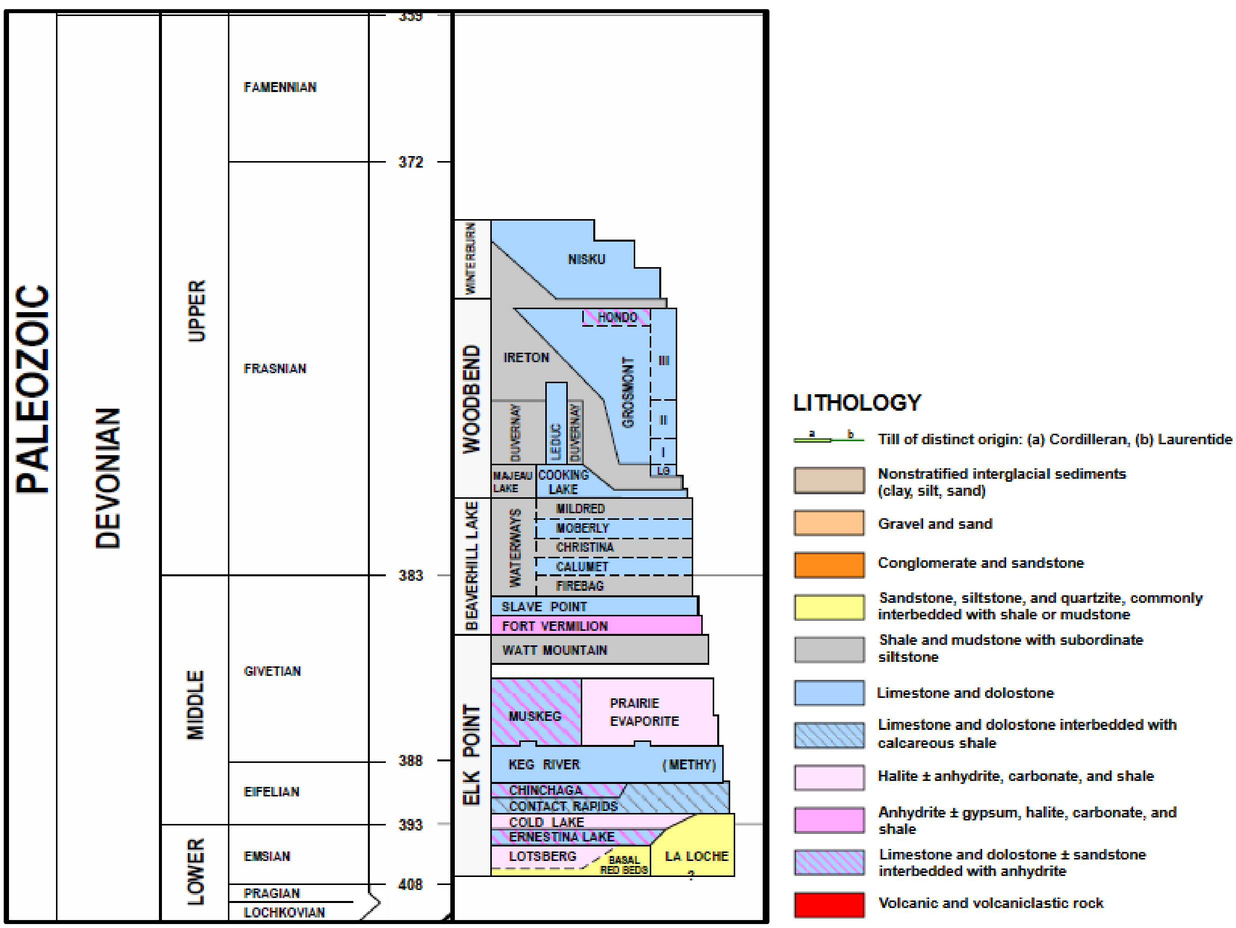

Figure 2-2. Devonian stratigraphy in Northeast Alberta (from Alberta Geological Survey, 2015).

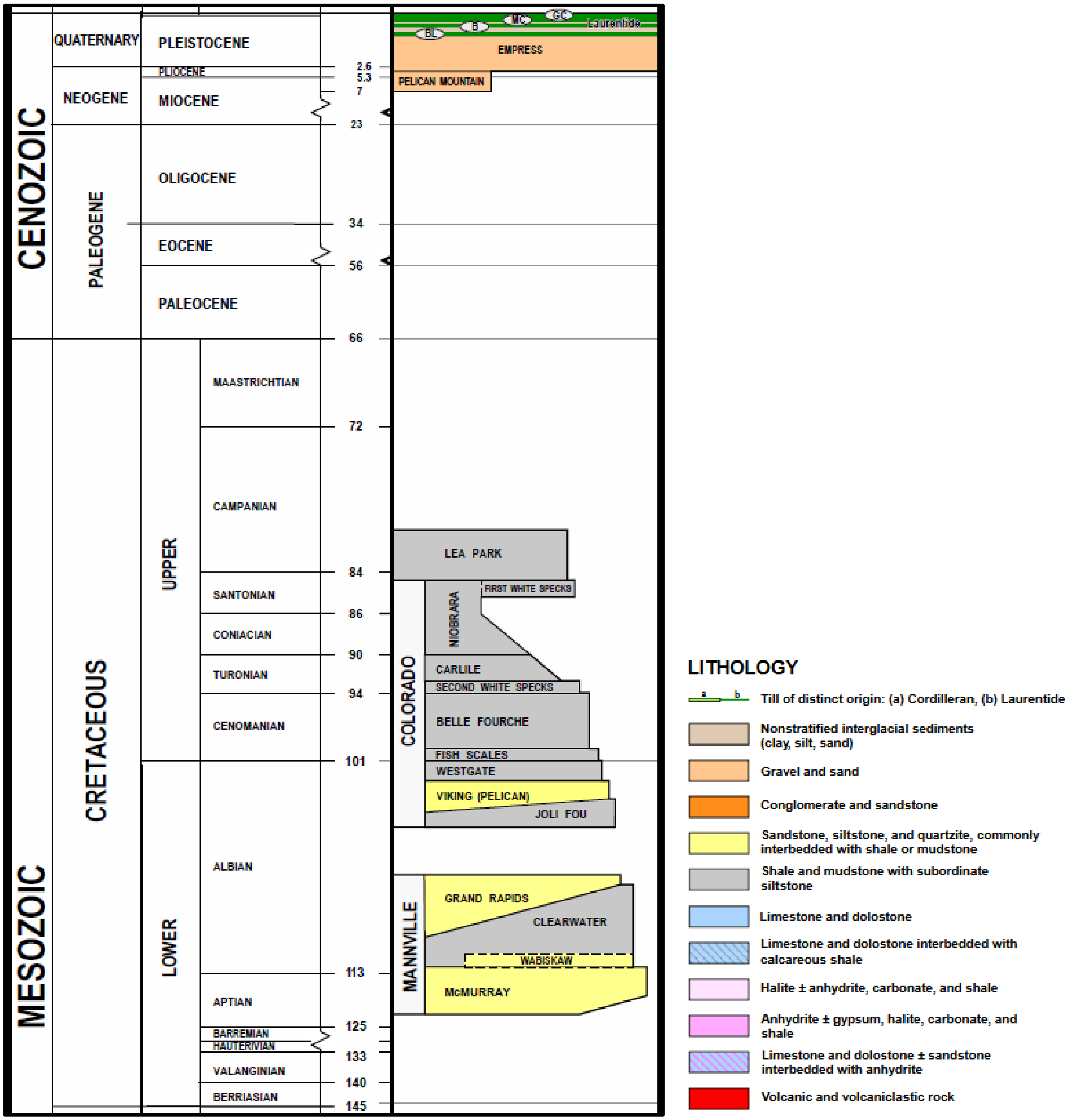

Figure 2-3. Cretaceous and Cenozoic stratigraphy in Northeast Alberta (from Alberta Geological Survey, 2015).

Above the Pre-Cretaceous Unconformity are the Cretaceous Mannville and Colorado Group strata, which in the Athabasca area are made up entirely of sandstones and shales and some of the units in these clastics are unconsolidated. The McMurray Formation, at the base of the

Mannville Group, is an unconsolidated Aptian reservoir sandstone. These sediments accumulated in incised valleys that were formed by fluvial processes and subsequently transgressed by marginal-marine environments during an early Cretaceous sea-level rise (Gingras and Rokosh, 2004).

Traditionally the McMurray Fm is separated in to three stratigraphic sequences, namely the McMurray A, B and C, also known as the Lower, Middle and Upper McMurray. The Lower McMurray is generally medium to coarse grained, massive appearing to crudely cross-bedded and contains no ichnofossils and is fluvial in nature (Gingras and Rokosh, 2004). While the Lower McMurray contains no ichnofossils, the Middle McMurray contains brackish water trace fossils (Pemberton et al., 1982). Inclined heterolithic stratification (IHS) dominates the Middle McMurray where deposition occurred on tidally influenced point bars (Gingras and Rokosh, 2004). The Upper McMurray has a more marine character, interpreted as low energy shorefaces and small deltaic systems (Gingras and Rokosh, 2004). A modern depositional analogue for the McMurray Formation is the Ganges Delta in Bangladesh and India (Figure 2-4). An analogous depositional condition to the Lower McMurray would be the more inland sedimentation occurring in the Northern part of Figure 2-4. The Upper and Middle McMurray would be more closely represented by the estuarine component of the Ganges Delta.

Figure 2-4. The Ganges Delta, a marginal marine depositional analogue to the McMurray Formation (from Google maps, 2016).

Conformably above the McMurray Formation lies the Wabiskaw Member of the Clearwater Formation. The Wabiskaw member is a fine-grained, well sorted glauconitic sandstone with interbedded shales, including a shale unit separating the Wabiskaw from the underlying McMurray Formation (Glass, 2009). The remainder of the Clearwater Formation, in the Athabasca Oil Sands, consists of soft black and grey mudstones, with interbedded grey sands (Glass, 2010). The extensive shales in the Clearwater Formation act as regional baffles to vertical fluid flow. These shales are colloquially known as the caprock to SAGD operations in the McMurray Formation. In the project area the Clearwater Formation, including the Wabiskaw member, has a thickness of approximately 50 m.

The uppermost unit of the Mannville Group in the project area is the Grand Rapids Formation, made up of is a series of coarsening upward shoreface sequences with incised channels containing brackish sediments (Baturin-Pollock, 2010). Sandstones of the Grand Rapids Formation are much more porous and permeable than the underlying Clearwater Formation shales. The Grand Rapids Formation has a thickness of approximately 100 m in the project area.

The Cretaceous Colorado Group, bounded above and below by unconformities, is the uppermost Mesozoic unit in the rock column in the Athabasca region. The Colorado Group is made up of almost entirely mudstone with thin interbedded sandstone and conglomerate sequences (Leckie et al., 1994). In the Athabasca region the Colorado Group is variably eroded, with some areas missing the Colorado Group sediments entirely. In the project area, the Fish Scales, Westgate, Viking and Joli Fou Formations are present. In other parts of the Western Canadian Sedimentary Basin the Colorado group is economically productive; for example the Cardium and Dunvegan sandstones are world class oil reservoirs.

Cenozoic sediments make up the shallow overburden in the Athabasca Oil Sands. These sediments are predominantly unconsolidated fluvial and glacial in nature and are over 300 m thick in some places (Andriashek, 2003). The glacial sequences present hindrances in seismic exploration, as propagating compressional and shear waves through these unconsolidated sediments is challenging. The large variability in seismic velocities in the Tertiary/Quaternary drift create large statics issues in processing. However, these processing challenges can be adequately mitigated and high quality seismic volumes are generated. Prior to the onset of glaciation in the Quaternary, regionally extensive fluvial systems deposited coarse grained sands and gravels in the

Athabasca region. These fluvial sediments are named the Empress Formation. A change from coarse fluvial sediments to lacustrine silt and mud occurs during the first glaciation (Andriashek, 2003). As the first Laurentide glacier advanced, sediment transport was blocked, leaving the lacustrine sequences in the early glacial period. The fine-grained lacustrine sediments are overlain by glacial outwash sands and gravels (Andriashek, 2003). There are four distinct glacial till cycles in the Quaternary Drift sequence in the Athabasca region (Andriashek, 2003).

2.2 Regional geology and hydrocarbon system

The hydrocarbons present in the Athabasca oil sands are thought to have been generated by the Exshaw Shale to the southwest where they outcrop near Exshaw, Alberta (Hein et al., 2001). Hydrocarbon generation is associated with the Laramide orogeny during Tertiary time. The oil sands reservoirs show very little evidence of diagenesis and there are assumed to never have been buried deeply (Hein et al., 2001). These reservoirs in the Athabasca region are primarily the McMurray Formation and to a lesser extent the Wabiskaw Member of the Clearwater Formation. These reservoirs are bounded above by the remainder of the Clearwater Formation, the Grand Rapids Formation and Colorado group strata, which act as regional seals. A cross section (Figure 2-5) across Alberta from Southwest to Northeast reveals the position of the oil sands with respect to the Canadian Rocky Mountains and the long hydrocarbon migration pathways. Directly beneath the bituminous sand reservoirs in the Athabasca region lie the Devonian and Mississippian carbonates. The large unconformity between the clastic reservoirs and carbonates, known as the Pre-Cretaceous unconformity, has significant topography. In addition to variable topography, local salt-dissolution tectonics affected both accommodation space and base-level changes in the oil sands reservoirs (Hein, et al., 2008). The subsurface in Alberta is predominantly quaternary tills and fluvial sediments overlying Cretaceous siliciclastics and an angular unconformity surface separating these clastic rocks from Devonian and Mississippian carbonates (Figure 2-6). The true dip of the carbonates beneath the Pre-Cretaceous unconformity is very low (~1°). The Nisku Formation, a stratigraphic equivalent to the Lower Winterburn (Figure 2-3), dips with a gradient of 6.5 m/km near Edmonton (Mei, et al., 2015). This Lower Winterburn equivalent is dipping at a mere 0.4 degrees.

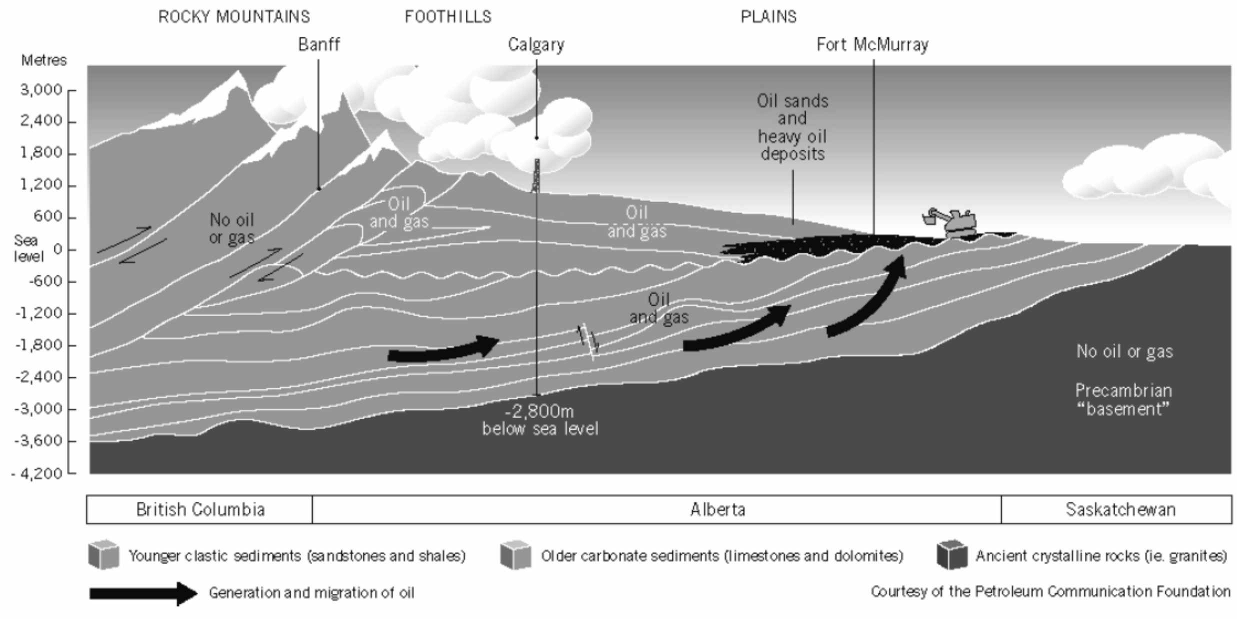

Figure 2-5. Southwest to Northeast cross section across the Western Canadian Sedimentary Basin (from Bott, 1999).

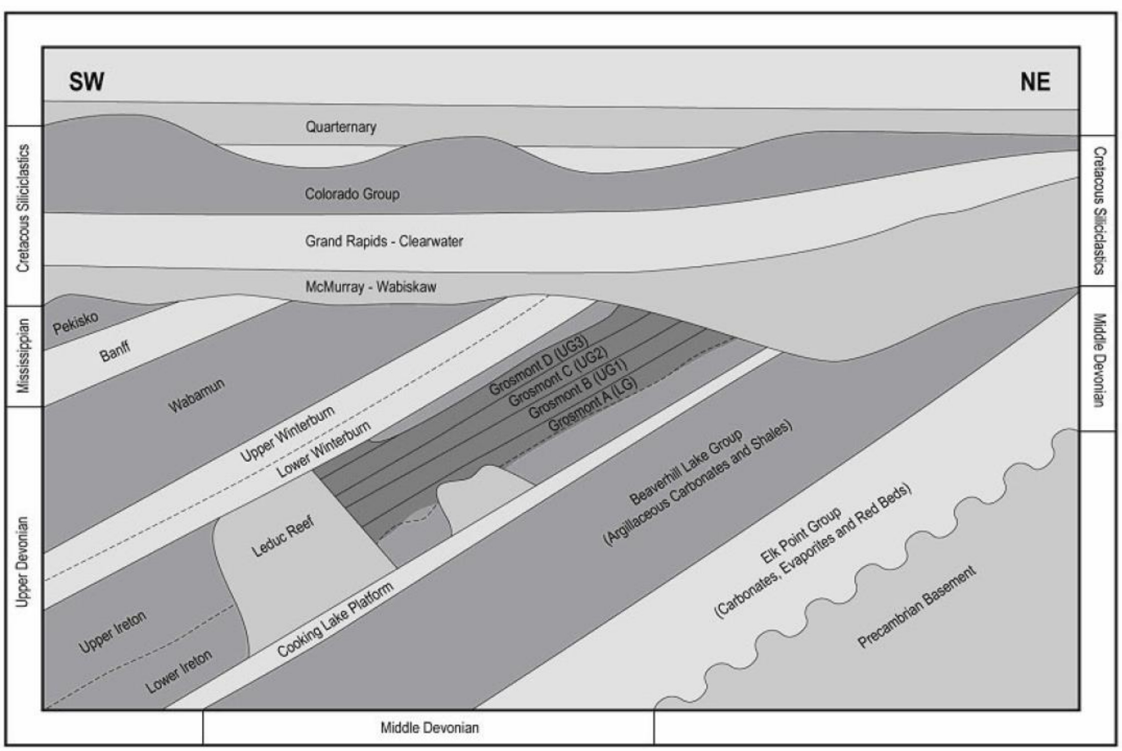

Figure 2-6. Southwest to Northeast cross section with stratigraphic nomenclature (from Hein et al., 2008).

The project area in this thesis lies in the southern portion of the Athabasca Oil Sands (Figure 2-1). The exact position of the study area is confidential. The entire rock column was included in the study, but with a focus mainly on the reservoir interval, the McMurray Formation, and the overlying “caprock,” strata (Clearwater, Grand Rapids, Colorado). The hydrocarbons present in the McMurray Formation in the Athabasca region exhibit significant biodegradation and thus have high densities and viscosities. Athabasca bitumen was found to have a density of 1.0133 g/cm^3 (8 °API) at 15.56 °C and a density of 0.90073 g/cm^3 (25 °API) at 195.00 °C (Souraki, 2012). At 20 °C, Athabasca bitumen has a viscosity greater than 500 000 cP, and at 130 °C Athabasca bitumen has a viscosity of 100 cP (Mehrotra and Svrcek, 1986). To compare, water at 25 °C has a viscosity of 0.894 cP, and peanut butter has a viscosity of 250 000 cP. The large contrast in density and viscosity values at variable temperatures is the property that SAGD in-situ bitumen extraction utilizes to produce the hydrocarbons.

2.3 Project area local geology

A well log cross section from the project area is shown in Figure 2-7, with the primary curves used for well log interpretation and seismic data analysis displayed. The four curves shown are: gamma ray, P-wave sonic, density and resistivity. Together these four well logs provide valuable information for geological interpretation and for seismic correlation. The gamma ray log was primarily used as a sand-shale differentiator. Relatively low gamma ray values (40-80 °API) indicate reservoir sands and relatively high gamma ray values (80+ °API) indicate mudstones. The sonic and density well logs were used for seismic correlation and to pick geological boundaries on well logs. The resistivity log is a reservoir fluid indicator, as saline formation water has low resistivity whereas hydrocarbons have high resistivity values.

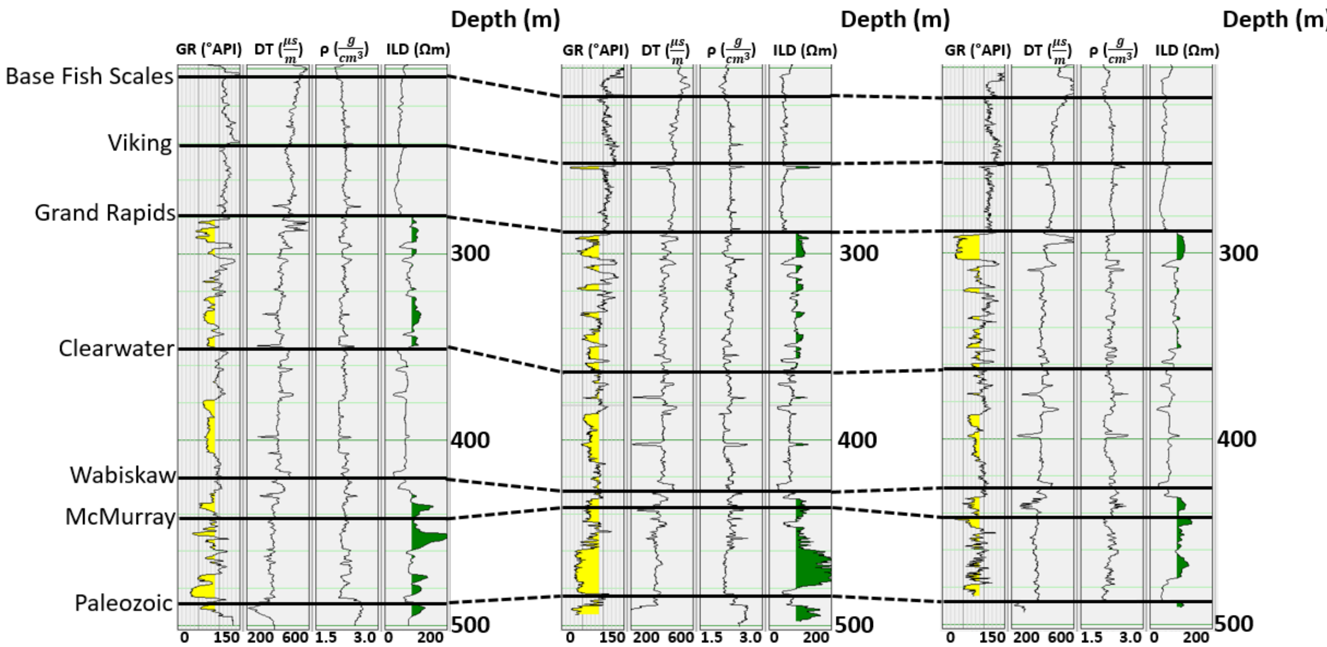

Figure 2-7. Cross section of three well logs in the project area.

CHAPTER 3: SEISMIC DATA PROCESSING

Data processing was undertaken in an integrated manner for the PP and PS seismic data, using Schlumberger Vista and Halliburton ProMAX software. The main interval of interest extends from the surface to the Paleozoic Unconformity (Devonian Beaverhill Lake Group). The Cretaceous-Devonian contact has a large P and S acoustic impedance contrast, generating a high amplitude reflection that appears on both the PP and PS seismic datasets. This bright reflection occurs at approximately 500 ms and 800 ms in the PP and PS volumes respectively. The data processing flows followed much of the methodology from previous CREWES reports (Kelly, 2012 and Isaac, 1996).

The seismic dataset was acquired in the Athabasca Oil sands region of Northeast Alberta in 2013. A total of 52 East-West oriented source lines and 34 North-South receiver lines both with 125 m separations made up the survey, with the geometry shown in Figure 3-1. Sources and receivers were separated by 25 meters, with 648 live channels per shot. Dynamite charges of ¼ kg buried at 6 m acted as energy sources. The sample rate was 1 ms and the record length was 4s.

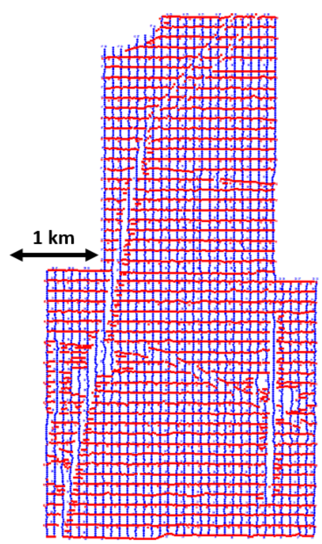

Figure 3-1. 3D seismic data sources (red) and receivers (blue).

The raw records were separated into vertical, in-line and cross-line components (Figures 3-2, 3-3 and 3-4). The in-line and cross-line components were rotated into radial and transverse components to increase the signal to noise ratio of reflected S-waves (Figure 3-5) (Alford, 1986). Example radial and transverse raw records are shown in Figure 3-6 and Figure 3-7. The vertical geophone component records mostly compressional waves, whereas the radial and transverse components generally record reflected S-waves. The most obvious features on all 3 raw records are ground roll and refracted arrivals. Hyperbolic reflection events are present and fairly obvious on the vertical component raw record (Figure 3-2). Reflection events are visible on the radial component shot gather (Figure 3-6), particularly at the largest offsets. No easily distinguishable reflection events are visible on the transverse component shot gather (Figure 3-7). The fact that converted wave reflections are limited to the radial shot gather may imply that the subsurface is essentially isotropic or has only vertical transverse isotropy, as there is no immediate evidence of shear wave birefringence.

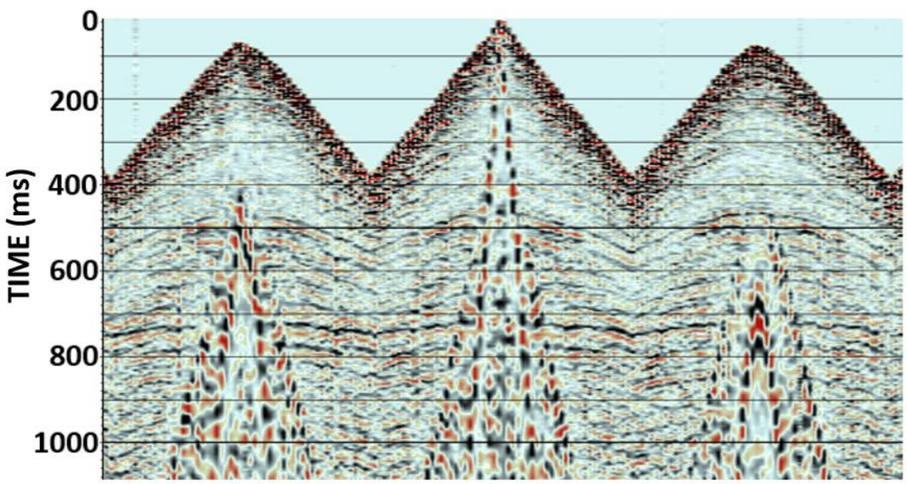

Figure 3-2 Sample vertical component raw seismic record.

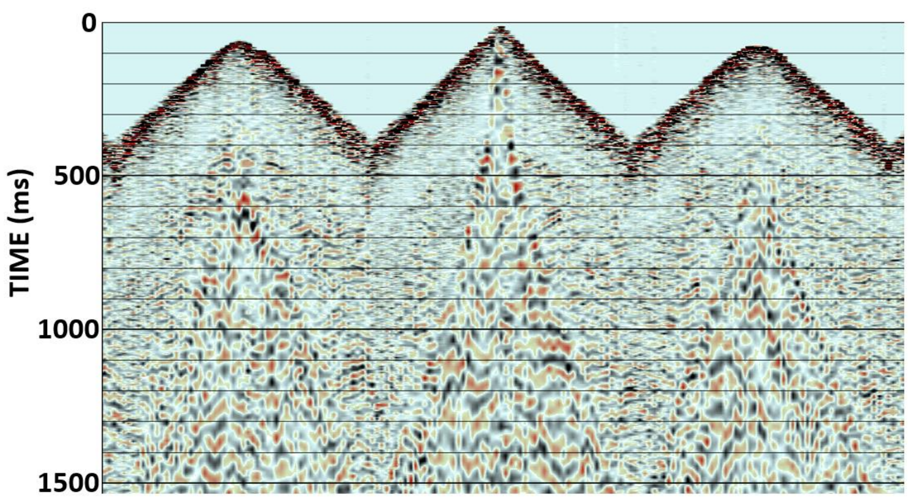

Figure 3-3. Sample inline component raw seismic record.

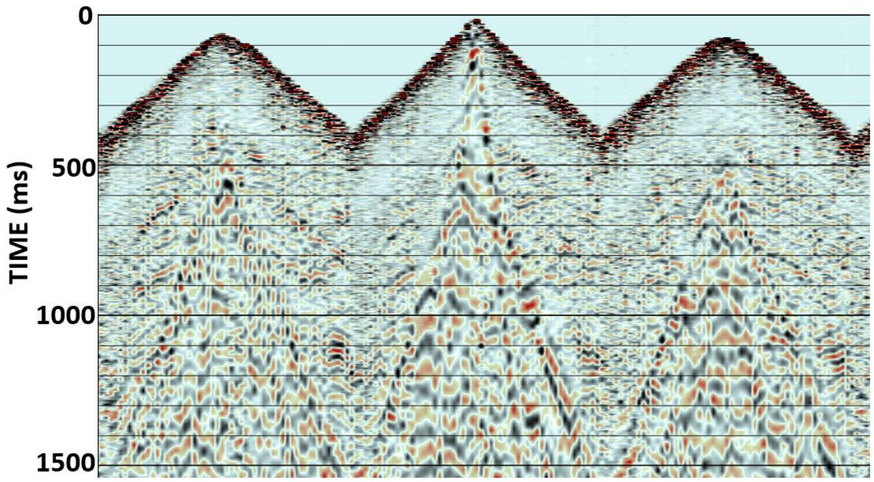

Figure 3-4. Sample crossline component raw seismic record.

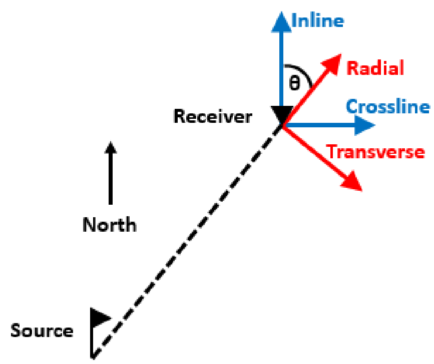

Figure 3-5. Schematic showing the field geophone orientations (blue) and the rotated geophone orientations (red).

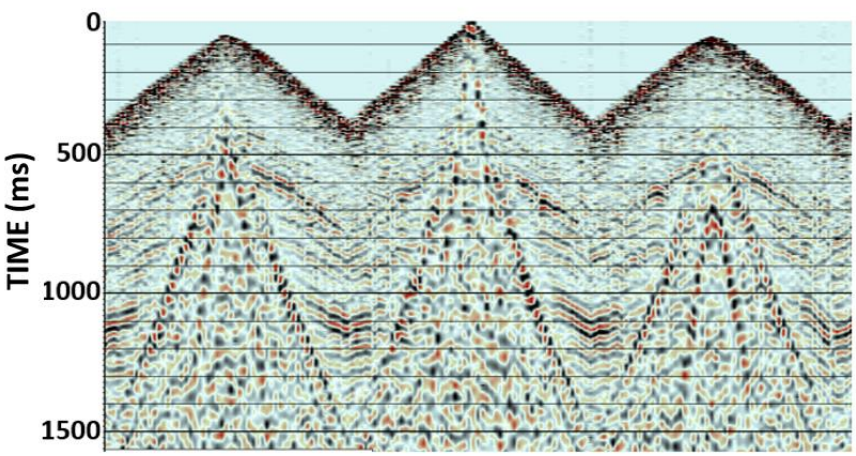

Figure 3-6. Sample radial component raw seismic record.

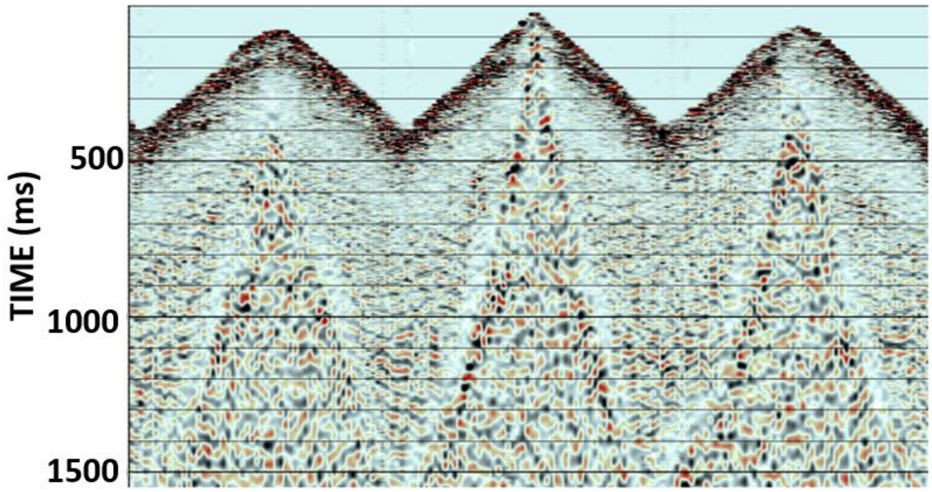

Figure 3-7. Sample transverse component raw seismic record.

3.1 PP seismic data processing

The general PP processing flow for 3D PP seismic data follows that of Isaac (1996) and is outlined in Figure 3-8. The 4 second seismic record was limited to 1.5 seconds to save on processing computation time as the interval of interest is well above 1.5 seconds and this was adequate for migration. Geometry was assigned and the bin grid was defined. The orthogonal survey design and 25 meter source and receiver spacing allows for a simple evenly spaced bin grid of 12.5 m x 12.5 m. After assigning geometry and the binning system, fold was calculated (Figure 3-9 and 3-10). The maximum nominal fold is 46 and the average fold is 28; the nominal fold statistics are displayed in Figure 3-11. PP seismic fold for offsets up to 500m is shown in Figure 3-10. The lower fold seen in these smaller offsets results in lower signal to noise ratio in shallower zones. The maximum offset recorded was 900m.

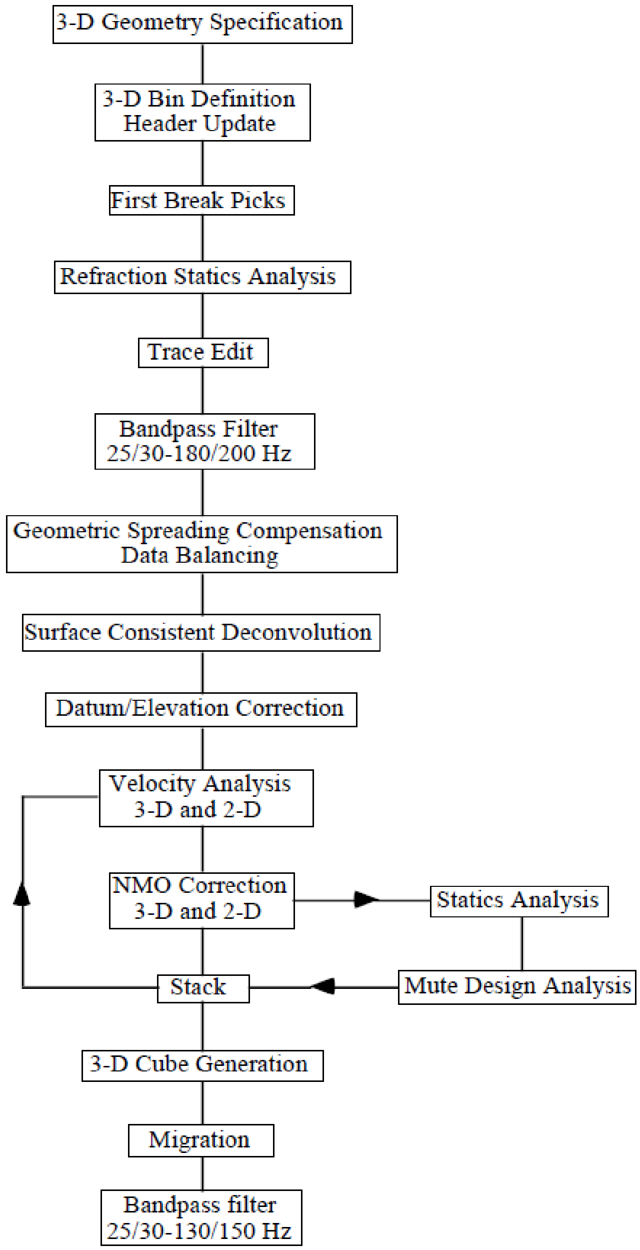

Figure 3-8 3D PP processing flow (modified from Isaac, 1996).

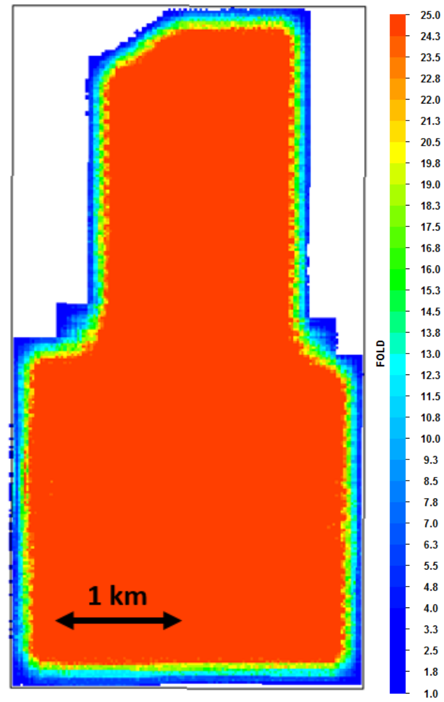

Figure 3-9. PP seismic nominal fold.

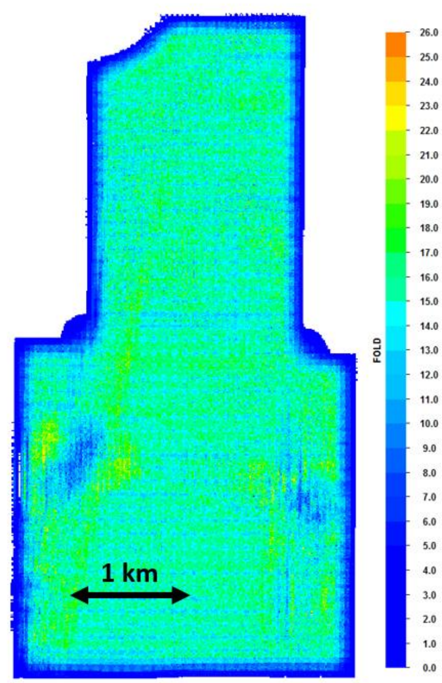

Figure 3-10. PP seismic fold limited to 500 m offset.

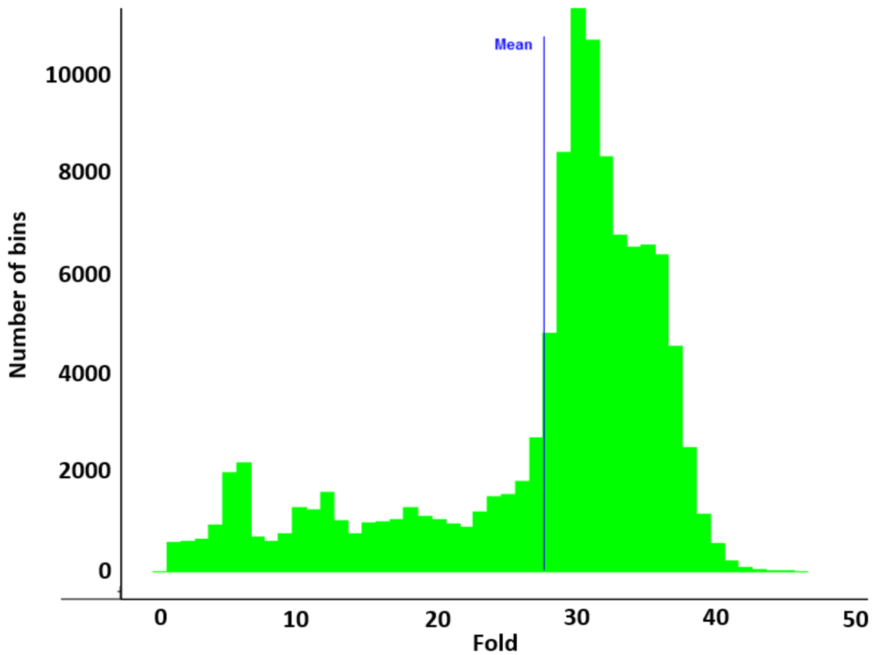

Figure 3-11. PP seismic survey fold histogram for all azimuths and offsets. The average fold in the survey is 28.

3.1.1 PP Elevation and refraction statics

Next, elevation and refraction statics corrections were calculated and applied. Topographic variations were reduced to a datum of 750 m and a replacement velocity of 1900 m/s was used. The topography of the survey area is relatively flat, with the surface elevation ranging from 660 m to 690 m (Figure 3-12). The selected datum of 750 m was higher elevation than all of the surface elevations. First break picks were made for the raw shot gathers, and refraction statics were calculated using the first break times (Cox, 1999). A scatterplot of first break time versus offset shows that arrival times concentrate on two linear trends, which implies two near surface low velocity layers in the model (Figure 3-13). The velocities of the two low velocity layers are ~1700 m/s and ~2000 m/s. The magnitude of the elevation statics ranged from 30 ms to 70 ms and the magnitude of the refraction statics ranged from 15 ms to 30 ms.

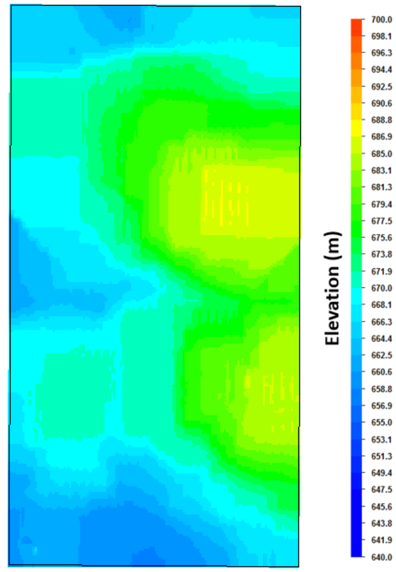

Figure 3-12. Survey surface elevation.

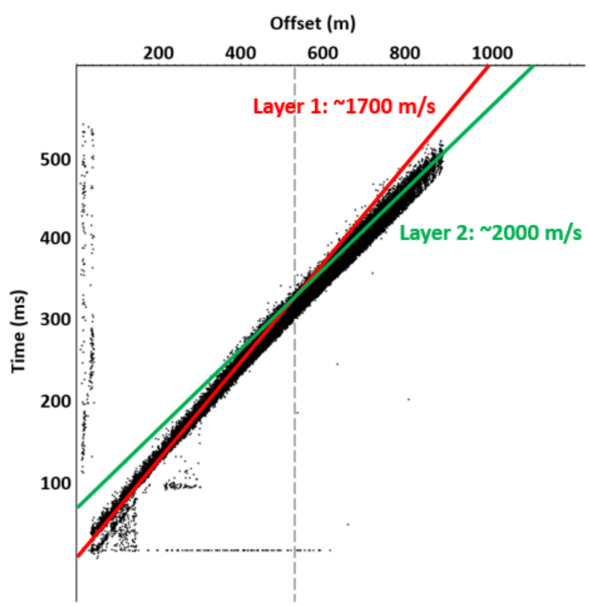

Figure 3-13. A scatterplot of first break time versus offset values.

3.1.2 Radial transform denoise

Following elevation and refraction statics, a radial transform denoise algorithm was used to attenuate the high amplitude ground roll (Henley, 2011). The radial filter is an effective tool to remove unwanted coherent linear noise in seismic shot gathers. First, the radial transform of the statics-corrected shot gather is taken (Figure 3-14). A low cut filter is then applied to the data in the R-T domain, followed by an inverse radial transform. The output of this reverse radial transform is a collection of the linear events within the shot gather. The linear noise can now be simply subtracted. A gather before and after the radial transform is displayed in Figure 3-15. Amplitude corrections were then undertaken to correct for the effects of geometric spreading through an exponential gain function. A mean scaling algorithm was used to balance traces across the gather.

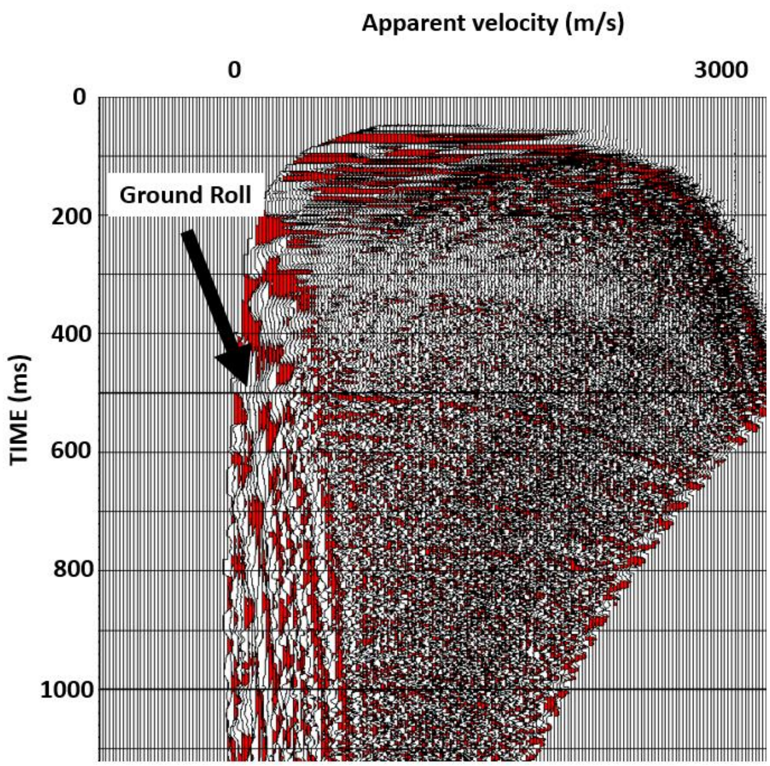

Figure 3-14. Radial transform of a shot gather.

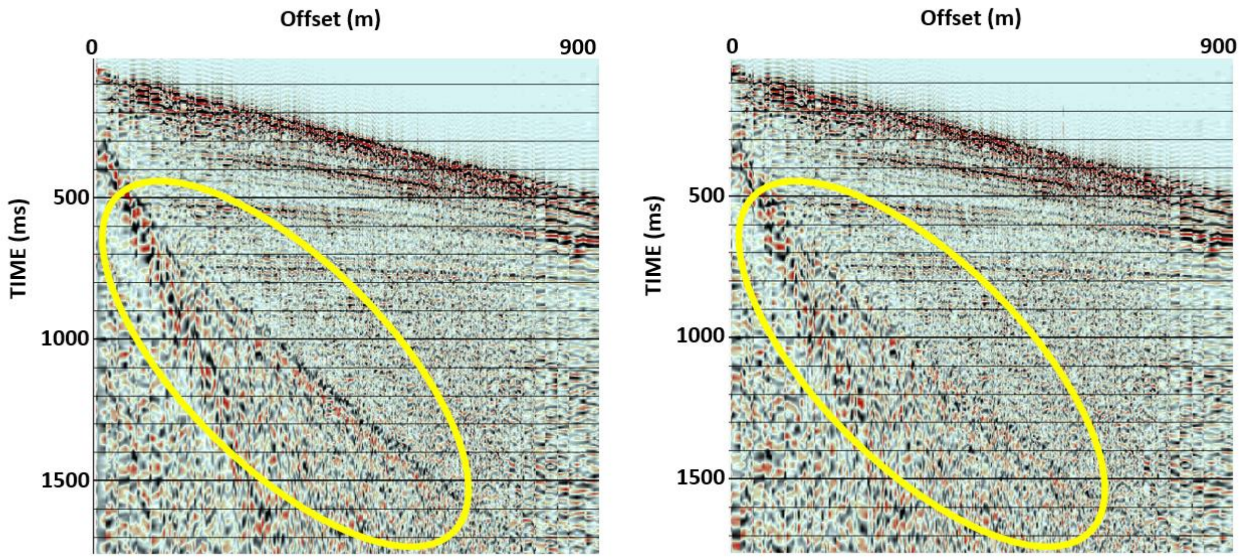

Figure 3-15. Shot gather before (left) and after (right) radial transform denoise. The attenuated coherent noise is highlighted with yellow ovals.

3.1.3 Gabor deconvolution and spectral balancing

Gabor deconvolution, a non-stationary deconvolution technique, was used to enhance frequency and attenuate noise. Several deconvolution algorithms were tested but Gabor deconvolution was found to produce the optimum results. The Gabor transform, a non-stationary generalization of the Fourier transform was applied to each seismic trace and a time-frequency decomposition was performed (Margrave et al., 2004). The before and after results for Gabor deconvolution show effective frequency enhancement and noise attenuation (Figure 3-16). The residual surface wave energy at near offsets were well attenuated after the application of Gabor deconvolution. In addition to Gabor deconvolution, spectral whitening was used to enhance the frequency spectrum.

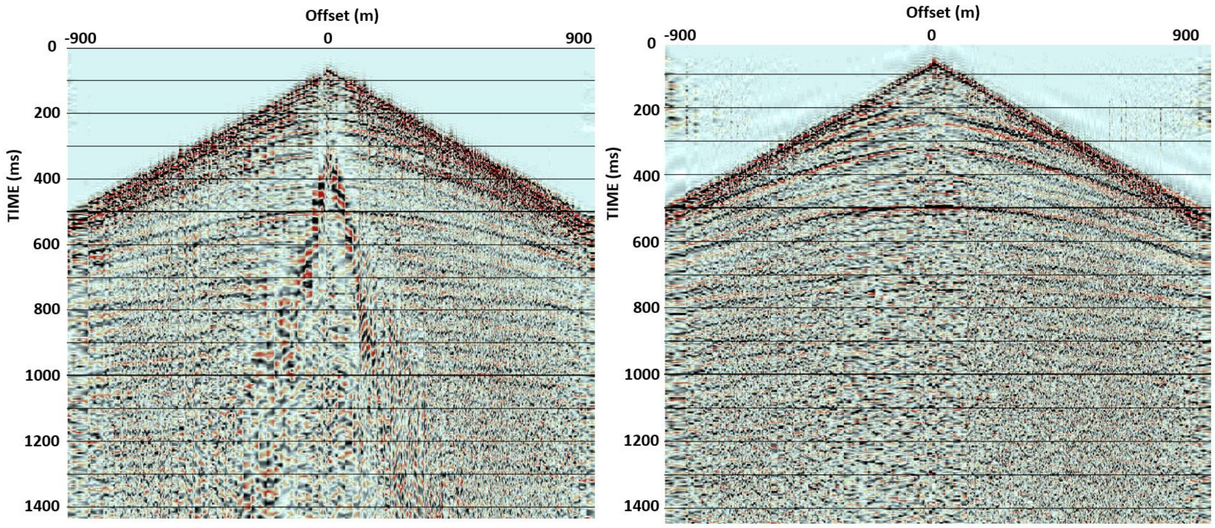

Figure 3-16. Shot gather before (left) and after (right) Gabor deconvolution.

Time-variant spectral balancing is a trace-by-trace process in which a seismic trace is broken down into a series of traces in a frequency band; automatic gain control is applied to each of the component traces and then the traces are summed. This process equalizes amplitudes at all times, effectively whitening the amplitude spectrum. Unfortunately, spectral balancing is indifferent to noise and can boost unwanted high frequency noise (Figure 3-17).

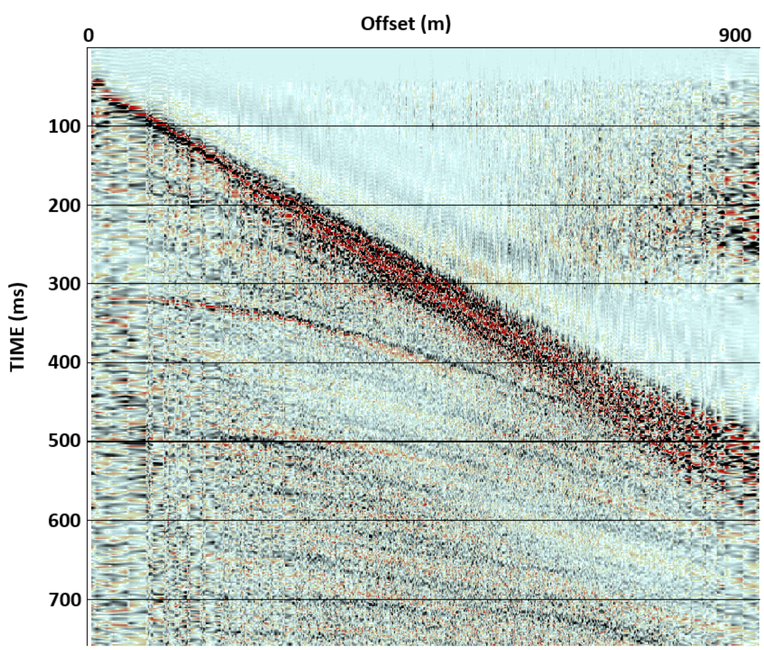

Figure 3-17. Shot gather after application of spectral balancing, displaying high frequency noise.

3.1.4 Velocity analysis and normal moveout correction

Velocity analysis was performed to obtain root mean square (RMS) velocities. RMS velocities are used to correct for normal moveout (NMO) of seismic reflections. Normal moveout is the effect of increased traveltimes of seismic reflections with offset. Correcting for NMO will move offset reflections to their zero-offset time. RMS velocities were determined by picking velocity profiles at common midpoint bin locations based on semblance, common offset stacks and constant velocity stacks (Figure 3-18). Semblance (equation 3-1) is calculated for a discrete set of velocities to determine how coherent a hyperbola is in a group of traces. Bright zones on a semblance plot indicate best coherence for a certain RMS velocity (Taner and Koehler, 1969).

To create common offset stacks, traces were sorted into offset groups and then stacked. Common offset stacks show seismic reflection hyperbolas well. Constant velocity stacks were obtained by correcting for NMO and CMP stacking for a discrete velocity. Reflections will stack additively when the correct RMS velocity is used in constant velocity stacking. Constant velocity stacks in conjunction with semblance plots and common offset stacks provide a robust way to obtain RMS velocities in the subsurface. NMO correction introduces a frequency distortion at large offsets and for shallow reflections (Yilmaz, 2001). A mute was applied to the NMO-corrected source gathers to account for this distortion. The NMO mute had offset and time values of: 123 m/135 ms, 253 m/265 ms, 356 m/376 ms, 510 m/510 ms and 734 m/861 ms.

$$Semblance = \frac{\sum_{j=k-\frac{N}{2}}^{k+\frac{N}{2}} \left(\sum_{i=1}^{M} f_{i,j(i)}\right)^2}{\sum_{j=k-\frac{N}{2}}^{k+\frac{N}{2}} \sum_{i=1}^{M} f_{i,j(i)}^2} \tag{3.1}$$

Following velocity analysis and NMO correction, residual statics were calculated and applied. Residual statics are calculated using stack-power maximization (Ronen and Claerbout, 1985). Stack-power maximization is a surface consistent residual statics process. Several iterations of velocity analysis and residual statics estimation were done in order to obtain the best quality stacked section. The prestack shot gathers after iterated velocity analysis and residual statics show clear, flattened reflection horizons (Figure 3-19).

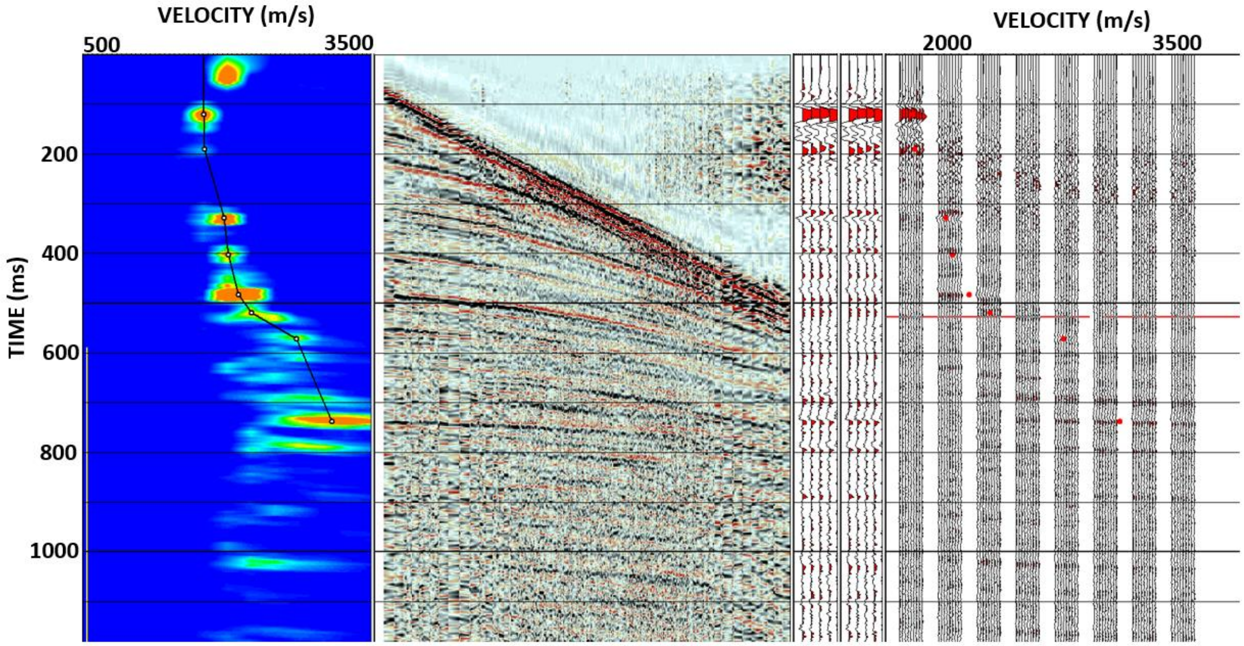

Figure 3-18. Interactive velocity analysis display: semblance (left panel), common offset stack (center panel) and constant velocity stacks (right panel).

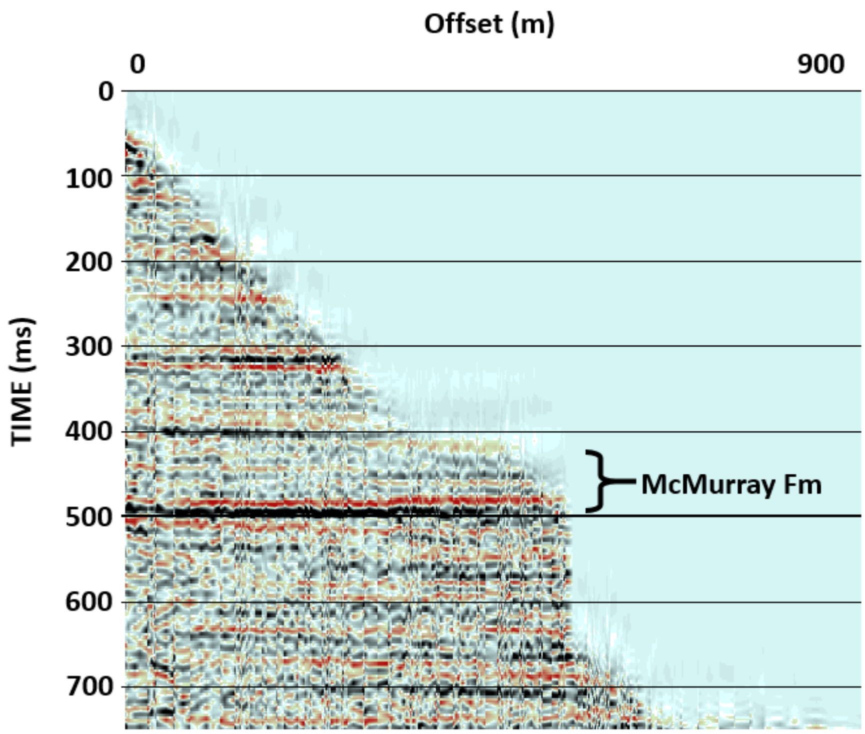

Figure 3-19. Prestack shot gather example following 3 iterations of velocity analysis/NMO correction and residual statics. NMO mute applied.

3.1.5 PP CMP stacking

Common midpoint stacking was undertaken for the next step. Stacking is an effective tool in increasing signal to noise ratio. Traces with various azimuths and offsets that share a common midpoint are summed to form a single trace. After preprocessing, the number of traces summed is called the fold. The stacked section shows clear and continuous reflections (Figure 3-20). The interval of interest, extending from 250 ms to 550 ms, is well imaged.

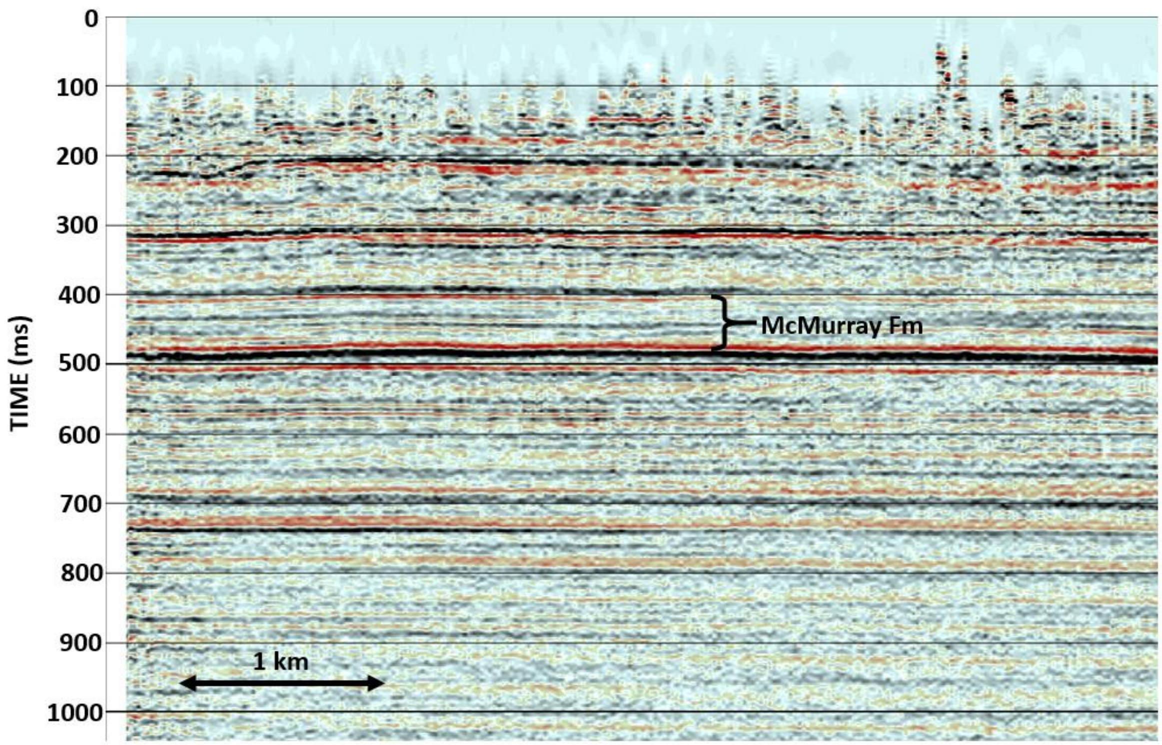

Figure 3-20. Example of PP stacked section from the data volume after iterated velocity analysis and application of residual statics.

To enhance the signal to noise ratio even further, random noise was attenuated with F-XY deconvolution. F-XY deconvolution is an effective spatial prediction filtering method in which noise is attenuated by comparing adjacent traces in the frequency domain (Chase, 1992). The application of F-XY noise attenuation improves signal to noise ratio (Figure 3-21).

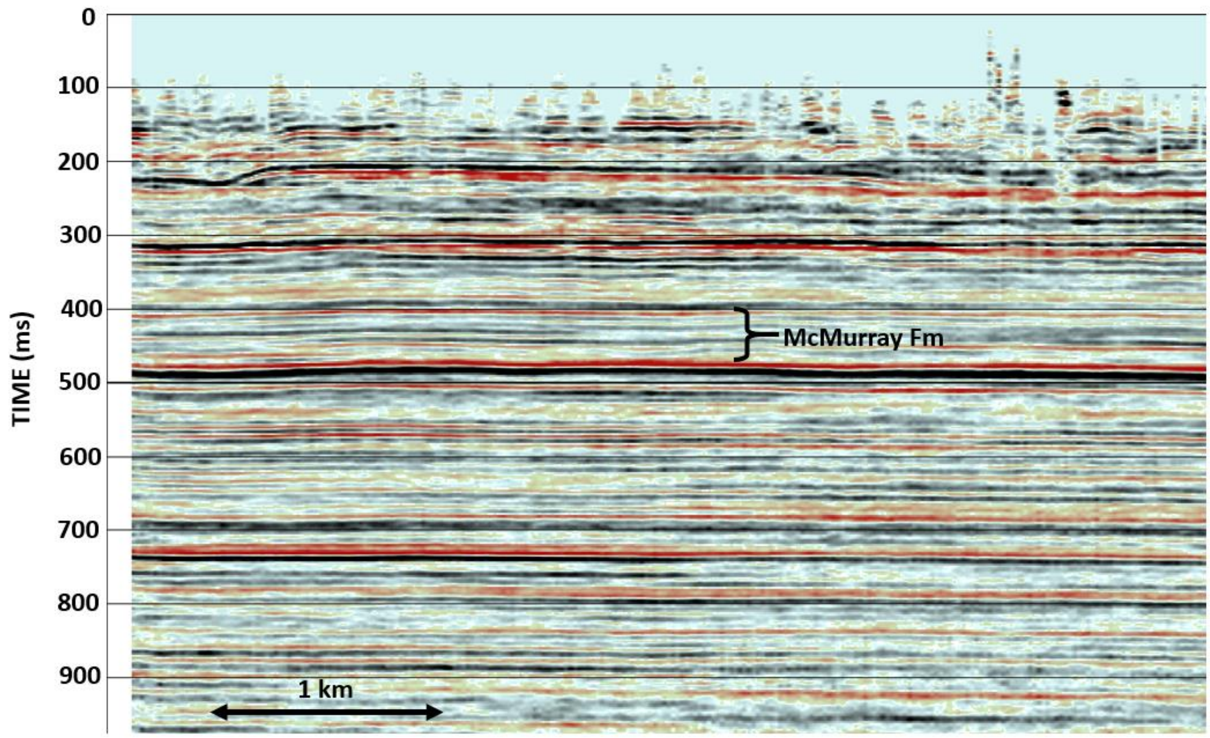

Figure 3-21. Example of a PP stacked section after F-XY deconvolution.

To complete the PP processing, post-stack migration was performed using a phase shift plus interpolation (PSPI) migration algorithm. PSPI migration is a generalization of phase shift migration that can account for lateral variation of seismic velocities (Gazdag and Sguazzero, 1984). In PSPI migration, sources and receivers are downward continued by phase-shifting, utilizing several laterally homogeneous velocity fields. For each velocity field a reference wave field is produced. The reference wave fields are interpolated to recover the true wave field (Gazdag, 1978 and Gazdag and Sguazzero, 1984). An example of a section from the migrated data volume is shown in Figure 3-22. Migration does not have a significant effect on the seismic volume due to the nearly flat layer geological strata in the Athabasca region.

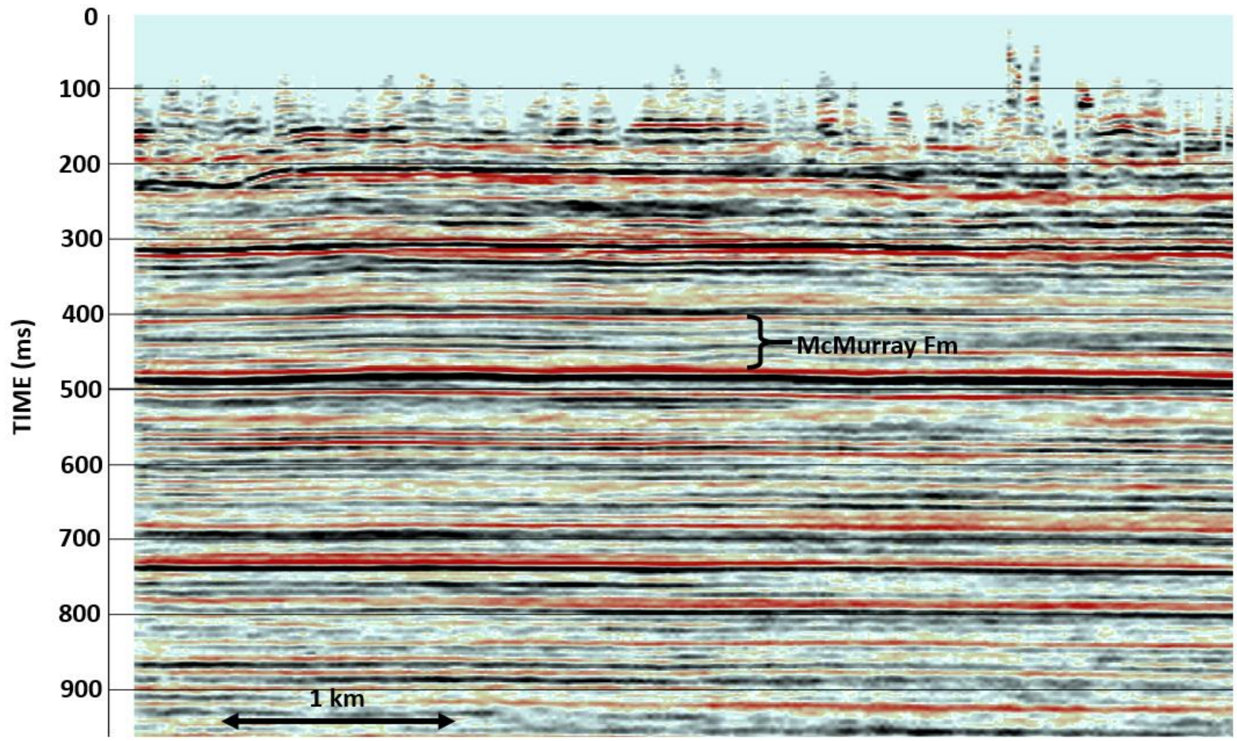

Figure 3-22. PP migrated seismic section.

3.2 PS seismic data processing

There are a number of notable differences in the processing of converted wave seismic data compared to processing conventional vertical component records. Some of the key differences in PS data processing include: trace rotation, application and calculation of shot and receiver statics, converted wave velocity analysis and common conversion point binning. Additionally, some of the key outputs from PP seismic data processing are necessary to adequately process converted wave data. P wave shot statics from PP refraction analysis are applied early in the PS processing flow and PP RMS velocities are required for correct asymptotic common conversion point and common conversion point binning and stacking. Many of the same processing tools utilized in PP processing were used to image the converted wave reflections; so only the methodologies differing from those used in PP processing are discussed in detail. Before and after shot gather examples from the PS pre-processing are shown in figures 3-23 and 3-24.

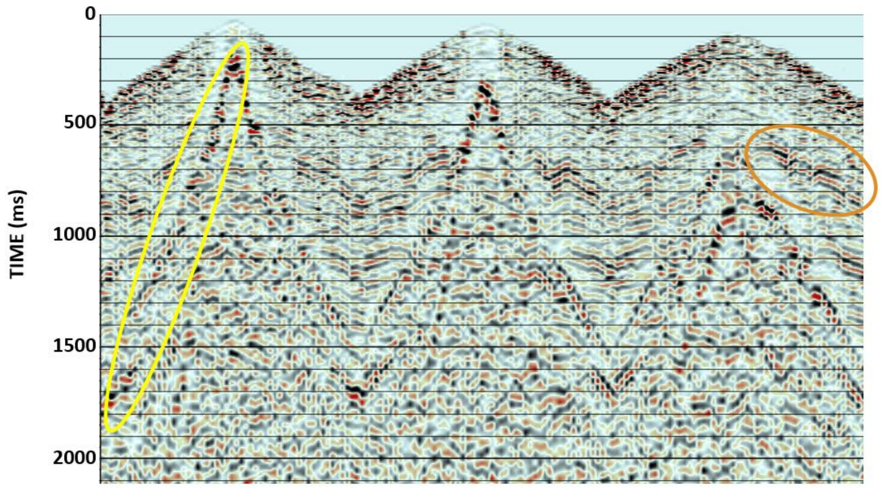

Figure 3-23 Raw PS shot gather example. Yellow circle highlights ground roll and orange circle highlights PS reflections.

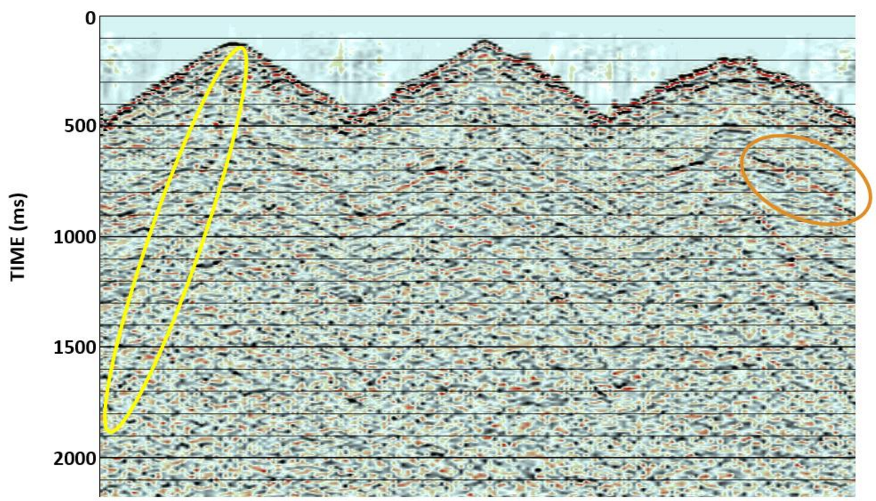

Figure 3-24 PS shot gather example with source statics, radial denoise and Gabor deconvolution. The ground roll present in figure 3-20 has been attenuated (yellow circle). The frequency of the PS reflections has been increased by deconvolution (orange circle). There are unresolved receiver statics which cause the reflections to have low coherency.

The bin grid used for the converted wave seismic data was the same as the PP bin grid. After assigning geometry, inline and crossline components recorded in the field were rotated to radial and transverse components. Converted wave reflections were limited to the radial component gathers and thus the subsurface media was considered to be horizontally isotropic (Figures 3-6 and 3-7). P wave shot statics and P and S wave elevation statics were applied next. P wave shot statics were obtained from the PP processing flow and elevation statics were calculated from field elevations and a fixed datum for a downgoing P wave and an upgoing S wave. The next processes: radial transform denoise, Gabor deconvolution and spectral balancing were applied in a similar manner as described for the vertical component processing.

3.2.1 PS velocity analysis

The converted-wave velocity analysis was done in a similar way to PP velocity analysis (Figure 3-25). The output of the converted wave velocity analysis are converted wave stacking velocities which can be used to correct normal moveout of the PS reflections.

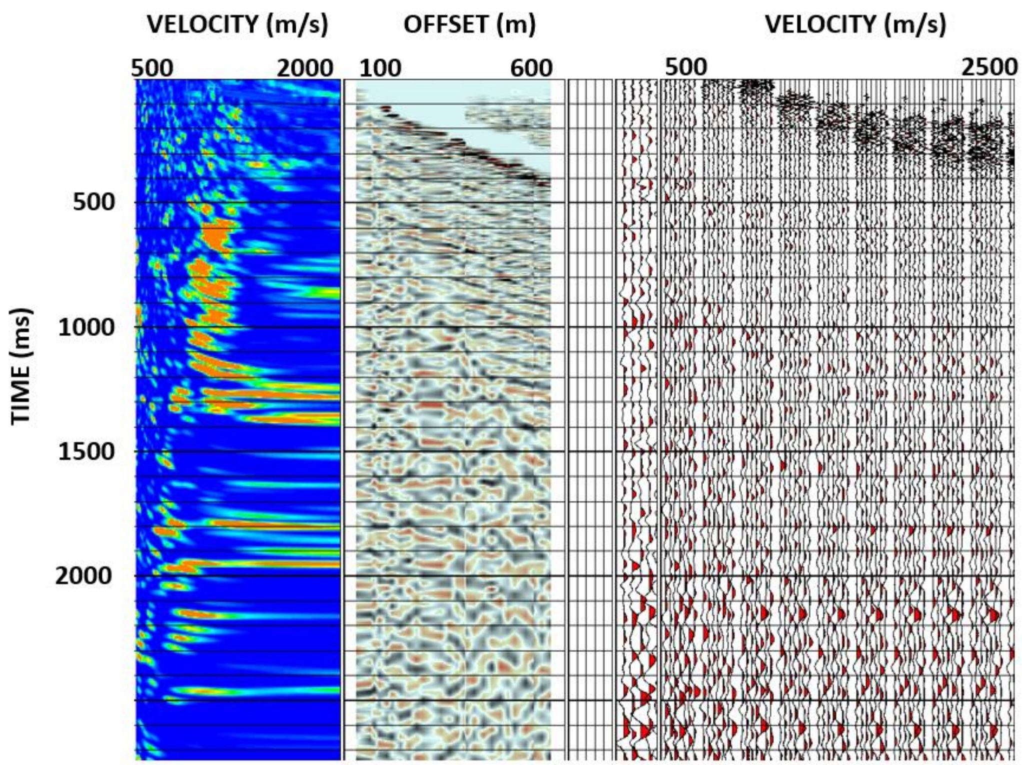

Figure 3-25. Interactive velocity analysis for converted wave RMS velocities, semblance (left panel), common offset stack (center panel) and constant velocity stacks (right panel).

3.2.2 S-wave receiver statics

Common receiver stacks were generated next, and these were used to determine S-wave receiver statics. The near surface often has low, complex and variable shear wave velocities, resulting in large S-wave receiver statics (Ion and Galbraith, 2011). Receiver static estimation based on common receiver stacks have three main steps: horizon picking, horizon smoothing and horizon subtraction. First, continuous horizons were picked on common receiver stacks (Figure 3-26). Smoothing was applied to the horizons to obtain a regional trend. The horizon-based static was then acquired by subtracting the original horizon pick from the smoothed regional trend. It is very important to pick several horizons and to calculate statics for each to avoid biasing the static results by using only a single reflection structure. After the receiver static was calculated it was applied to prestack data and also to receiver stacks (Figure 3-27).

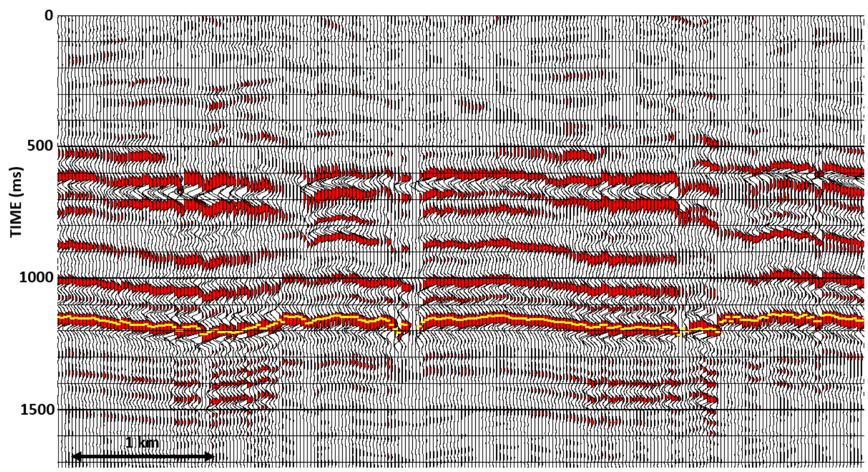

Figure 3-26. Radial component common receiver stack. Horizon used for statics analysis in yellow.

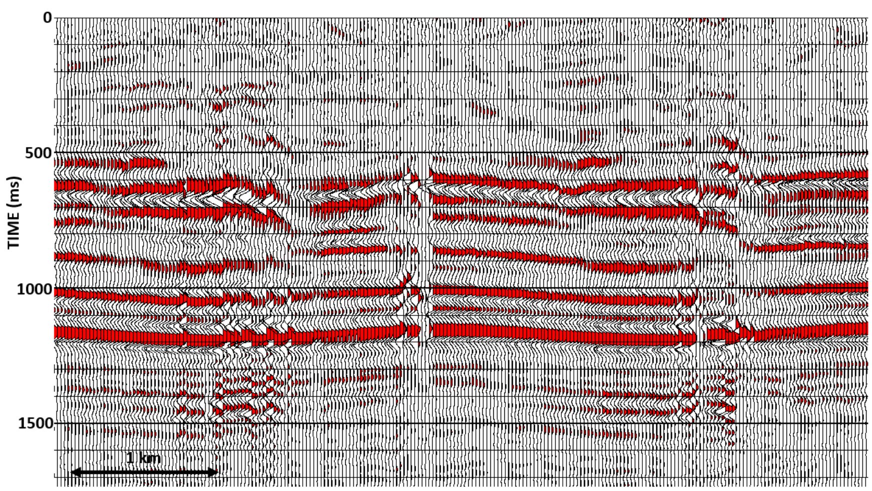

Figure 3-27. Radial component common receiver stack after application of S-wave receiver statics.

3.2.3 PS CCP stacking

Due to the asymmetric raypath of a converted wave reflection PS data cannot be stacked using traditional CMP stacking, as the conversion point varies with depth. The conversion point moves away from the receiver with increasing depth and trends towards an asymptotic value (Figure 3-28). Snell's law tells us that the S-wave reflection angle is related to the V_p/V_s and P-wave incidence angle. As depth increases, the P-wave incidence angle decreases and the position of the PS-wave conversion point approaches an asymptote. An asymptotic common conversion point stack can be made for an average V_p/V_s in an interval of interest (Figure 3-29). Asymptotic common conversion point stacks are effective in focusing deeper converted wave reflections, but they smear events in the near surface due to the error between the conversion point asymptote and the true conversion point. Using PP and PS stacking velocities, a spatially varying V_p/V_s can be created, which can be used to calculate the true conversion points of reflections. Alternatively, corresponding PP and PS horizons can be used to calculate V_p/V_s profiles at bin locations. Both methods were be used to create common conversion point stacks (Figure 3-30). Comparing the asymptotic common conversion point stack (Figure 3-29) to the common conversion point stack (Figure 3-30), the differences are minor and he major reflection events are common to both sections. The near surface, between 200 ms and 400 ms, is more coherent on the common conversion point stack, but the recovered offsets here are barely wide enough to support converted waves.

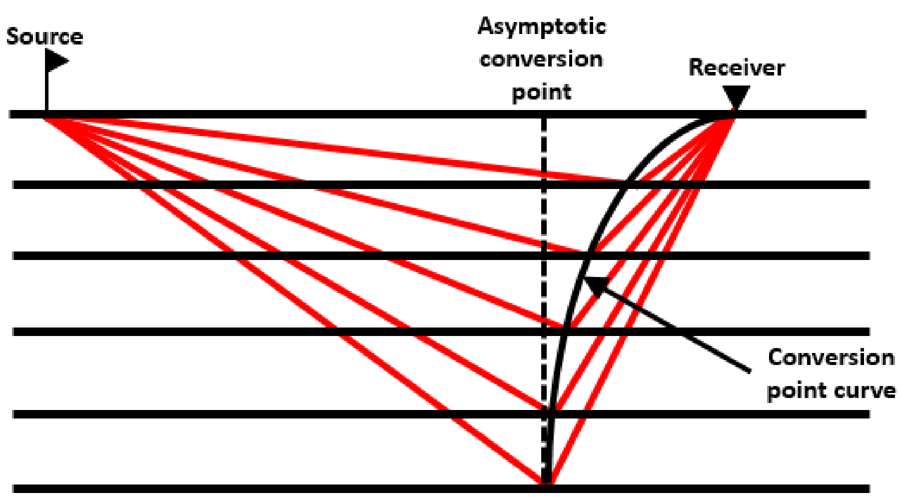

Figure 3-28. Reflection raypath geometries for converted waves. The conversion point and conversion point asymptote are shown.

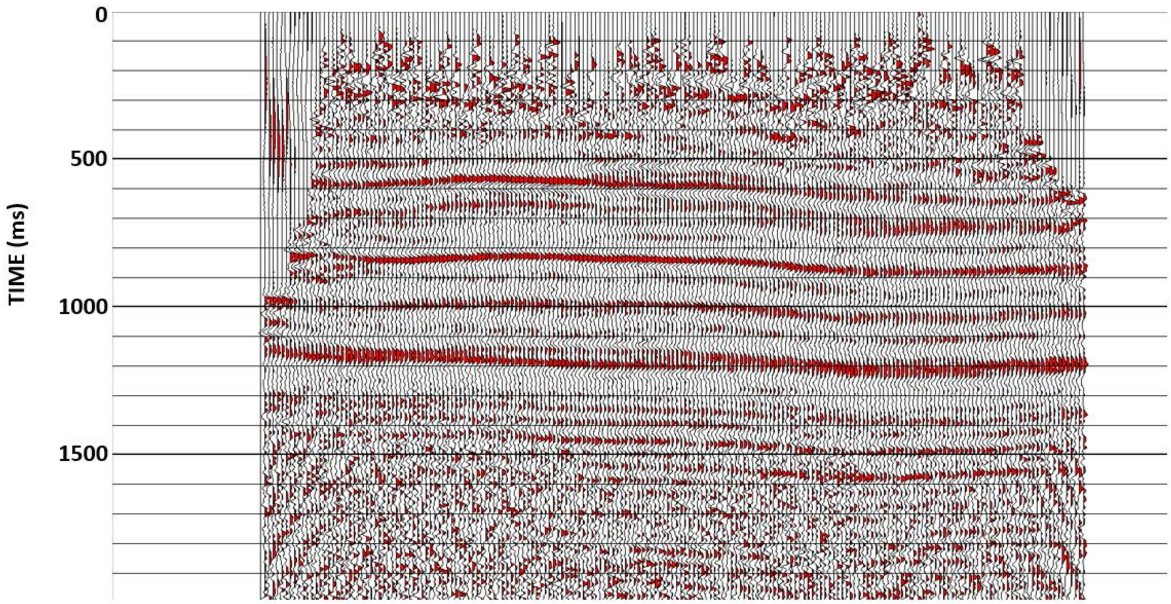

Figure 3-29. Radial component asymptotic common conversion point stack.

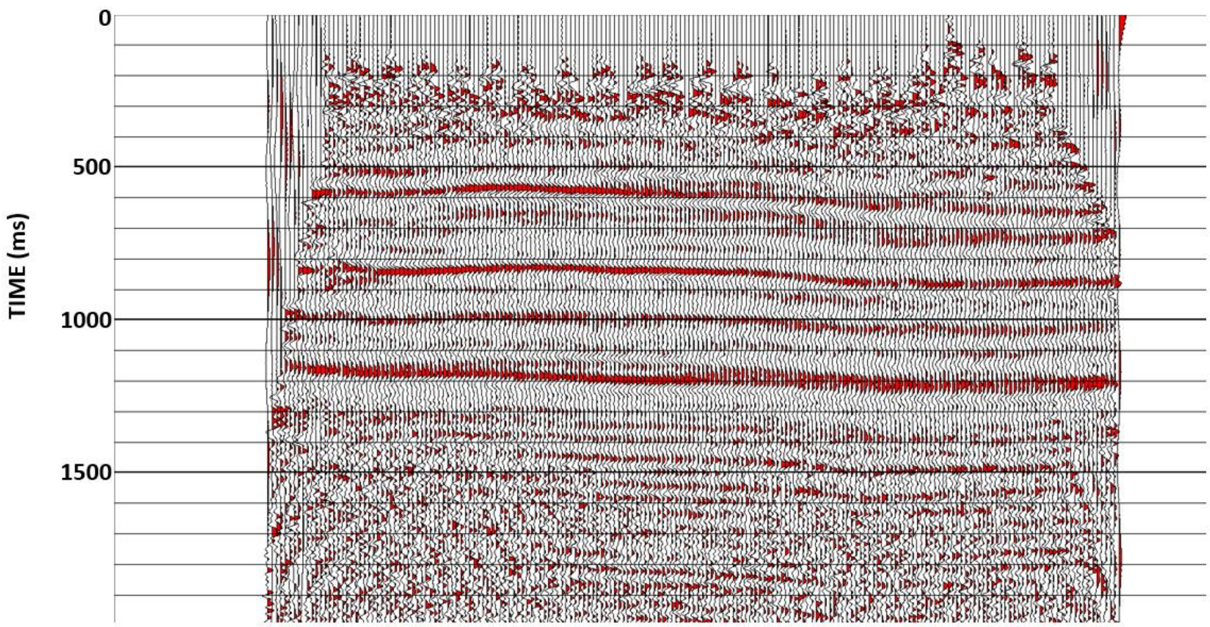

Figure 3-30. Radial component common conversion point stack.

3.3 Discussion

A conventional flow was used to process the seismic data. The vertical and radial geophone components were processed to create PP and PS volumes. The PP pre-stack data were processed into pre-stack gathers to be used for AVO inversion. With the exception of the shear wave receiver statics calculation and application and the binning and stacking process, the PP and PS processing flows were similar. The primary processing tools used were: refraction and elevation statics, deconvolution, velocity analysis and NMO correction, residual statics, stack and migration.

Figure 3-31 shows fully processed PP and PS volumes. The seismic data show pervasive reflections throughout, with the exception of below ~1400 ms on the PS data. Fortunately, the base of the zone of interest is at around ~900 ms in PS time.

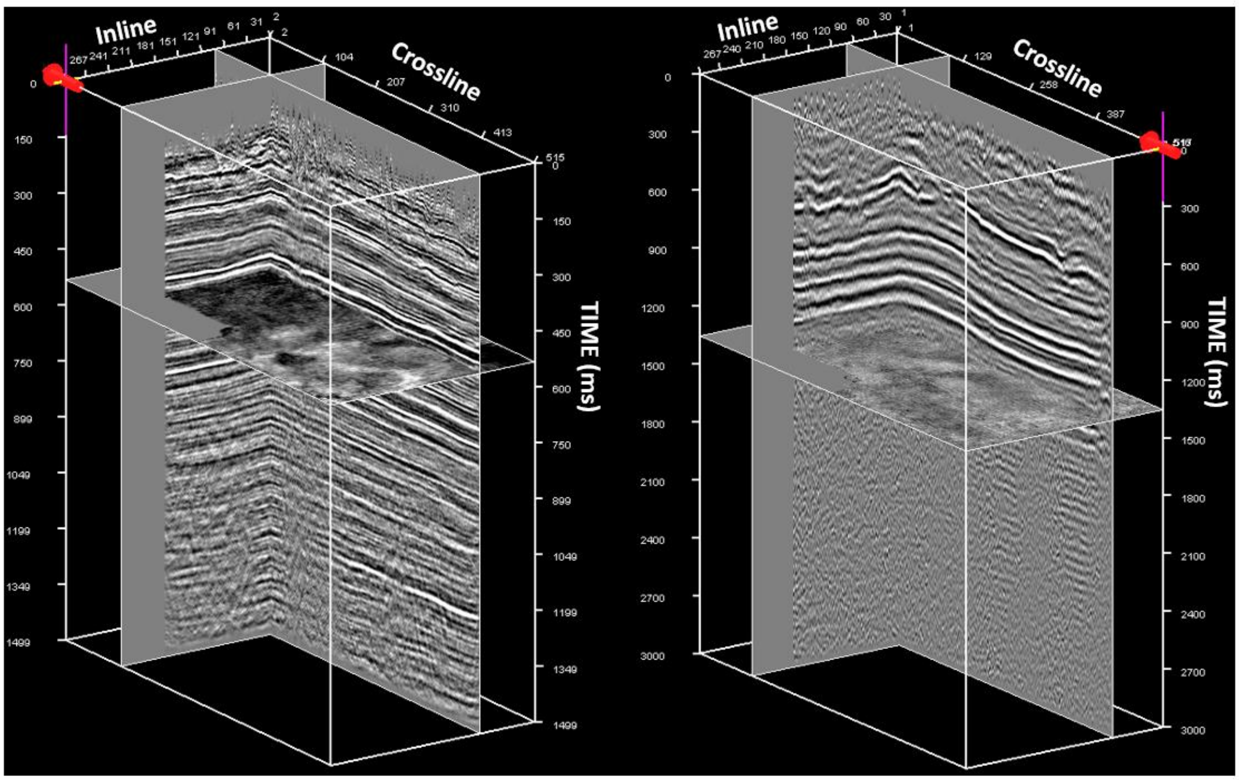

Figure 5-31. Example stacked PP (left) and PS (right) seismic datasets.

CHAPTER 4: SEISMIC DATA INTERPRETATION

In the Athabasca Oil Sands, seismic interpretation usually starts with well log correlation. The high well density in the project area, and relatively simple geological structure allowed synthetic seismogram correlations to be robust for seismic interpretation. Early in the interpretation workflow pervasive reflectivity contrasts were defined as specific geological boundaries. Pervasive reflection events are usually called seismic horizons. Instantaneous amplitude, which is related to reflectivity, is the first tool utilized in seismic stratigraphy. Other seismic parameters can aid in horizon picking in areas where instantaneous amplitude is unreliable. A permutation of seismic amplitude, phase or frequency is called a seismic attribute. Several seismic attributes are useful in horizon picking such as instantaneous phase and instantaneous frequency. Hardage et al. (1998), found that instantaneous frequency can be used as an edge detection method. Instantaneous frequency can also indicate the presence of hydrocarbons (Taner et al. 1979). Instantaneous phase can aid in defining horizons in low amplitude zones (Bondár, 1992).

More detailed geological interpretations were made once the regional seismic stratigraphy was defined. Basic interpretation techniques include: structure and amplitude map analysis, isochron analysis, time slice and stratal slicing. All of these initial interpretation practises were useful in this project. The PP seismic data wer interpreted first, followed by the PS seismic data. There are several reasons to work with the PP seismic data first: PP synthetic seismograms are simple to make, PP seismic data usually have higher bandwidth and PP seismic data usually have increased signal to noise. The regional interpretation of the PP and PS seismic volumes are explored in this section.

4.1 PP seismic data interpretation

Two 3D seismic volumes were used in the PP interpretation. One was processed as part of in this study, with emphasis on joint processing with the converted wave seismic dataset. The second, a recent commercially processed volume focussed on PP reflection imaging only. The two volumes are similar, as shown by a comparison of two in-line sections in Figure 4-1. The recent commercial processing spectrum shows that it contains frequencies up to ~150 Hz, whereas the jointly processed spectrum shows lower high frequency content (Figure 4-2).

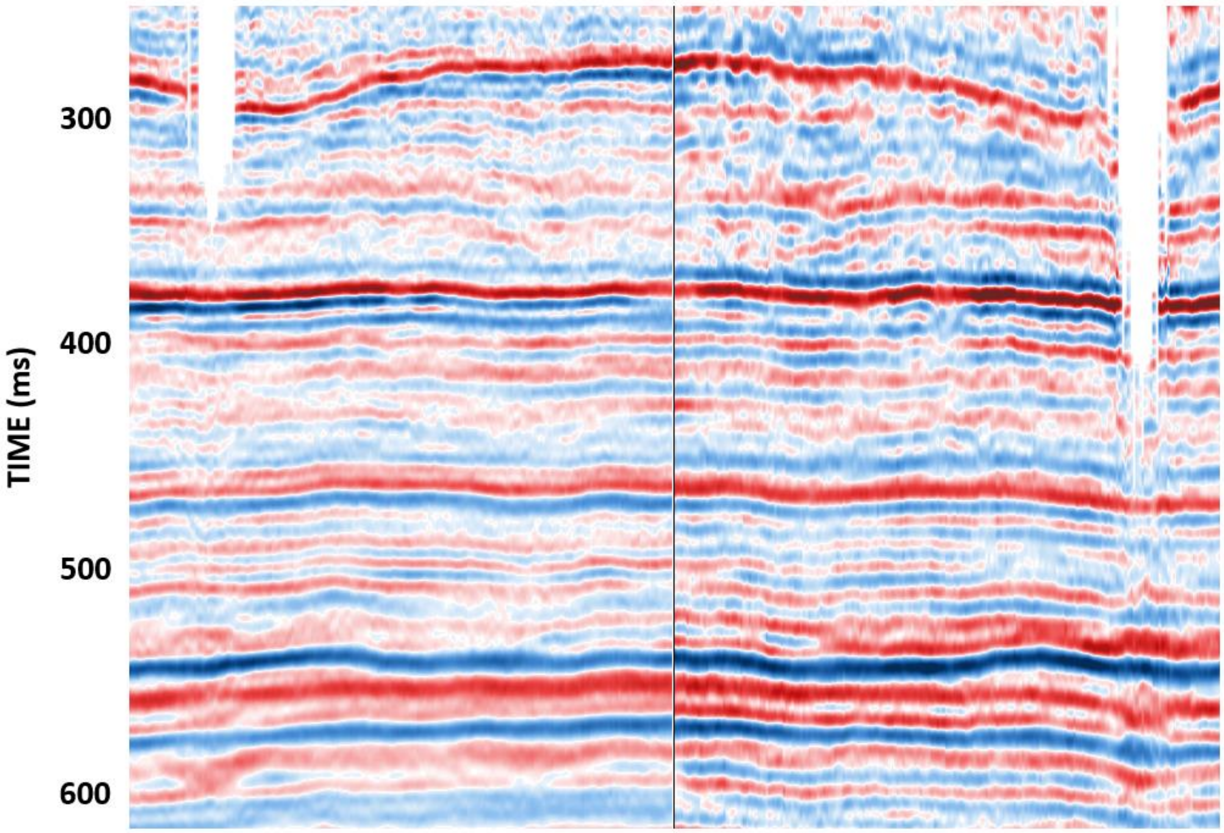

Figure 4-1. Mirror image seismic sections from commercial PP processing (left) and processing undertaken as a part of this study (right).

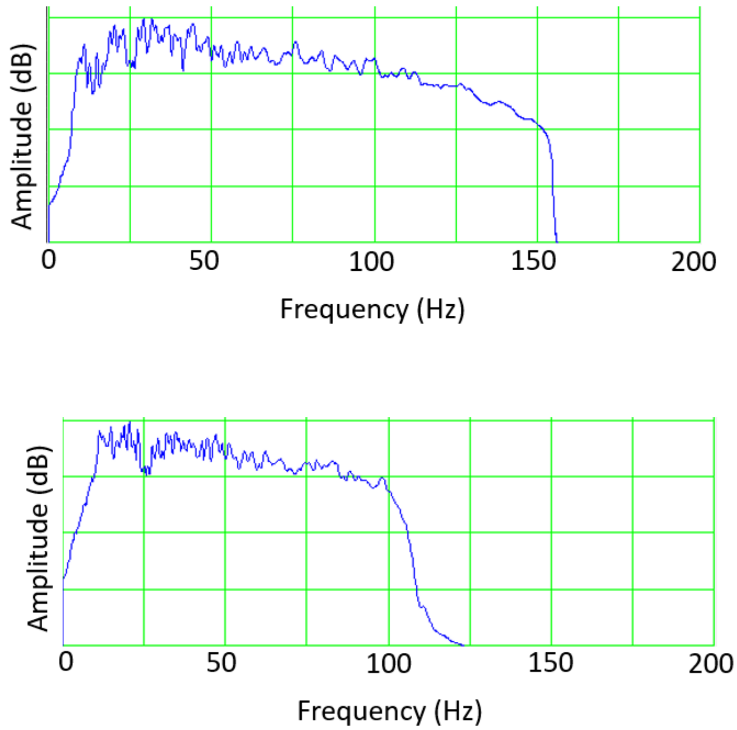

Figure 4-2. Amplitude spectra of the commercially processed PP seismic data (top) and PP-PS jointly processed seismic data (bottom)

4.1.1 PP synthetic seismogram and well tie

A sample synthetic seismogram and its correlation to the PP stacked seismic is shown in Figure 4-3. The synthetic seismogram was generated using despiked density and V_p well logs. The well-derived reflectivity sequence was convolved with a wavelet extracted from the seismic data. The synthetic seismogram (Figure 4-3) has a maximum crosscorrelation of 0.65, indicating a relatively close match between model and data.

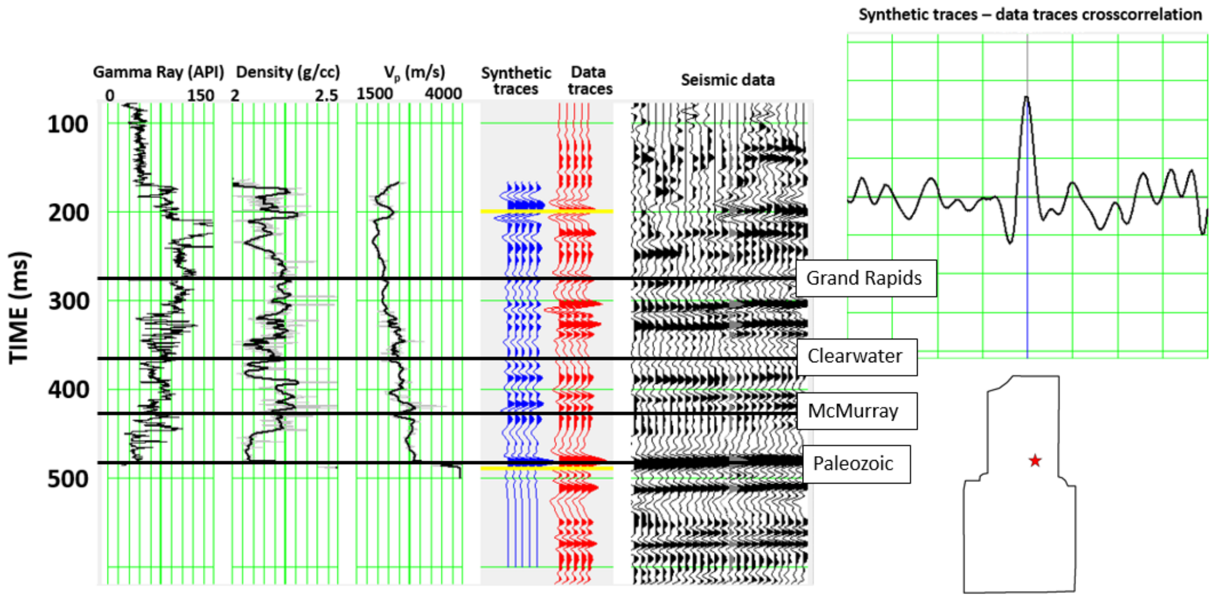

Figure 4-3. Synthetic seismogram for stacked PP seismic data. Synthetic traces in blue, seismic data traces in red. Maximum crosscorrelation of 0.650.

4.1.2 PP reflection interpretation

Seismic horizons (Figures 4-4 and 4-5) were picked utilizing the synthetic seismogram, the surface seismic data and the known geological tops from well logs. The reflection continuity is variable through the section. The Paleozoic, Clearwater and Grand Rapids horizons are nearly ubiquitous, but the McMurray and Colorado tops are more marginal picks. The Wabiskaw Member of the Clearwater Formation, which directly overlies the McMurray Formation, has similar lithology to the McMurray Formation and hence similar P-impedance. The low impedance contract between the two units is responsible for the poor reflection quality at the top of the McMurray formation on the PP seismic data. A zoomed cross section through the regional McMurray sequence is shown in Figure 4-6. The alternating regional sands and mudstones in the McMurray generate the three-cycle seismic sequence (Figure 4-6).

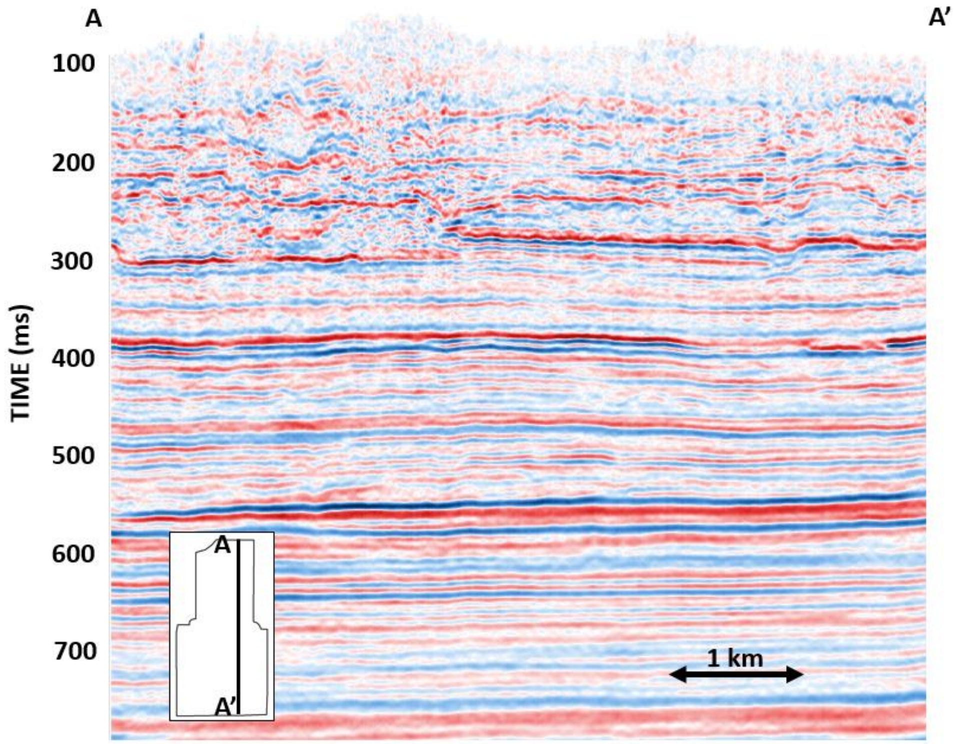

Figure 4-4. Seismic section without annotation

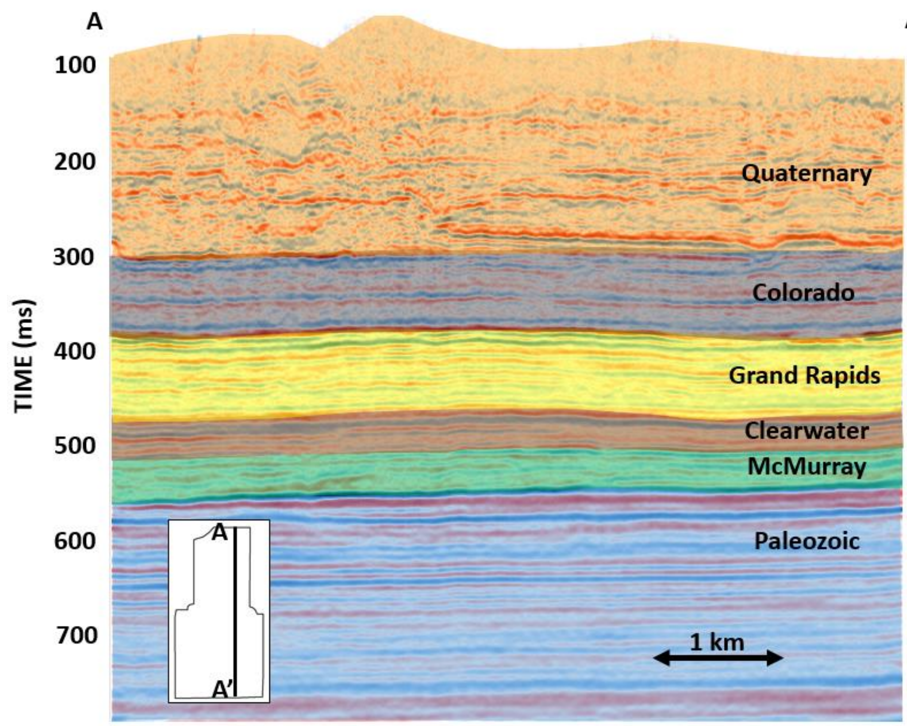

Figure 4-5. Seismic interpretation of the PP seismic data

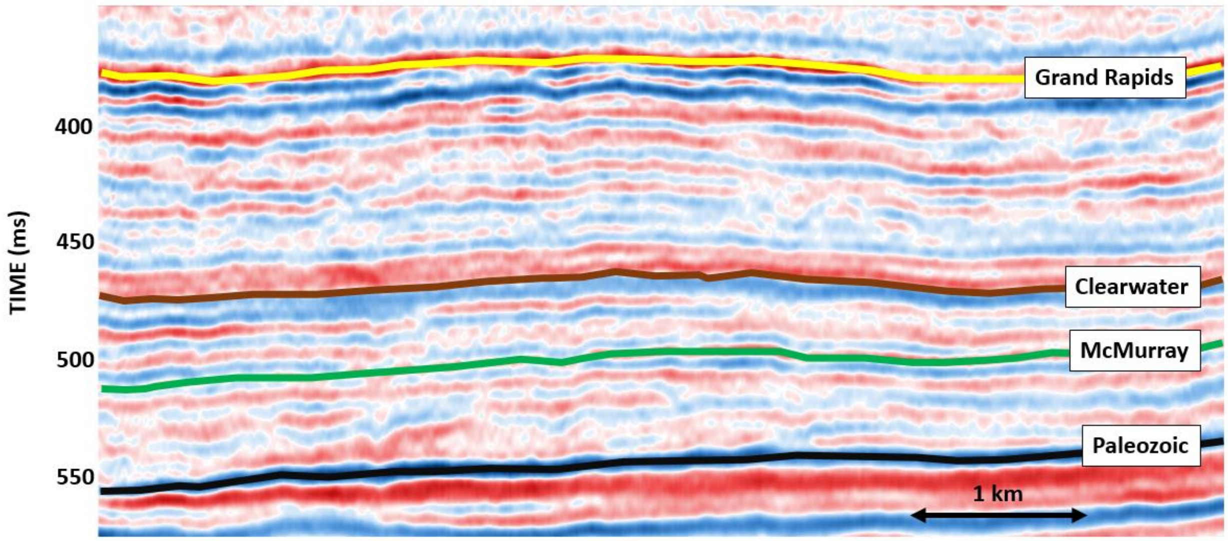

Figure 4-6. Zoomed in section through the Grand Rapids to Paleozoic interval. The typical regional McMurray 3-cycle sequence is present.

4.1.3 PP seismic data interpretation, McMurray Formation

The best quality reservoir is usually found not in the regional McMurray strata but in the large valley-fill systems cutting through the regional sequence. In seismic cross section, these valley systems will truncate the regional McMurray reflectors. Differential compaction plays a key role in the structure of the McMurray Formation. Mudstones will compress more than unconsolidated sandstones through diagenetic processes. Therefore, sandstones will be thicker, and the tops may have higher structural elevation. Time structure maps and isochron maps were used to find thick and structurally high zones. Paleozoic and McMurray time structure maps are shown in Figure 4-7. The topography of the Paleozoic Unconformity plays a vital role in determining the structure of the subsequent formations. The McMurray time structure closely follows the Paleozoic time structure (Figure 4-7), but the isochron between the McMurray and Paleozoic picks shows that there are lateral variations (Figure 4-8). A region with anomalously high isochron values is annotated on Figure 4-8. This high isochron zone also correlates with relatively high McMurray time structure (Figure 4-7). An amplitude stratal slice through the Middle McMurray shows the edges of the channel facies (Figure 4-9). The interpreted channel feature is different on the isochron (Figure 4-8) than the amplitude slice (Figure 4-9). The isochron shows the true position of the channel whereas the amplitude slice shows the position of the valley that contains the channel. The regionally extensive reflection horizons found within the McMurray are truncated by the valley incision (Figure 4-10).

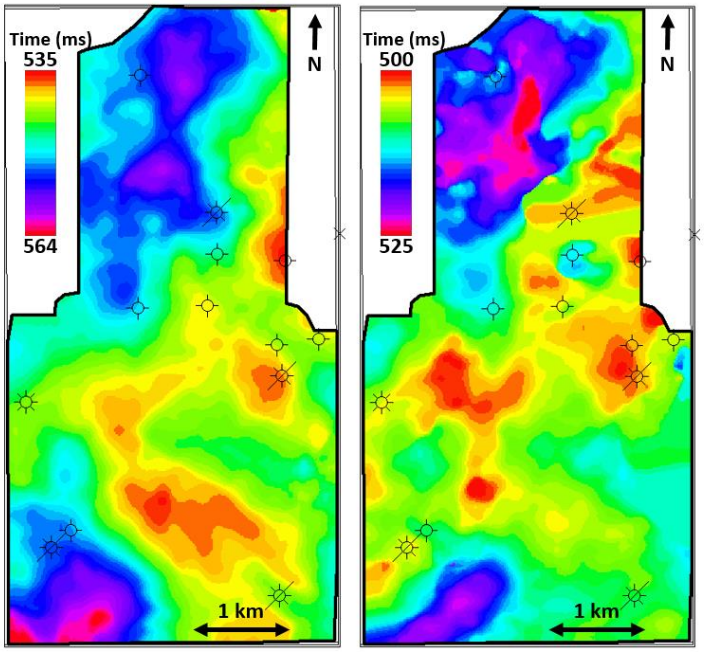

Figure 4-7. Paleozoic (left) and McMurray (right) PP time structure.

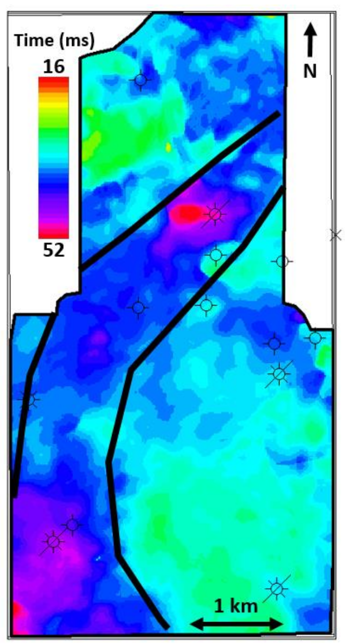

Figure 4-8. McMurray – Paleozoic PP isochron.

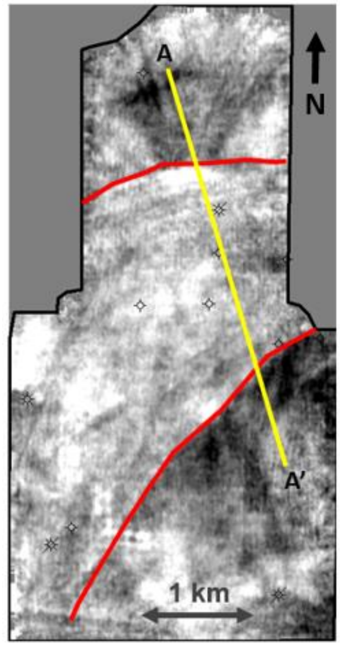

Figure 4-9. Middle McMurray stratal slice. Red Annotation indicates interpretation of channel fill edge, yellow annotation indicate cross section in Figure 4-12.

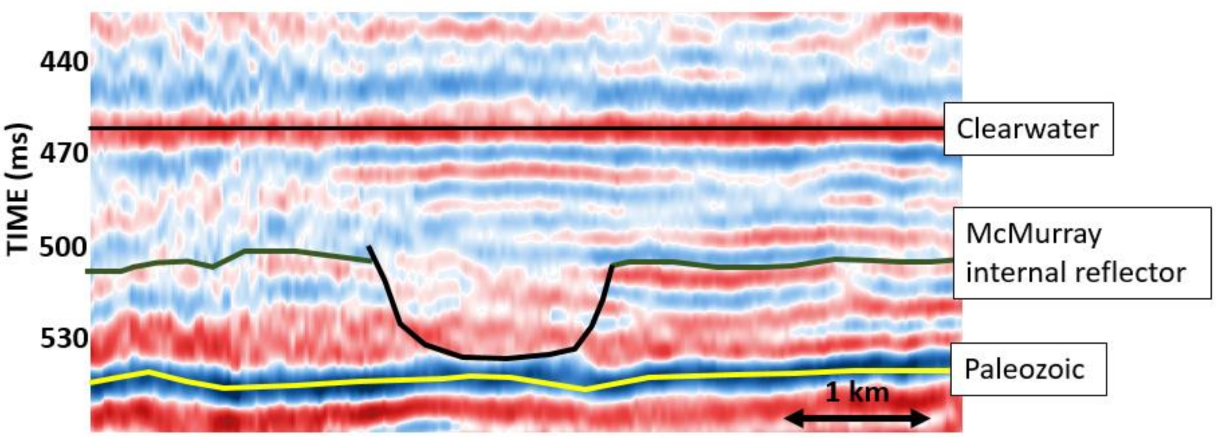

Figure 4-10. PP cross section through McMurray channel, regional McMurray reflections are truncated by channel edges.

Another key seismic property that can aid in understanding the McMurray reservoir is interval amplitude. Calculating a root mean square (RMS) seismic amplitude in a window can provide a measure of the average amplitude in said window. RMS maps were generated using the following algorithm: define a time window to calculate the RMS value, take the square of each sample and sum, divide by the number of samples and take the square root (equation 4-1). This process is applied to each trace generating an RMS amplitude value at every seismic bin location. It is important to note that RMS values are strictly positive.

$$x_{rms} = \sqrt{\frac{x_1^2 + x_2^2 + \cdots + x_n^2}{n}} \tag{4-1}$$

In the McMurray reservoir, high RMS amplitudes correlate to in-situ natural gas. Figure 4-11 shows an Upper McMurray RMS amplitude map and Figure 4-12 shows the RMS window chosen. Example well logs from wells penetrating the Upper McMurray show natural gas present in well A and show that well B is devoid of natural gas (Figure 4-13). In gas-saturated sandstones, the density porosity log and neutron porosity log will cross over. In gas saturated zones the neutron porosity log will underestimate the true porosity (Rider and Kennedy, 2011). Conversely, the density porosity log will overestimate the true porosity in gas saturated zones, due to the fact that the density porosity log is calibrated for sandstones. Well A (Figures 4-11 and 4-13), shows clear density and neutron porosity crossover and well B (Figures 4-11 and 4-13) does not.

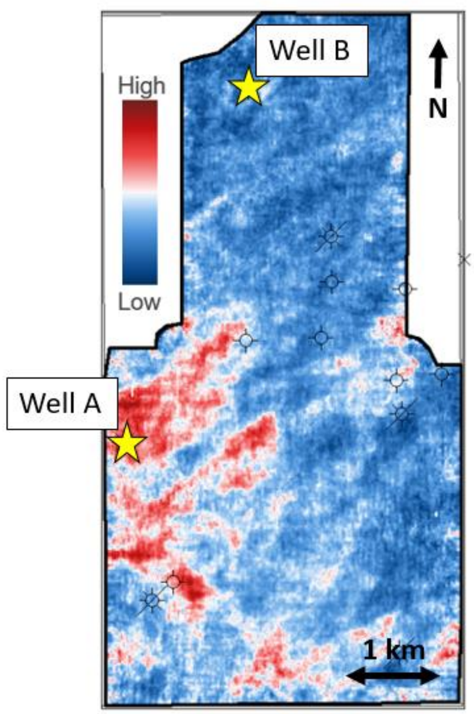

Figure 4-11. Upper McMurray RMS amplitude. Red zones correlate to in-situ natural gas. Yellow stars indicate example well positions.

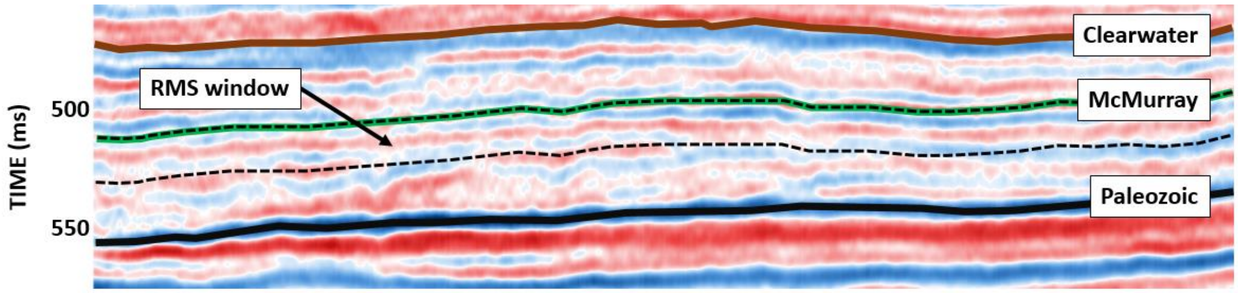

Figure 4-12. RMS window used to generate map in Figure 4-13. The dashed line coincident with the McMurray top and the dashed line within the McMurray represent the window.

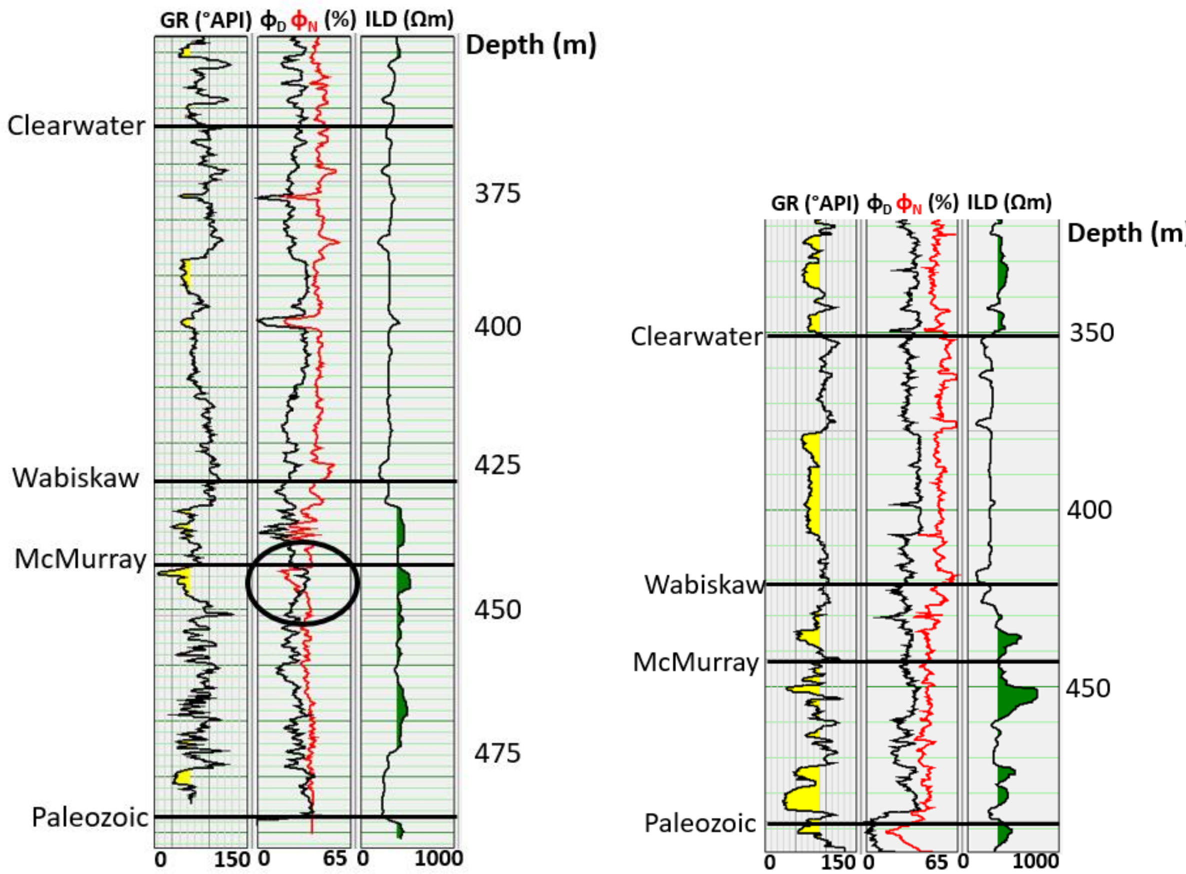

Figure 4-13. Well A displaying neutron and density porosity crossover – indicating in-situ natural gas (left) and well B showing no neutron and density porosity crossover – indicating no in-situ natural gas (right).

4.1.4 PP seismic data interpretation, Clearwater Formation

In addition to studying the reservoir, the interpretation tools described above were used to study other components of the stratal column. The Clearwater Formation, directly overlying the McMurray Formation, acts as an operational caprock for thermal oil sands production. The Clearwater Formation structure (Figure 4-14) has the same regional features as the Paleozoic and McMurray time structure (Figure 4-7). An amplitude time slice through the Clearwater Formation (Figure 4-14) has no large regional anomalies, as expected for a marine mudstone. The isochron map between the Clearwater Formation top and the McMurray formation top is mostly uniform with no significant anomalies.

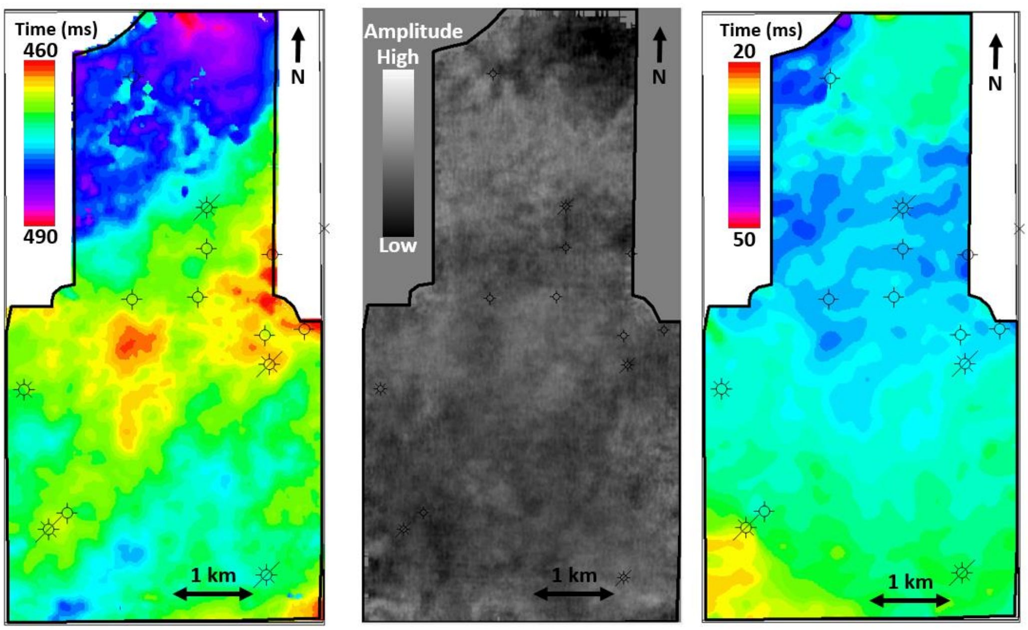

Figure 4-14. Clearwater Formation PP time structure (left), amplitude slice (center) and Clearwater – McMurray isochron (right).

4.1.5 PP seismic data interpretation, Grand Rapids Formation

Overlying the Clearwater Formation is the Grand Rapids Formation, which is comprised of a relatively thick sequence of high porosity, coarsening-upward shoreface sequences with many incised channels. The Grand Rapids forms a major hydrocarbon reservoir in other parts of the Western Canadian Sedimentary Basin. For instance, in the Cold Lake Oil Sands, the Lower Grand Rapids is targeted for thermal oil sands production (Willmer and Quinn, 2015) and in the

Lloydminster region, heavy oil is produced from the Grand Rapids Formation through Cold Heavy Oil Production with Sands (CHOPS) (Vigrass, 1968). The Grand Rapids time structure is shown in Figure 4-15, and illustrates the same regional trends as the lower geological units except for in the southern part of the map, where there is a structurally deeper zone. This deeper section represents a channel that exists in the youngest part of the Grand Rapids Formation. The young channel can be easily identified on an amplitude slice through the Upper Grand Rapids (Figure 4-15). A complicated system of cross cutting channels is clearly visible on the time slice, and this is commonly observed throughout the Grand Rapids Formation in the Athabasca Oil Sands. Isochron values over the Grand Rapids – Clearwater interval show a thinning in the vicinity of the young channel identified from the time structure map. Otherwise, the time thickness of the Grand Rapids Formation is consistent, with no large anomalies.

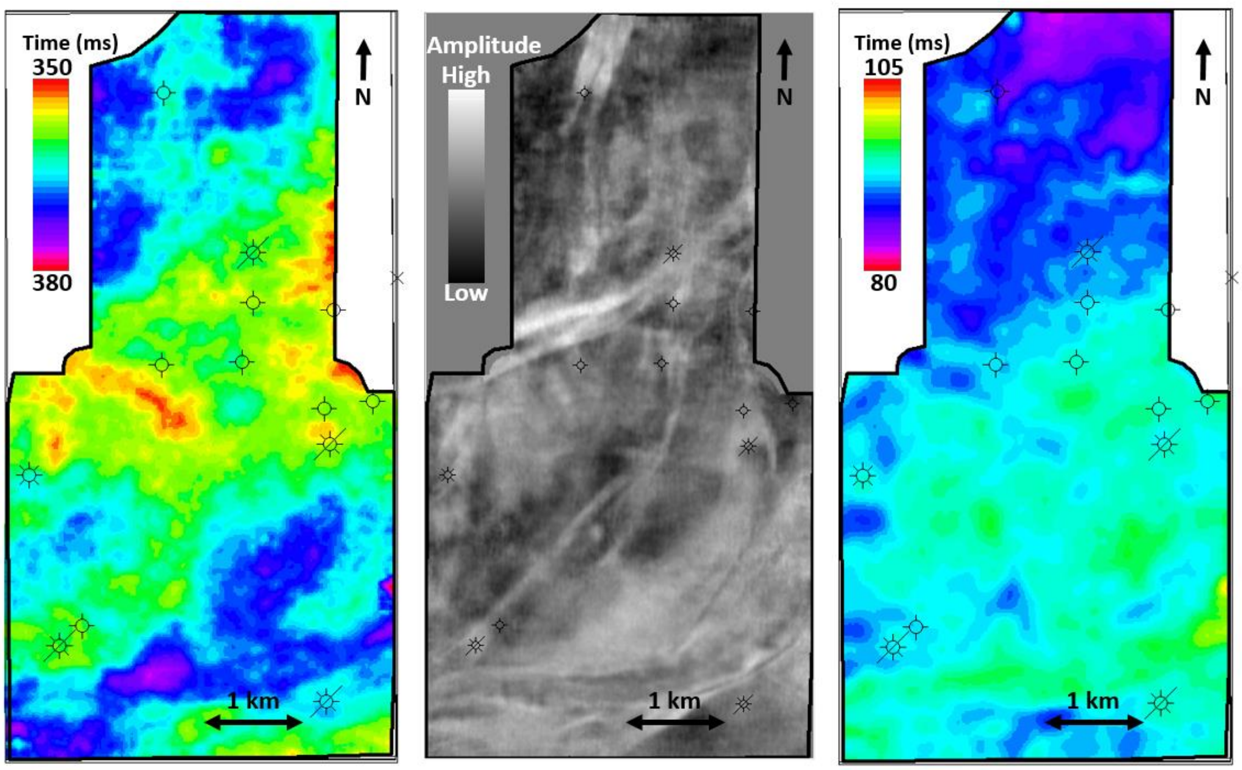

Figure 4-15. Grand Rapids Formation PP time structure (left), amplitude slice (center) and Grand Rapids – Clearwater isochron (right).

4.1.6 PP seismic data interpretation, Colorado Group

The Cretaceous Colorado Group lies above the Grand Rapids Formation. The Colorado group is a thick marine mudstone bounded both above and below by unconformities. On the PP seismic data the top of the Colorado Group does not exhibit a particularly extensive reflection horizon and is not easily picked. A Colorado Group equivalent horizon pick was created to represent a best guess for the top of the Colorado Group, and the time structure map is shown in Figure 4-16. The time structure shows a low trend in the western part of the data with a North-South orientation, otherwise the map has similar regional features to the Paleozoic, McMurray, Clearwater and Grand Rapids time structure maps. The low feature in the western part of the data is a large Quaternary channel incision into the Colorado Group. Clear edges of this lower Quaternary channel feature are visible on an amplitude time slice (Figure 4-17). An amplitude time slice through the Middle Colorado Group (Figure 4-16) shows similar character to the Clearwater Formation amplitude slice (Figure 4-15). The Middle Colorado amplitude time slice shows quiescent character with no anomalies. The effect of the quaternary channel incision on the Colorado Group time structure is also visible on the Colorado Group isochron (Figure 4-16). The structure of the Quaternary – Colorado unconformity is the main structural control for the Colorado Group isochron.

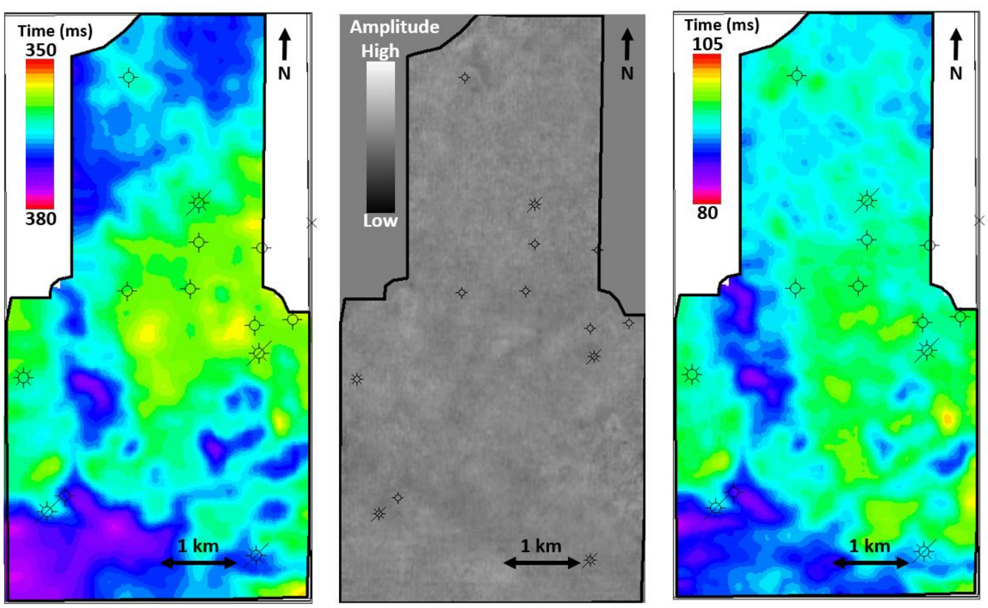

Figure 4-16. Colorado Group PP time structure (left), amplitude slice (center) and Colorado – Grand Rapids isochron (right).

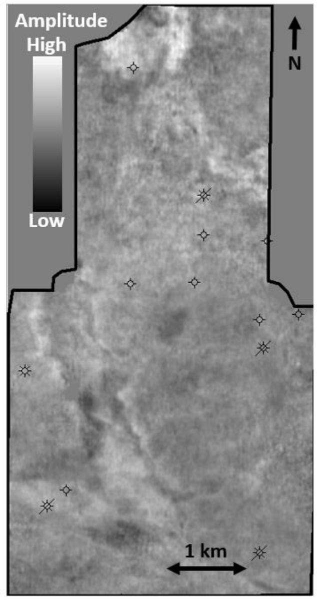

Figure 4-17. Upper Colorado Group time slice displaying Quaternary channel edges. Channel trends North-South in the southwest part of the map.

4.2 PP-PS seismic data registration

An important tool in joint PP-PS interpretation is registration of the converted wave seismic volume. The process of PP-PS registration converts the PS data from the PS time domain to the PP time domain. The data can be more directly compared after the registration process. In addition, joint inversion requires PS seismic data to be in the PP time domain. A useful byproduct output by the PP-PS registration process is a coarse V_p/V_s volume. Many manual and automatic registration algorithms have been proposed. Nickel and Sonneland (2004), proposed an automatic PP-PS registration method where delay time between the PP and PS seismic data is obtained by applying an image processing technique where displacement between the two seismic volumes is estimated. Fomel and Backus (1999) presented a semi-automatic registration algorithm where by using an initial interpretation, the matching error between PP and PS traces is minimized. A solid initial interpretation prevents the error from becoming trapped in a local minimum. A simple way to register PP and PS seismic data is to simply match known geological horizons. If there are high quality, regionally extensive reflection horizons common to both the PP and PS seismic data, a nonstationary warping shift can be determined in order to change the PS seismic data to the PP time domain.

In this project, PP and PS seismic data were registered through a simple horizon matching methodology. The Grand Rapids Fm, the Clearwater Fm and the Paleozoic Unconformity are regionally extensive geological interfaces which generate high quality reflections on both the PP and PS seismic data volumes. A non-stationary warping shift, calculated by horizon matching, was applied to the PS seismic data. Figure 4-18 shows a PP seismic data example and the coincident PS seismic data which has been registered to PP time. The PS seismic data contains less high frequency content than the PP seismic data.

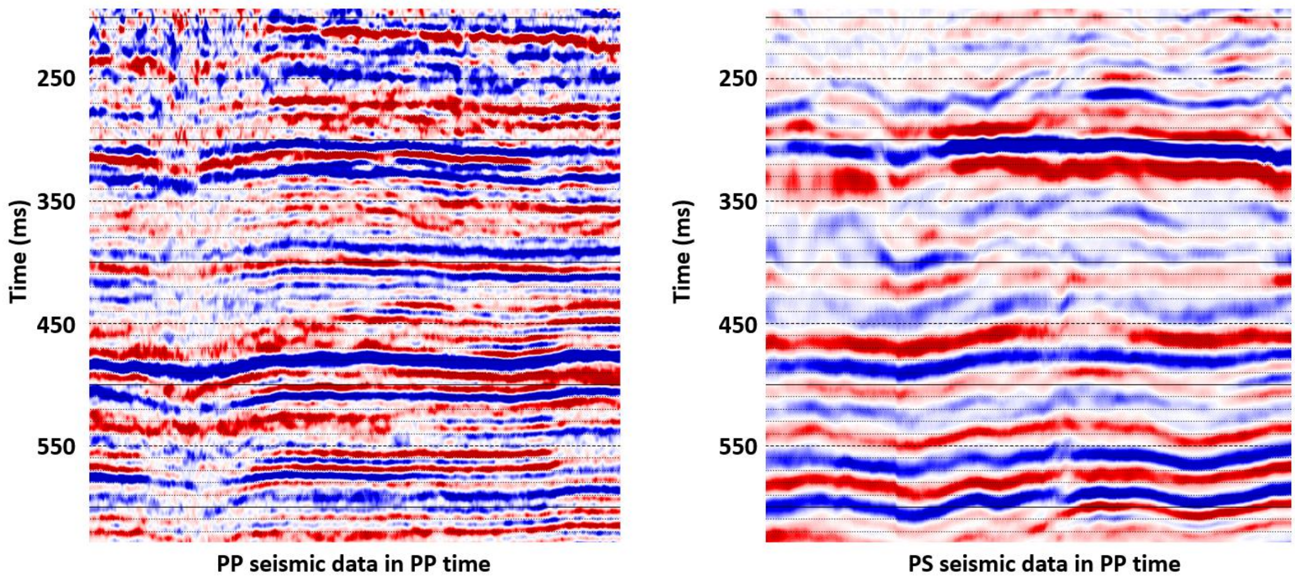

Figure 4-18. PP seismic data and coincident PS seismic data registered in the PP domain.

4.3 PS seismic interpretation

4.3.1 PS synthetic seismogram and well tie

The interpretation of the PS seismic data volume followed the same first steps as the PP interpretation. Generating converted wave synthetic seismograms is a more involved process than for the PP case. For creating PP synthetic seismograms, P sonic and density well log curves were used to create an impedance log from which reflectivity is calculated. A wavelet characteristic of the seismic data was convolved with the reflectivity sequence to obtain the synthetic seismogram. This methodology gives a representation of the PP seismic behaviour at normal incidence, but we know that PS reflectivity is zero at normal incidence. PS reflectivity was calculated for the range of incident angles in the gather using the Zoeppritz equations, P sonic, S sonic and density logs.

Characteristic wavelets for the PS seismic data were convolved with the calculated reflectivities to output synthetic seismograms. Several different offset angle synthetic seismograms were correlated to the seismic data. The PS synthetic which gave the largest maximum cross correlation with the PS seismic volume was used for interpretation. Figure 4-19 shows a PS synthetic seismogram created with Hampson-Russell software. The calculated reflectivity offset angle for the synthetic seismogram in Figure 4-19 was 20 degrees. The maximum value of the crosscorrelation between the synthetic traces and the data traces was 0.667 which implies a relatively strong linear relationship and a good synthetic tie. As a quality control check, a second PS synthetic seismogram was created using CREWES' Syngram software (Figure 4-20). The Syngram synthetic shows the response for the full range of offset angles. The zero reflectivity at normal incidence is demonstrated by the variable offset synthetic seismogram. To mimic the effect of an nmo mute, the multi-offset synthetic seismogram was given a maximum offset to depth ratio of 1, beyond which data were muted. The differences between the Hampson-Russell software (Figure 4-19) and Syngram (Figure 4-20) synthetic seismograms arise from differences in the chosen wavelet. In the Hampson-Russell synthetic seismogram a wavelet was statistically extracted from the coincident PS seismic data, whereas an Ormsby wavelet was used to generate the Syngram synthetic seismogram.

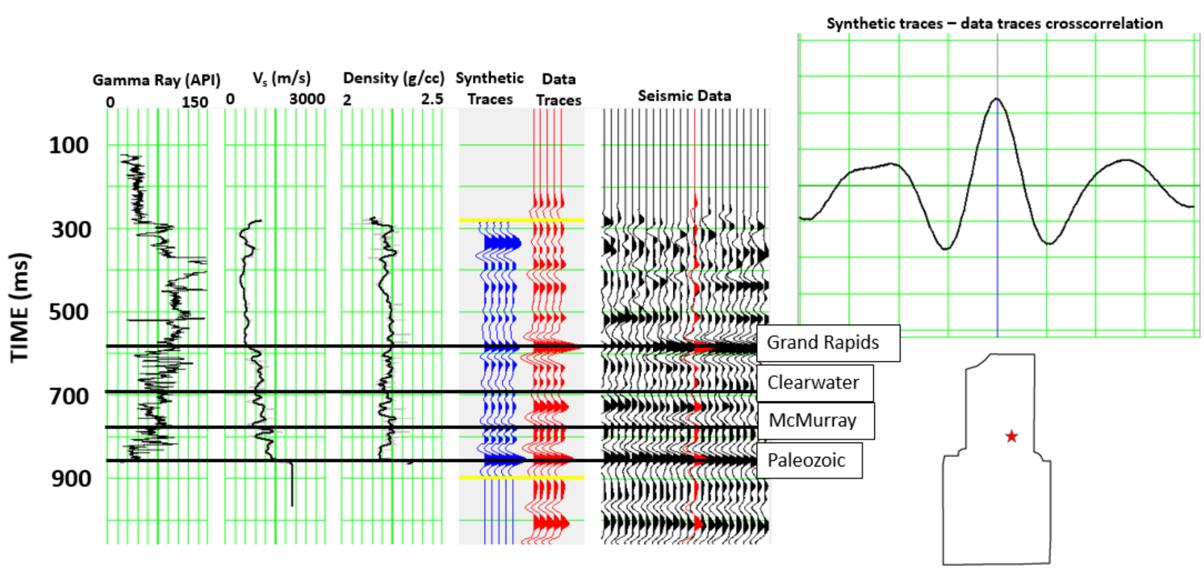

Figure 4-19. PS synthetic seismogram.

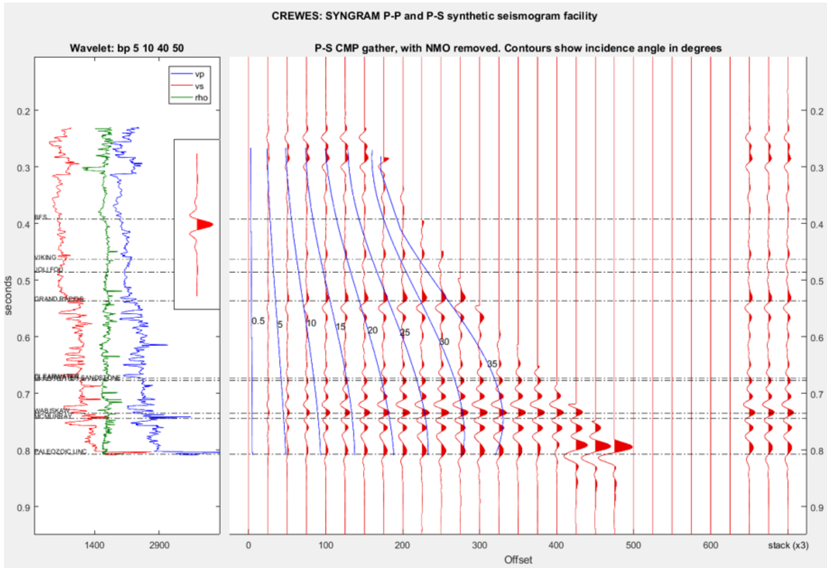

Figure 4-20. PS multi-offset synthetic seismogram and stacked synthetic seismogram using Syngram software.

4.3.2 PS reflection interpretation

Continuous PS reflections were defined after correlating the data to well logs. Figures 4-21 and 4-22 show a PS seismic section with and without annotation, respectively. All major geologic discontinuities correlate to pervasive seismic reflection horizons with the exception of the Quaternary-Colorado boundary. We interpret that, the reflection quality is good for the Paleozoic, McMurray, Clearwater and Grand Rapids events. The McMurray reflection is much more regionally extensive on the PS seismic data compared to the PP seismic data. One of the main reasons that converted-wave seismic sections are not used extensively in the hydrocarbon exploration industry is because it is hard to quantify to what extent PS seismic sections improve the interpretation completed on a PP seismic section alone. The fact that the top of the main reservoir interval produces a better quality PS reflection than PP reflection is one reason for justifying acquiring and processing converted wave seismic data in an oil sands setting. The high frequency content of the PS seismic data (Figure 4-23) is low compared to the PP data (4-2), as the high frequency data in are attenuated much more readily than in compressional waves and even more so in unconsolidated sediments such as those found in the Athabasca Oil Sands.

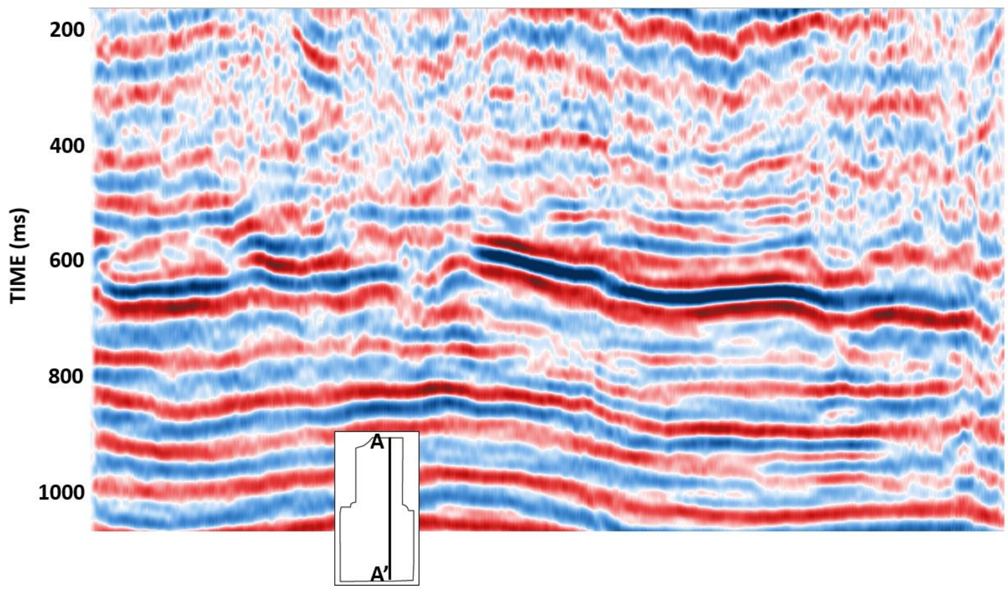

Figure 4-21. Inline cross section through stacked PS seismic data.

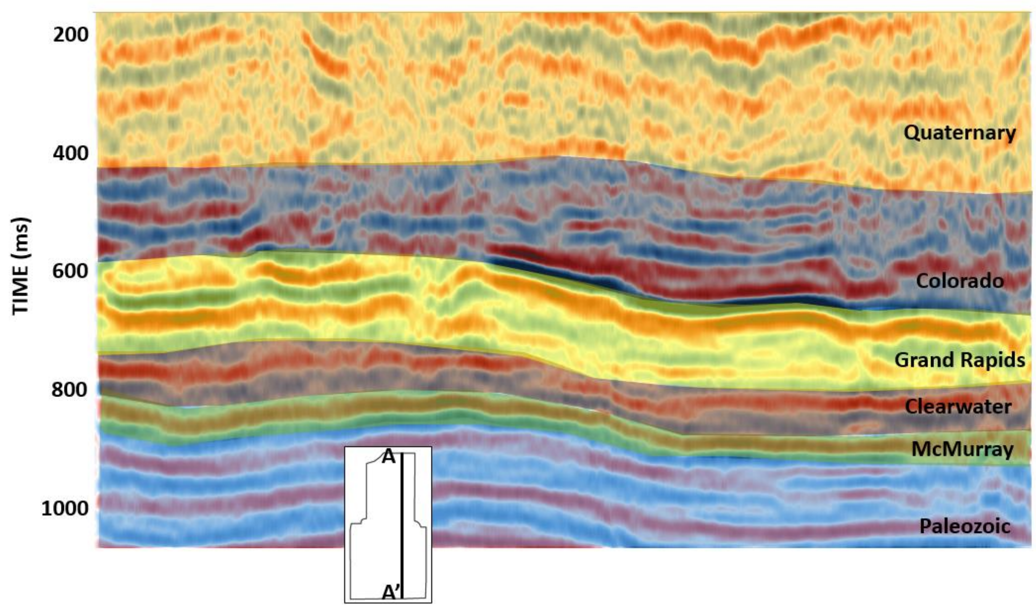

Figure 4-22. Annotated inline cross section through stacked PS seismic data.

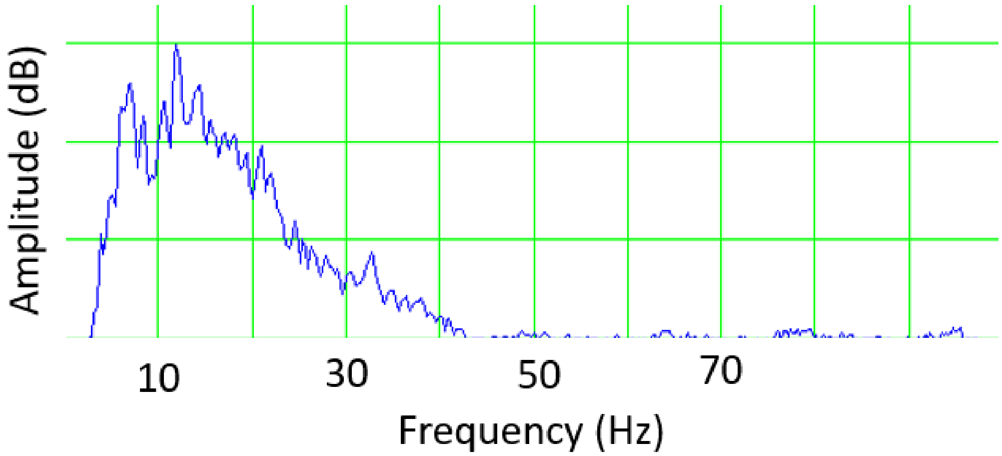

Figure 4-23. PS seismic data frequency spectrum in the interval of interest (300-1000 ms).

4.3.3 PS interpretation, McMurray Formation

We also studied the previously interpreted McMurray channel on the converted-wave seismic sections. The obvious truncations that are seen on the channel edges on the PP seismic data are not present on a PS cross section, however, there is an interruption of the seismic character across the known channel position (Figure 4-24). An interval RMS amplitude map of the Upper McMurray for the converted wave seismic data is shown in Figure 4-25, in which the approximate position of the McMurray channel is highlighted. The position of the channel was taken from the PP time structure and isochron, specifically the region within in the McMurray with shallow time structure and thick PP isochron values. The RMS amplitudes within the McMurray are highly variable. Generally, within the McMurray channel the PS RMS amplitudes are higher than the surrounding strata. Comparing two gamma ray well logs penetrating regions with differing RMS PS amplitude in the McMurray channel shows that better quality sands correlate with larger RMS PS amplitudes (Figure 4-26).

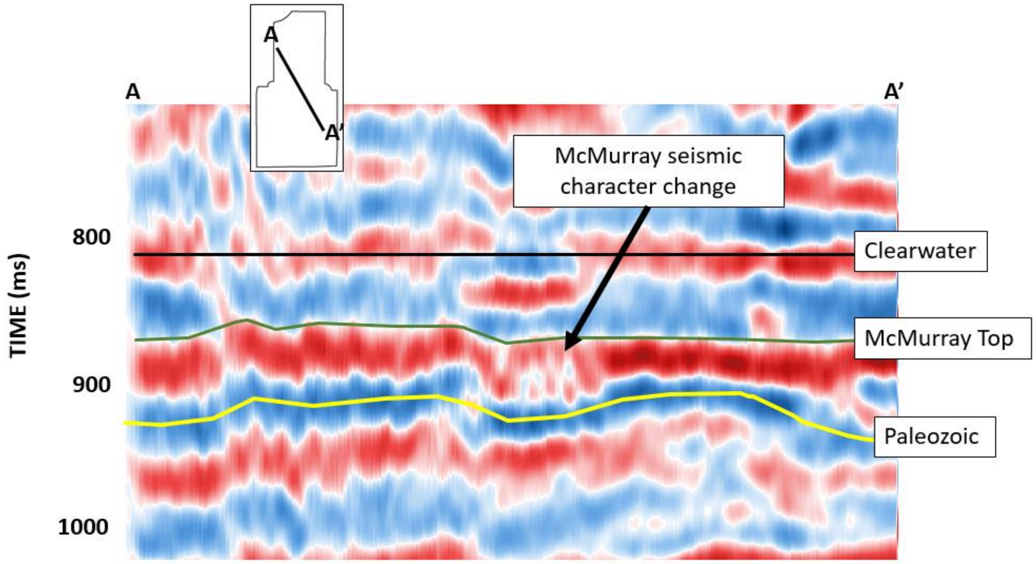

Figure 4-24. PS cross section through McMurray channel.

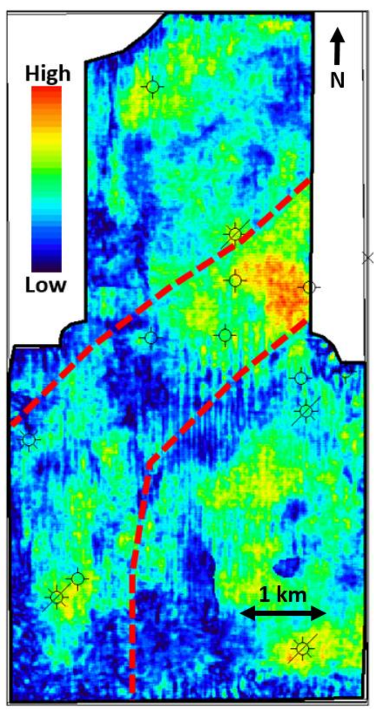

Figure 4-25. Converted wave interval RMS amplitude for the Upper McMurray. Approximate position of the McMurray channel is annotated in red.

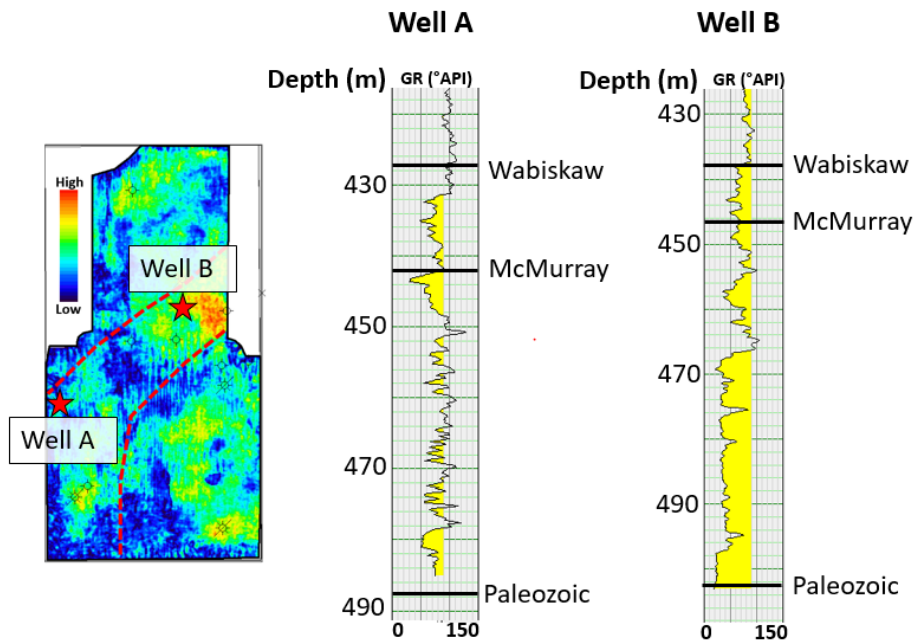

Figure 4-26. Gamma ray logs through low RMS PS amplitude and high RMS PS amplitude in the McMurray channel.

4.3 Horizon-based interval V_p/V_s

Using only isochron maps from the PP and PS seismic volumes, interval V_p/V_s values wer found, using equation 4-2. The variables, Δtpp and Δtps, are defined as PP and PS isochron times respectively.

$$\frac{V_p}{V_s} = 2\frac{\Delta t_{ps}}{\Delta t_{pp}} - 1 \tag{4-2}$$

Interval V_p/V_s is an effective way to obtain a physical rock parameter without inversion. Picking uncertainty has a very large effect on interval V_p/V_s so it is very important to use large intervals to reduce this error. For example, when creating an interval V_p/V_s map for the McMurray-Paleozoic interval large anomalies could stem from improper horizon picks. In Figure 4-27, very high V_p/V_s zones are a result of bad picks instead of actual rock properties. To generate a better map a larger interval, from the Grand Rapids to the Paleozoic, was used (Figure 4-27). The V_p/V_s map is much less sensitive to minor picking errors in this larger interval, but edge effects are still present. An erroneous V_p/V_s value (of 1) exists in the northwest corner of the Grand Rapids -

Paleozoic V_p/V_s map. Unfortunately, due to the large intervals that must be used to obtain adequate interval V_p/V_s maps, it is challenging to make detailed reservoir interpretations. Thus, interpretation of interval V_p/V_s maps is limited to large scale, regional interpretations, which are still valuable. Horizon based interval V_p/V_s can also be used to quality control inversion results. Comparing horizon based interval V_p/V_s maps to inversion based RMS or interval average maps and correlating back to geological control can give a sense of the accuracy of the results.

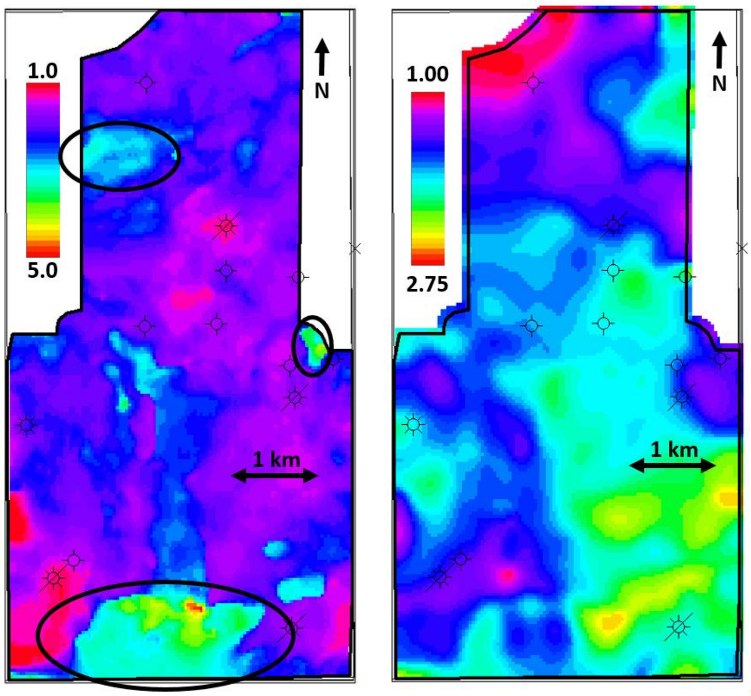

Figure 4-27. Horizon based interval V_p/V_s for the McMurray – Paleozoic interval (left) and the Grand Rapids – Paleozoic interval (right). Black ellipses on the McMurray – Paleozoic interval map indicate regions with poor horizon picks.

4.5 Discussion

Seismic reflections were interpreted for the PP and PS data volumes. Regionally extensive PP reflections were found for the Paleozoic Unconformity, the Clearwater Fm and the Grand Rapids Fm, with more marginal reflection quality found for the McMurray Fm and the Colorado Gp. For the PS seismic data volume, with the exception of the Colorado Gp, all of these main geologic interfaces have good quality, continuous reflections. Within the main reservoir interval (McMurray Fm) a structurally high, thick isochron anomaly was found and interpreted to be a channel incision and fill. The edges of this feature were clear on PP amplitude stratal slices. In PP and PS cross section, the regional McMurray reflection sequence was truncated by the edges of this large channel.

The distribution of natural gas within the McMurray Fm was found using interval RMS amplitude maps on the PP seismic data. High interval RMS amplitudes correlated to in-situ natural gas. Well logs in the high RMS amplitude zones displayed density porosity and neutron porosity log crossover indicating the presence of these hydrocarbons and well logs in low RMS amplitude zones showed no porosity log crossover.

Stratigraphically younger units were also studied. A complex system of cross cutting channels was found in the Grand Rapids Fm. The Clearwater Fm Colorado Gp marine shales were found to have uniform amplitude slices as expected for a mudstone. However, a large Quaternary channel feature was identified in the Upper Colorado Group.

Some PP-PS registration algorithms were discussed. The registration methodology used in this project was a relatively simple horizon based process. This methodology warps PS data by stretching and squeezing coincident PP and PS reflection horizons. The best three horizons were used in the registration process: the Grand Rapids Fm, the Clearwater Fm and the Paleozoic Unconformity.

Interval V_p/V_s maps were generated using the isochrons from the PP and PS seismic data volumes. It was found that large intervals must be used to reliably create interval V_p/V_s maps. Picking errors propagate into large anomalies when small intervals were used to make the V_p/V_s maps.

CHAPTER 5: SEISMIC INVERSION AND ROCK PHYSICS

Several different inversion methodologies were used in attempt to interpret rock properties from the seismic data and well logs. Deterministic and probabilistic tools were used and compared. The first technique to obtain a physical rock parameter was post-stack model-based PP impedance inversion, following the generalized linear inversion (GLI) methodology laid out by Cooke and Schneider (1983). In post stack PP impedance inversion the only output is P impedance. Pre-stack inversion of PP angle gathers was then undertaken; this follows a similar algorithm to post-stack inversion but has more outputs: P impedance, S-impedance and density. An inversion process using both the processed PP and PS seismic data was then performed. PP-PS joint inversion provides the same outputs as pre-stack inversion: P impedance, S-impedance and Density. From the pre-stack or joint inversion outputs, geomechanical properties can be calculated. Young's Modulus and Poisson's Ratio were calculated from the PP-PS joint inversion outputs, which had a better correlation to blind well logs than the pre-stack inversion outputs. After interpreting the geomechanical property volumes, linear and nonlinear multiattribute analysis was investigated. Gamma ray volumes were created by finding a statistical relationship between well log values and inversion outputs values. Gamma ray was selected as the prediction objective because it is the most useful well log in facies identification in the project area.

5.1 Post-stack model-based PP impedance inversion

5.1.1 Post-stack inversion setup and inputs

Model based GLI requires three main components: the processed seismic data, a wavelet and an input low frequency impedance model. The wavelet (Figure 5-1) was obtained from the seismic data by first choosing a time window representing the interval of interest (Colorado Gp – Paleozoic Unconformity). Then, the autocorrelation of each trace in the window was calculated and the Fourier transform was taken. The square root of the amplitude spectrum of the autocorrelation is approximately the amplitude spectrum of the desired wavelet, thus an inverse Fourier transform then produced the wavelet. The low frequency model was generated based on the regional seismic interpretation and a regionally characteristic well log from within the 3D seismic data volume (Figure 5-2). In GLI, a seismic trace is forward modeled from the low frequency impedance model and the inversion wavelet, the difference between the true seismic trace and the forward modeled trace is found, and the model is updated based on the difference.

The objective of this inversion methodology is to minimize the difference between the modeled trace and the observed trace. Several iterations of forward modeling and model updating were done in order to minimize the error. A flowchart for GLI is shown in Figure 5-3.

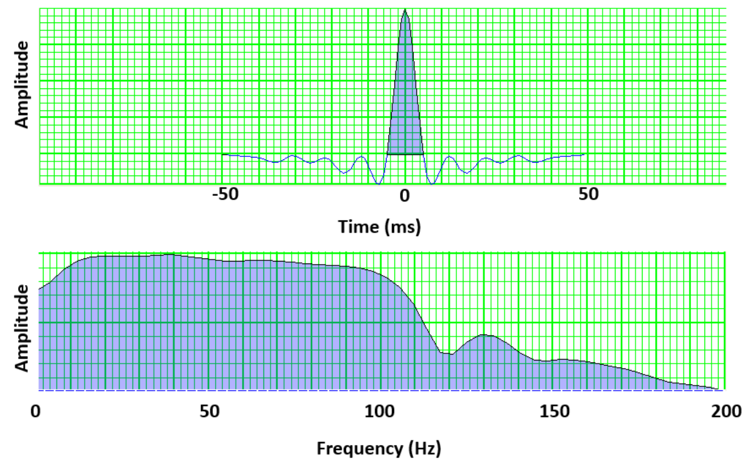

Figure 5-1. Wavelet used in PP impedance inversion, statistically extracted from PP seismic data.

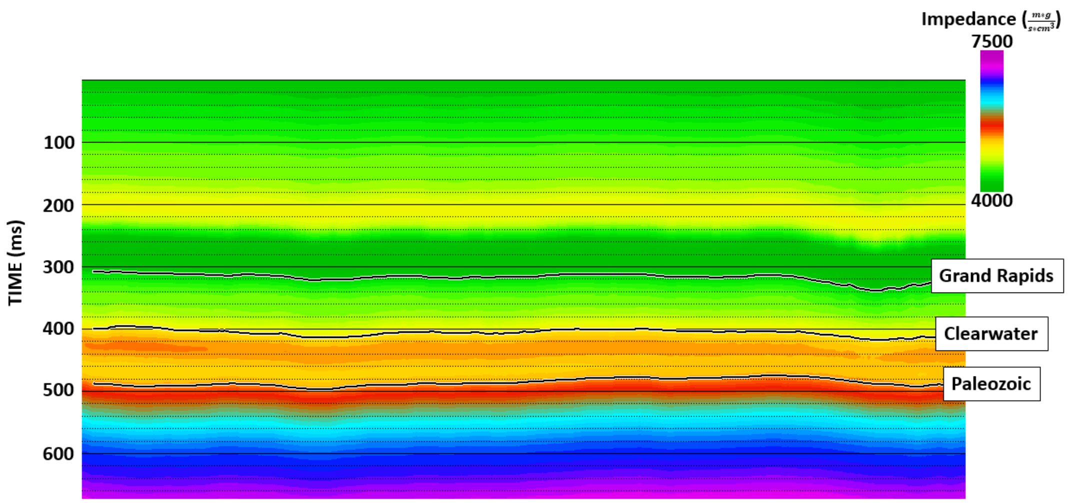

Figure 5-2. Low frequency input model used in PP impedance inversion.

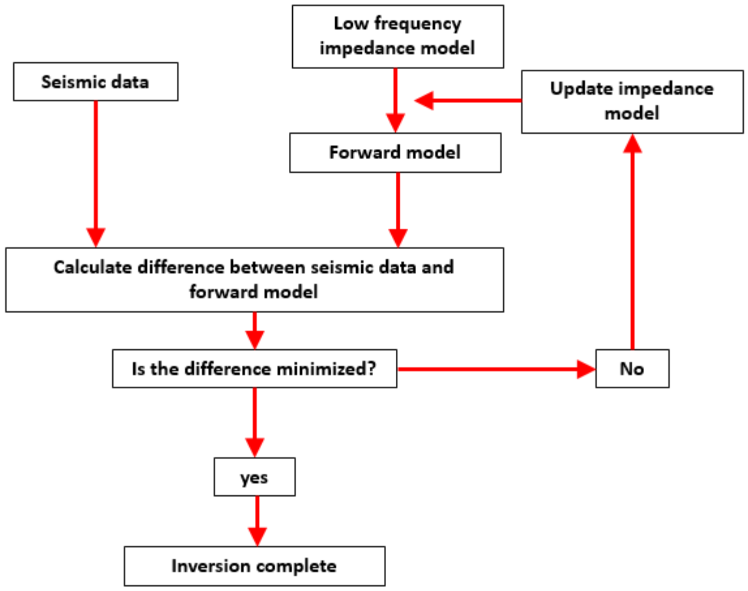

Figure 5-3. Generalized linear inversion flowchart

5.1.2 Post-stack inversion outputs and analysis

An example cross section from the PP impedance output is shown in Figure 5-4, including a blind well log impedance test. The well log was not at all involved in the inversion process making it "blind," that is, the inversion result is mathematically independent of the shown well log. A comparison between the blind well log and the inversion result provides a qualitative estimate of the accuracy of the inversion. In Figure 5-4, the blind well log impedance and the seismic inversion impedance match fairly well, particularly in the zone of interest (below 400 ms). A more quantitative quality control measure is to directly cross plot the inversion trace with the well log impedance. Figure 5-5 shows blind well log P impedance, seismically derived P impedance and the two traces cross plotted. The correlation coefficient of the cross plot is 0.716, implying a reasonably strong linear relationship between the two and hence a good post stack impedance inversion.

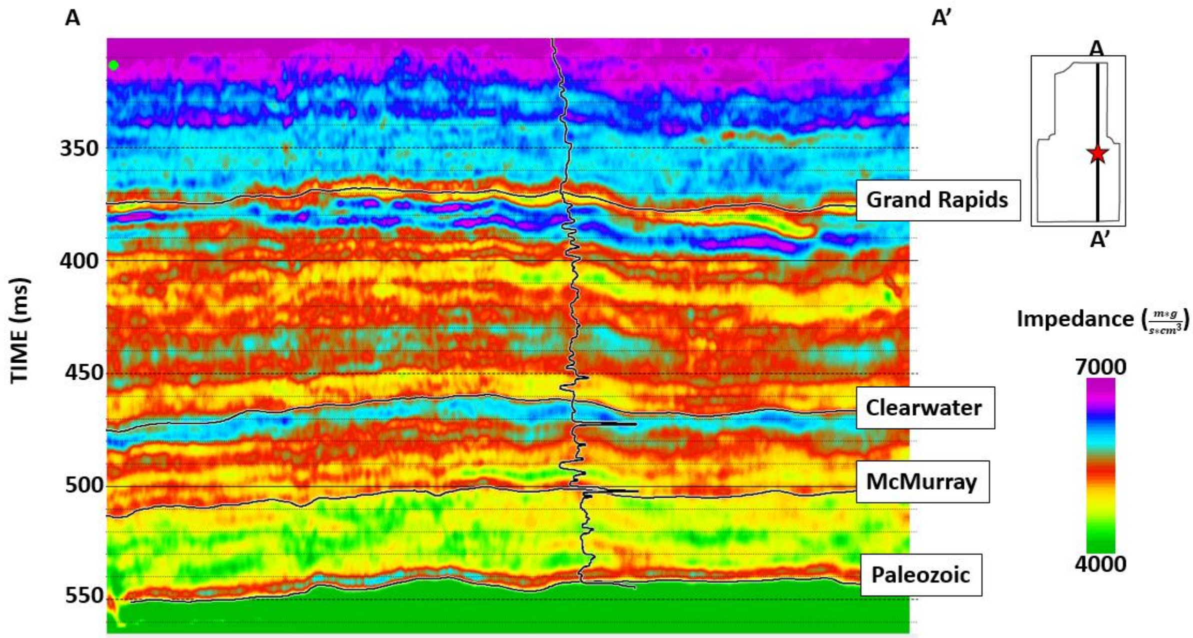

Figure 5-4. Example cross section of PP impedance from post-stack inversion. A superposed blind well log shows qualitative similarities between the inversion result and well data.

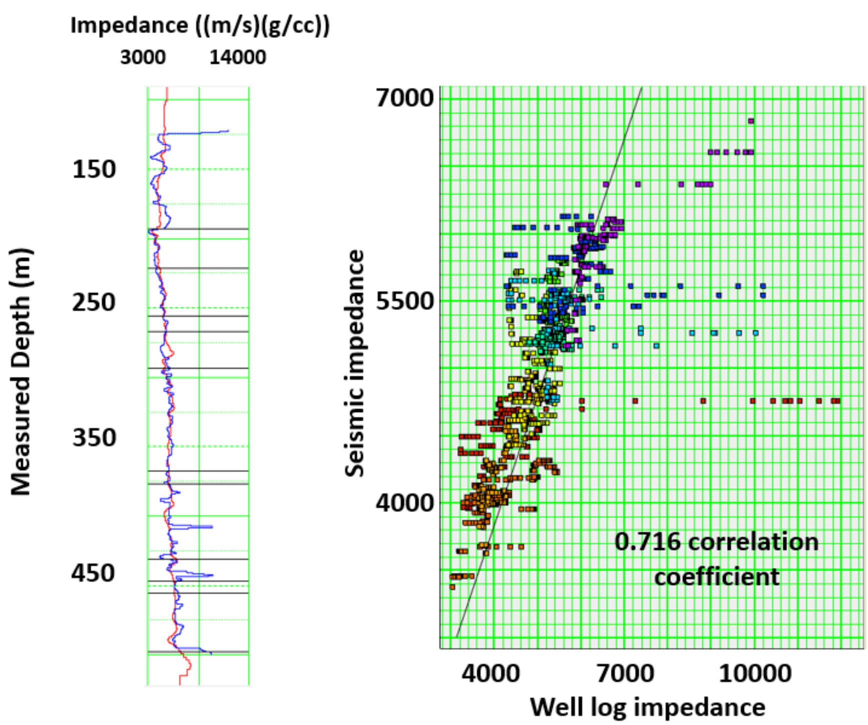

Figure 5-5. Blind well log impedance versus seismic impedance: trace values (left) and cross plot (right). Well log is in blue, inversion trace is in red.

When jointly interpreted with the corresponding seismic data with the well control, the P impedance volume can add to the conventional interpretation of the seismic data and well data. Figure 5-6 depicts Upper McMurray Formation interval average impedance, and shows a trend of high impedance in approximately the same position as the McMurray channel interpreted in Chapter 4. When correlated with well control, the high average impedance zones tend to coincide with regions with better reservoir quality. For example, Well B (Figure 5-7), which lies in a region with relatively high RMS impedance, displays a lower gamma ray reading (GR), higher porosity (ϕ_D, ϕ_N) and higher resistivity (ILD) in the McMurray than Well A (Figure 5-7), which lies in a region with lower average impedance. Directly comparing the P impedance inversion results to the coincident seismic data shows that geologic boundaries are more apparent on the P impedance volume (Figure 5-9). More detail is interpretable on the P impedance section, particularly within the McMurray Formation, because of the improved resolution after inversion. From the well log calibration, the best reservoir will be encountered in regions with higher P impedance. There are clear high impedance anomalies within the McMurray Formation in the centre of the P impedance cross section, which coincides with be the position of the McMurray channel.

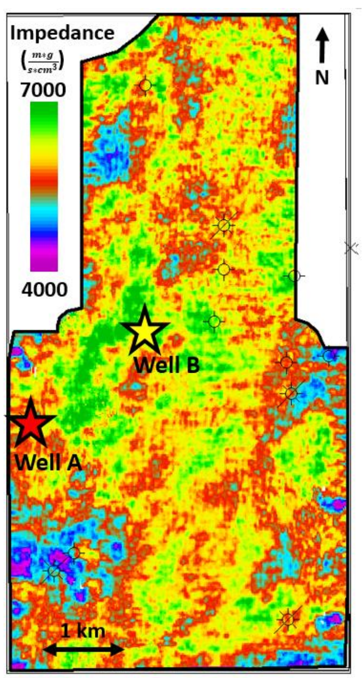

Figure 5-6. Upper McMurray interval average impedance. Well log positions from Figure 5-7 are labeled.

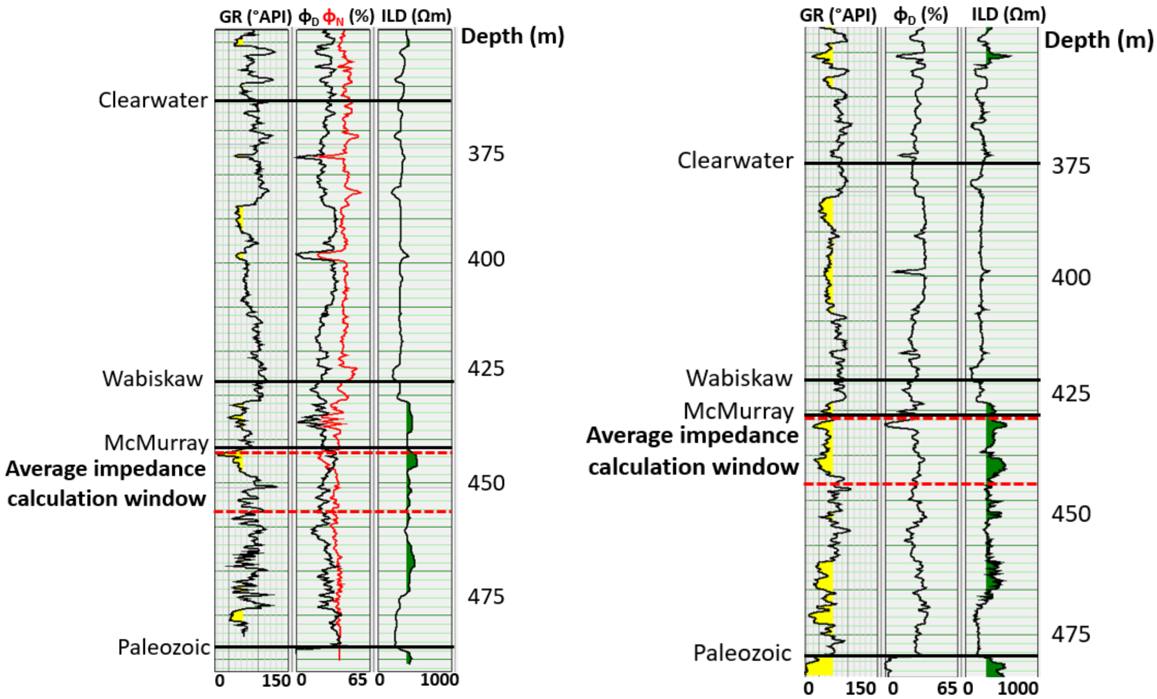

Figure 5-7. Logs from Well A (left) and Well B (right), interval average P impedance is Lower in Well A than Well B. GR is the gamma ray log, ϕ_D and ϕ_N are density and neutron porosity and ILD is the resistivity log.

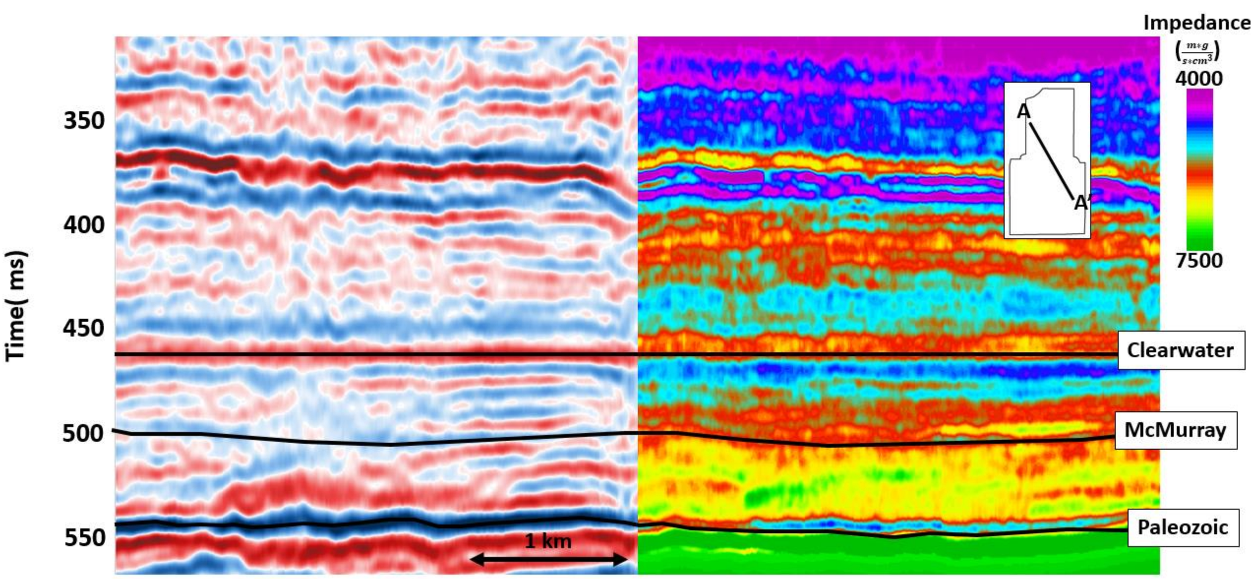

Figure 5-9. Coincident seismic data and P impedance sections, flattened on the Clearwater Formation pick.

5.2 Pre-stack model based PP inversion

Following the analysis of the post-stack PP impedance inversion, pre-stack PP inversion was performed. Utilizing a similar forward modelling and model updating algorithm, pre-stack seismic data was inverted to obtain P impedance, S impedance, density and V_p/V_s. These physical properties were all inverted for simultaneously in the pre-stack inversion process. PP and PS reflectivity can be found as a function of incidence angle using the Zoeppritz equations, or an approximation of the Zoeppritz equations. In this case, the Aki-Richards approximations, a linearized approximation of the Zoeppritz equations, (Aki and Richards, 1980; Haase, 2004) (equations 5-1 and 5-2) were used. In equations 5-1 and 5-2 R_{pp} and R_{ps} are defined as the PP and PS reflection coefficients, α, β and ρ are the average densities across an interface, θ is the average of the incident and transmitted P-wave reflection angle and ϕ is the average of the S-wave reflection and transmission angles.

$$R_{pp}(\theta) \approx \frac{1}{2}\left(1 - 4\frac{\beta^2}{\alpha^2}\sin^2\theta\right)\frac{\Delta\rho}{\rho} + \frac{1}{2}(1+\tan^2\theta)\frac{\Delta\alpha}{\alpha} - 4\frac{\beta^2}{\alpha^2}\sin^2\theta\,\frac{\Delta\beta}{\beta} \qquad (5\text{-}1)$$

$$R_{ps}(\theta,\varphi) \approx -\frac{1}{2}\tan\varphi\left[\left(\frac{\alpha}{\beta} - 2\frac{\beta}{\alpha}\sin^2\theta + 2\cos\theta\cos\varphi\right)\frac{\Delta\rho}{\rho} - 4\left(\frac{\beta}{\alpha}\sin^2\theta - \cos\theta\cos\varphi\right)\frac{\Delta\beta}{\beta}\right] \qquad (5\text{-}2)$$

5.2.1 Pre-stack inversion setup

The input seismic data volumes used in pre-stack inversion were angle gathers. Seismic data are recorded as a function of offset, not angle, so some preprocessing is required to transform data from the offset domain to the angle domain. Pre-stack inversion is very sensitive to noise, therefore in addition to the offset to angle transform, some data preconditioning was applied to the pre-stack seismic data to reduce noise. These data preconditioning steps include: creating supergathers, radon transform denoise, and trim statics.

Seismic super gathers are traces averaged across adjacent CDPs. The pre-stack seismic data signal to noise ratio was greatly increased by generating super gathers. Following super gather creation trim statics were calculated and applied. Trim statics were calculated by cross-correlating each trace of a gather with a pilot trace, the pilot trace was chosen to be the stacked trace at the CDP. Random noise was suppressed using the radon noise suppression. Noise is removed by creating a model for the primary data and estimating random noise from the model, which is then subtracted from the pre-stack gathers. The Radon transform is a process that assumes pre-stack seismic gathers can be made up of many constant amplitude parabolas. The transform was performed in the frequency domain, but each sample can be thought of as a combination of parabolas at each time sample (Hampson-Russell, 2016).

The process of converting seismic data from the offset domain to the angle domain is challenging because the relationship between offset and angle is nonlinear. The method of Bale et al. (2001), based on the non-hyperbolic moveout equation, was used to transform seismic gathers from the offset to the angle domain. A set of example angle gathers is shown in Figure 5-10. The maximum angle with sufficient signal to noise ratio for pre-stack inversion is 25°.

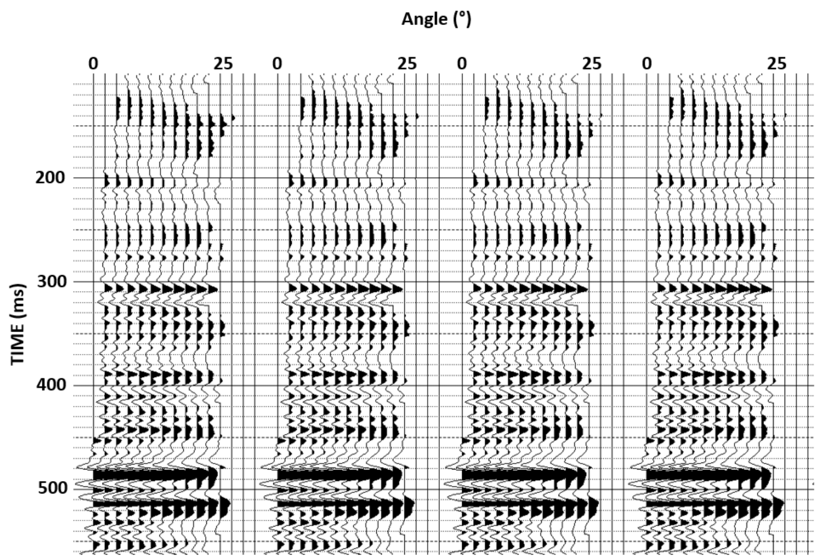

Figure 5-10. Example PP angle gathers. AVO effects are present particularly at 200 ms, 400 ms and 475 ms.

The objective of pre-stack inversion is to recover P and S impedance and density from characteristic wavelets, an input low frequency model and the angle gathers. In order to accurately obtain rock properties from pre-stack seismic data there must be a large enough range of angles and a sufficient change in amplitudes over these angles. The angle gathers in Figure 5-10 display some AVO effects, particularly at 200 ms, 400 ms and 475 ms. In addition to the seismic data used in the pre-stack inversion, either a wavelet or set of wavelets and in input low frequency model are required. Statistical wavelets, extracted in the same manner as from the post-stack seismic data, can be extracted from discrete ranges of angles. 7 different wavelets were extracted at different angles from the angle gathers (Figure 5-11). The wavelets are generally very similar in shape; the side lobe of the larger angle wavelets tend to be slightly lower in amplitude.

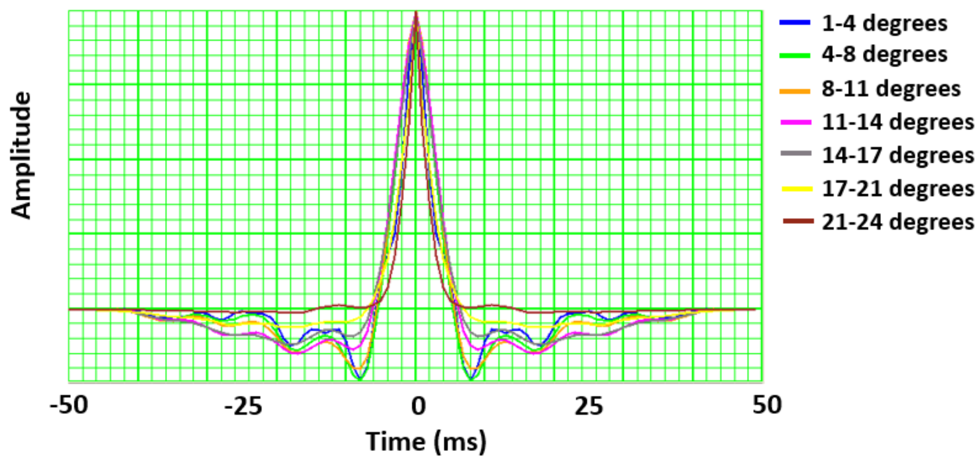

Figure 5-11. Angle dependent wavelets statistically extracted from angle gather seismic data.

The input low frequency model for pre-stack inversion was created in the same way as the post-stack inversion input model. However, in addition to a P impedance low frequency model, shear impedance and density models were created (Figures 5-12, 5-13 and 5-14). The input P impedance model used in the pre-stack inversion is the same as the input model used in the post-stack inversion. This allows for a more direct comparison between the pre-stack and post-stack inversion outputs.

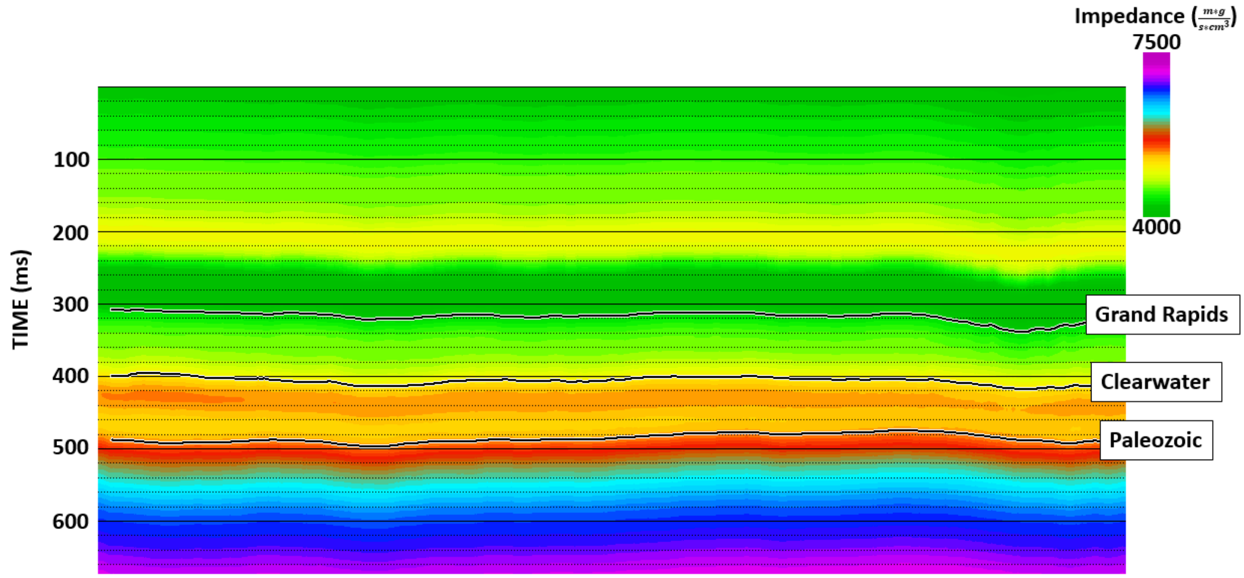

Figure 5-12. Low frequency P impedance model for pre-stack inversion

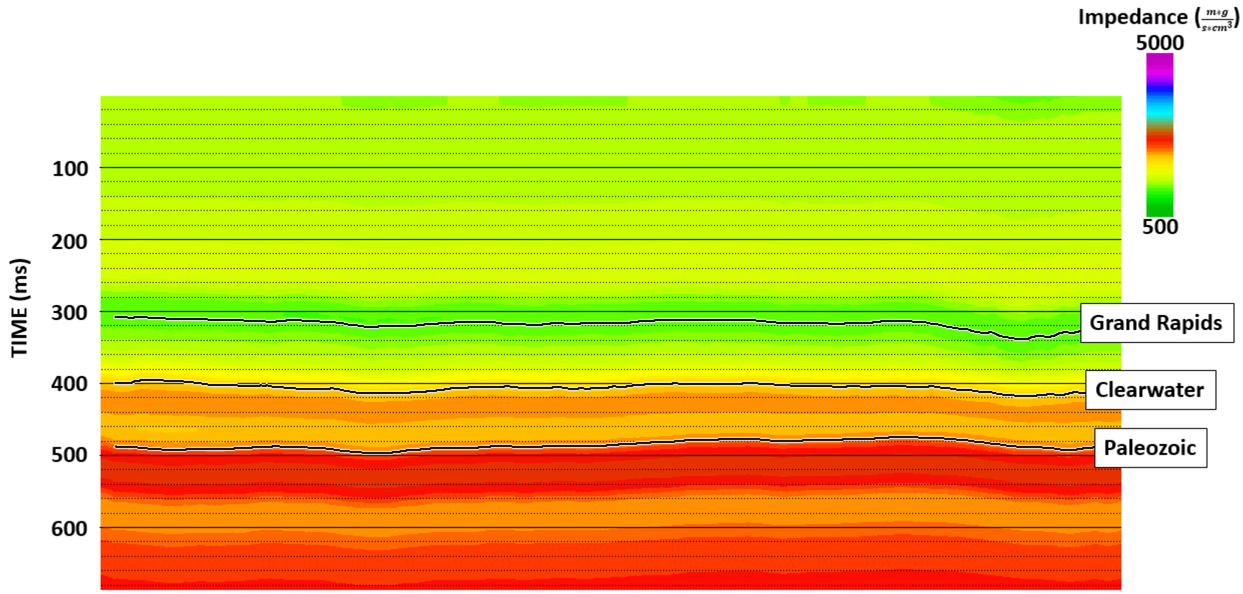

Figure 5-13. Low frequency S impedance model for pre-stack inversion

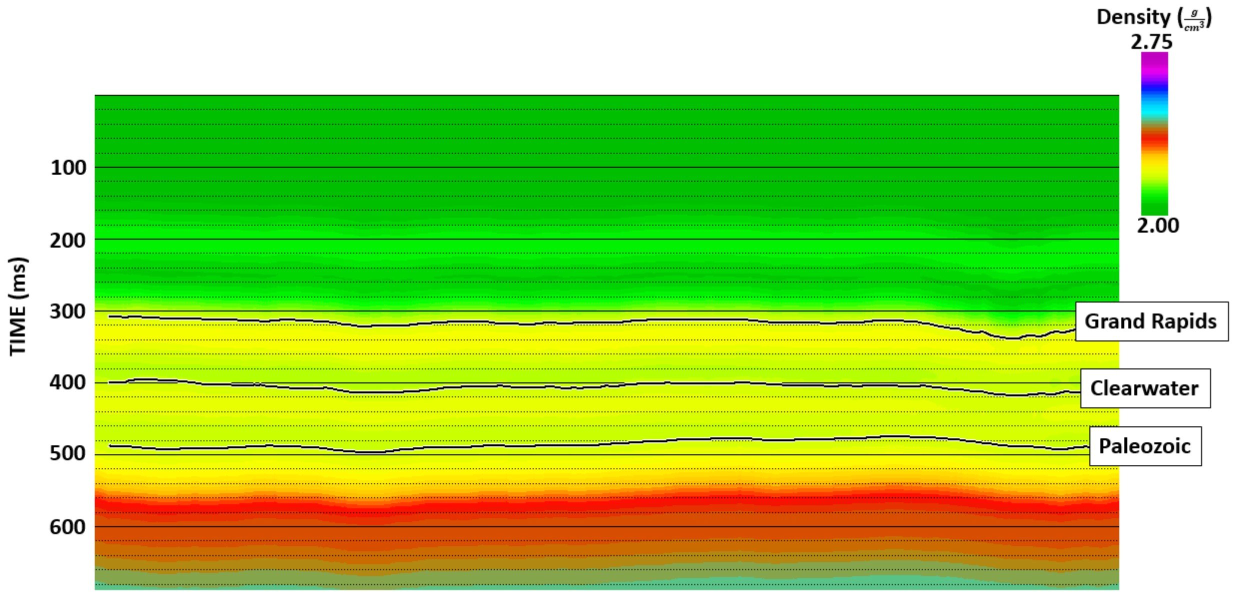

Figure 5-14. Low frequency Density model for pre-stack inversion

Two major assumptions of the pre-stack inversion process are that in wet clastic rocks, there is a linear relationship between the logarithm of P impedance and S impedance; and between P impedance and density (Hampson et al. 2005). These linear relationships were found empirically from well logs (Figure 5-15). The correlation coefficient for the linear regression of the logarithm of P impedance versus the logarithm of S impedance is 0.85, indicating a very strong linearity between the two series. The logarithm of P impedance versus the logarithm of density has a correlation coefficient of the linear regression is 0.65 which implies a moderate linear relationship exists. From these empirical analyses, linearity assumptions were made with relative confidence. In clastic rocks with hydrocarbon saturation these linear relationships do not hold, therefore it is important to calibrate the linear regressions in wet rocks.

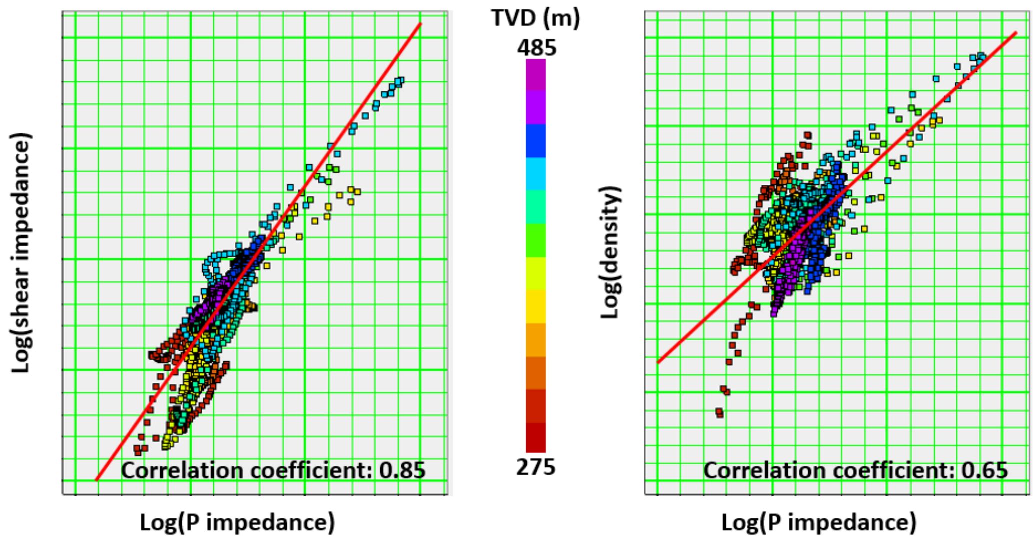

Figure 5-15. The logarithm of P impedance versus the logarithm of S impedance from well logs (left) and the logarithm of P impedance versus the logarithm of density from well logs (right).

The Aki-Richards approximation of the Zoeppritz equations (equations 5-1 and 5-2) show that relatively high incidence angles are required to distinguish between density and P wave velocity. At low angles of incidence, $\theta \sim 0$ and both $\sin^2(\theta)$ and $\tan^2(\theta)$ are ~0. As the incidence angle increases, the ability to distinguish the $\sin^2(\theta)$ and $\tan^2(\theta)$ terms increases. In the Aki-Richards equation, density is proportional to the $\sin^2(\theta)$ term. Therefore in order to accurately invert for density, a large range in offset angles is required. Offset angles in the range of 45° are necessary to invert for density using model updating techniques (Hampson-Russell, 2016). However, pre-stack inversion can still function without updating density models directly. The linear relationships found from well logs (Figure 5-15) can be used to provide a density result.

5.2.2 Pre-stack inversion outputs and analysis

Pre-stack inversion output examples are shown in Figure 5-16, 5-17, 5-18 and 5-19. Quality control tools were the same for both pre-stack and post-stack inversion results. Blind well crossplots for each of the four pre-stack inversion outputs show some variability in their correlation coefficients (Figures 5-20, 5-21, 5-22 and 5-23). The correlation coefficient values range from 0.440 for the density inversion to 0.816 for the V_p/V_S. The results for the P and S impedance have blind well correlation coefficients of 0.690 and 0.745 respectively both indicating strong linear relationships and accurate inversion results for these two parameters. The V_p/V_s blind well test has an even larger correlation coefficient at 0.816, again implying a good inversion result. The V_p/V_s results from inversion are an improvement on the horizon-based V_p/V_s map creation done in Chapter 4, due the inclusion of the low frequency inversion model.

The blind well correlation coefficient for the pre-stack inversion density result is 0.440. In the main interval of interest (Grand Rapids – Paleozoic) the inverted density correlation coefficient is 0.560. The reason for this lower precision in the density inversion is due to the major assumptions made in the pre-stack inversion process. The density results were not inverted iteratively, but the P and shear impedance were. The density results were obtained using an empirical relationship found between the logarithm of the P impedance and the logarithm of the density (Figure 5-15). Even though the correlation coefficient is lower for the density results, the value of 0.56 does indicate the existence of a weak linear relationship and an interpretable pre-stack inversion density result within the main interval of interest.

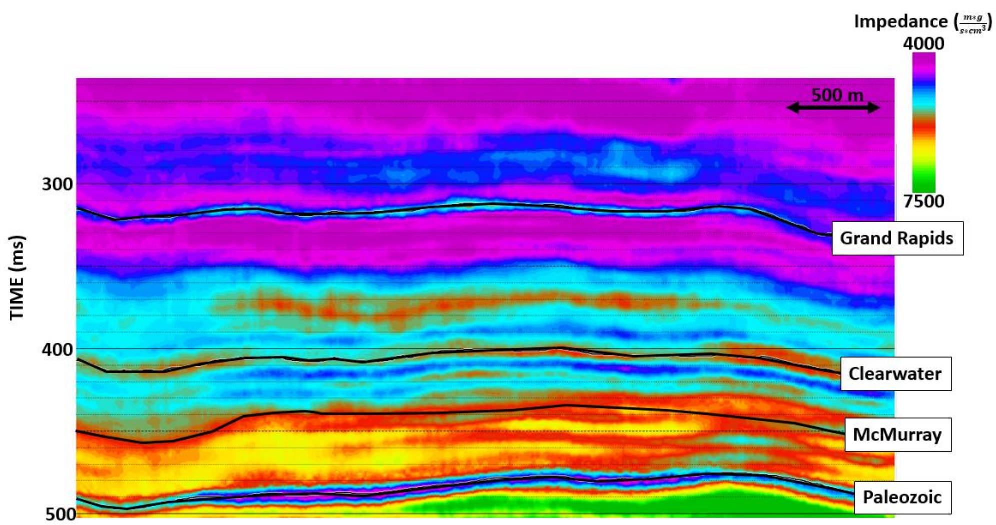

Figure 5-16. Pre-stack inverted P impedance example

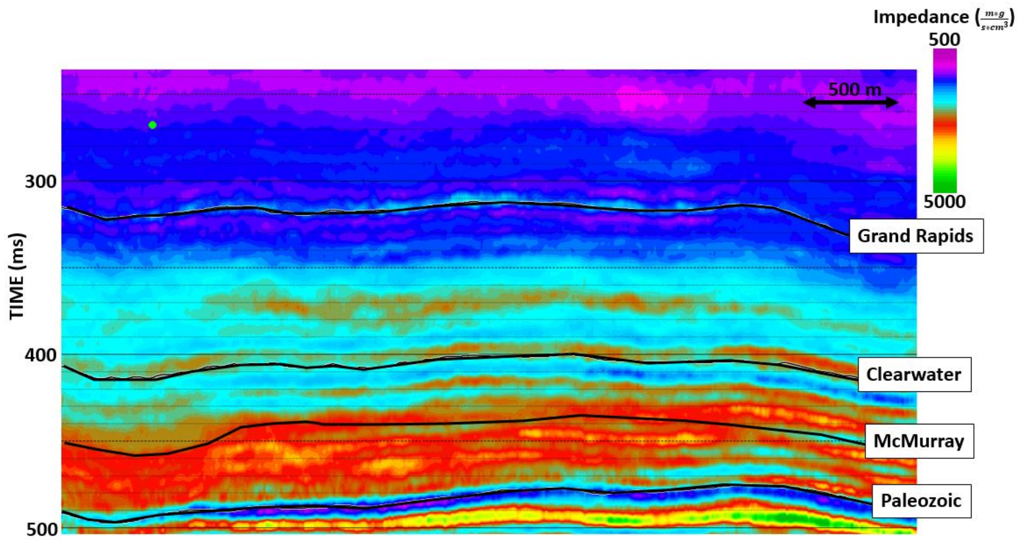

Figure 5-17. Pre-stack inverted S impedance example.

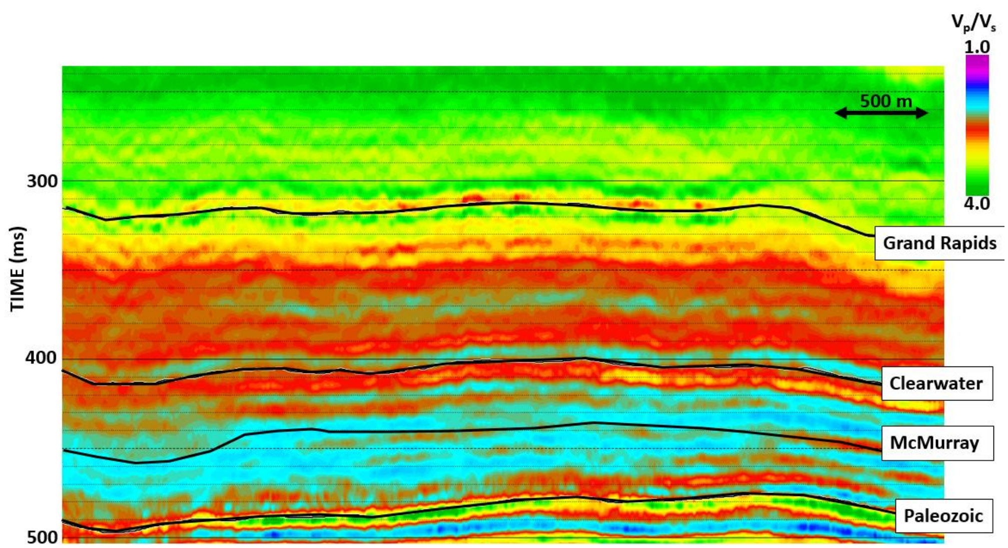

Figure 5-18. V_p/V_s example derived from pre-stack PP inversion.

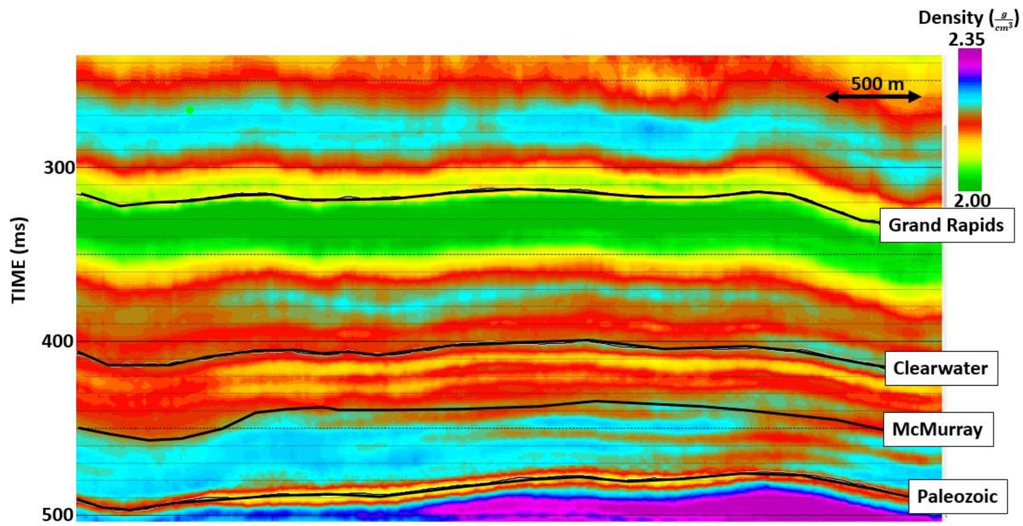

Figure 5-19. Pre-stack inverted density example.

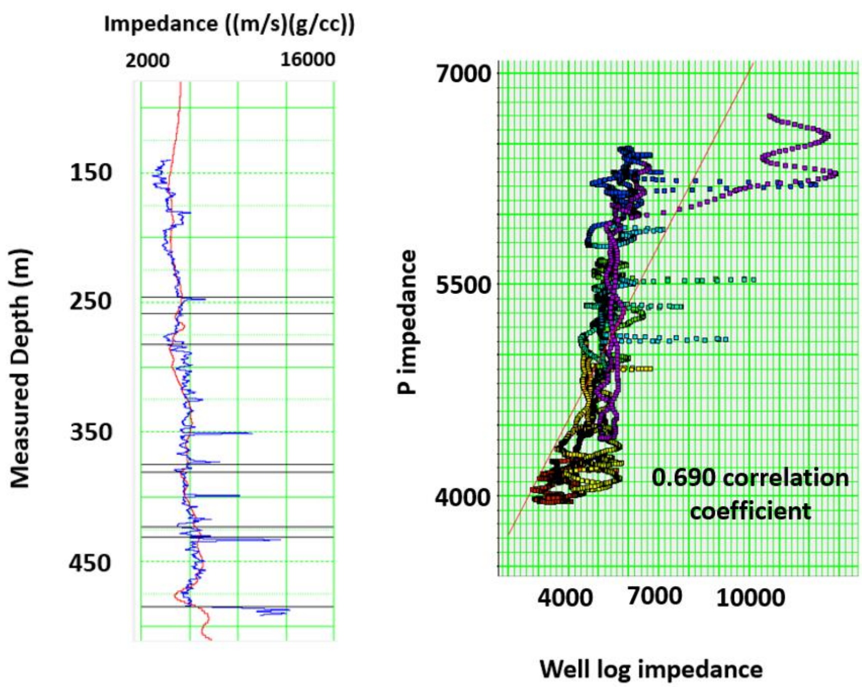

Figure 5-20. Pre-stack inverted P impedance blind well log test. Trace values (left) and crossplot (right). Well log is in blue and inverted trace is in red.

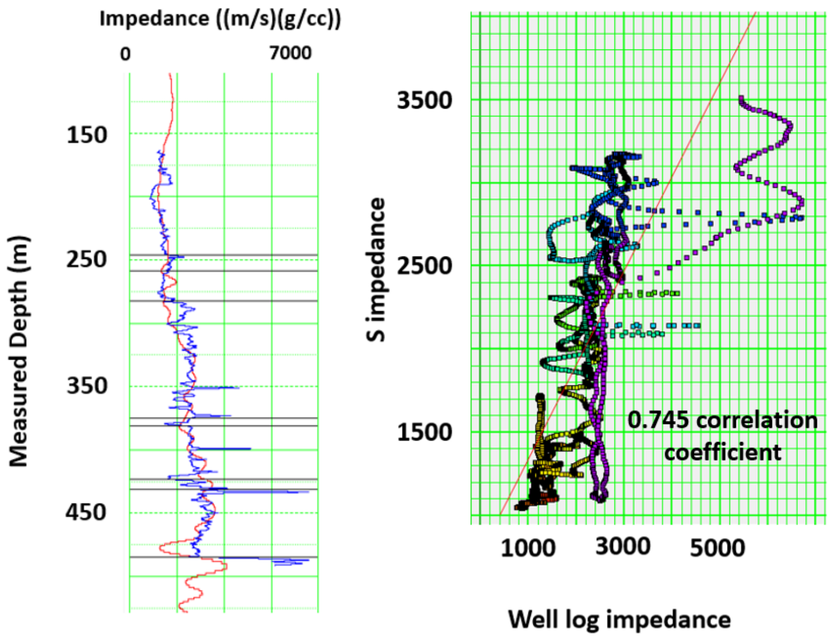

Figure 5-21. Pre-stack inverted S impedance blind well log test. Trace values (left) and crossplot (right). Well log is in blue and inverted trace is in red.

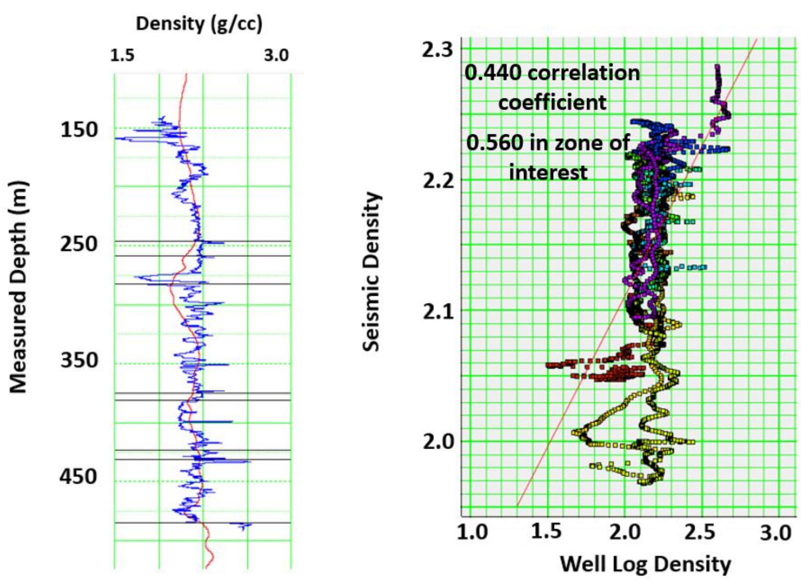

Figure 5-22. Pre-stack inverted density blind well log test. Trace values (left) and crossplot (right). Well log is in blue and inverted trace is in red.

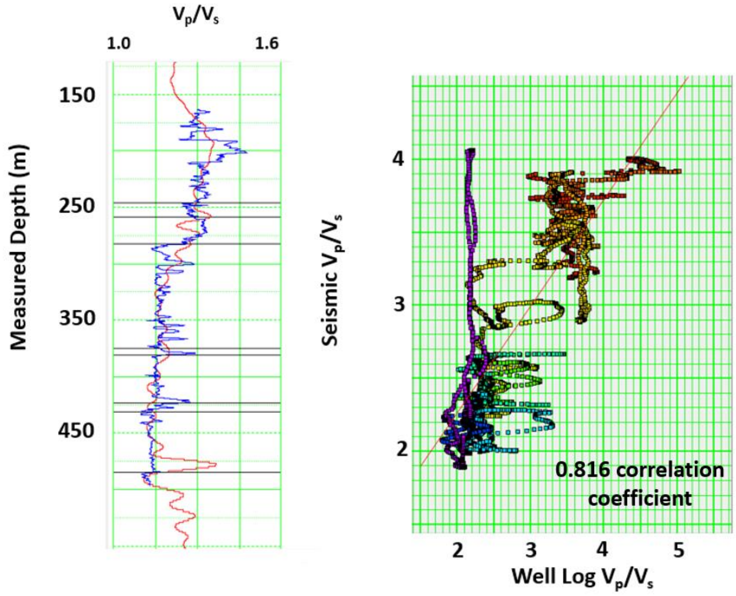

Figure 5-23. Pre-stack inverted V_p/V_s blind well log test. Trace values (left) and crossplot (right). Well log is in blue and inverted trace is in red.

A side-by-side comparison of the post-stack P impedance and pre-stack P impedance in the main interval of interest is shown in Figure 5-24. Within the reservoir (McMurray Fm), the continuity of the strata is clearer on the pre-stack inversion than in the post-stack inversion. These distinct laterally continuous impedance features are the regional McMurray sequence, a system of alternating sands and shales. The higher impedance elements (green) are the regional sands and the lower impedance units are regional shales (yellow/orange). The correlation between impedance and reservoir quality from the post-stack inverted P impedance is also noted for the pre-stack inverted P impedance. A cross section through the McMurray channel feature on the pre-stack inverted P impedance (Figure 5-25) shows more detail than on the post-stack inversion P impedance (Figure 5-9).

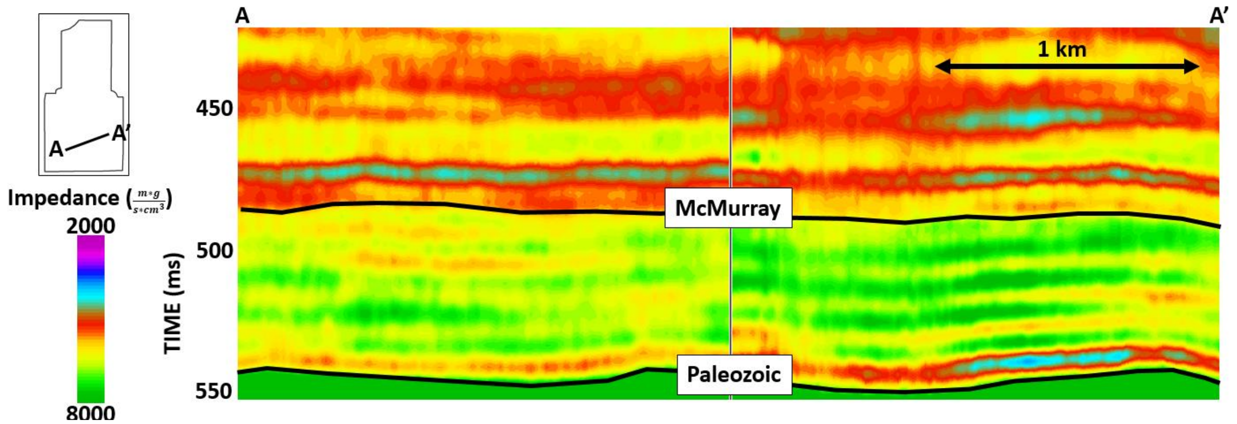

Figure 5-24. Post-stack inverted P impedance (left) and pre-stack inverted P impedance (right).

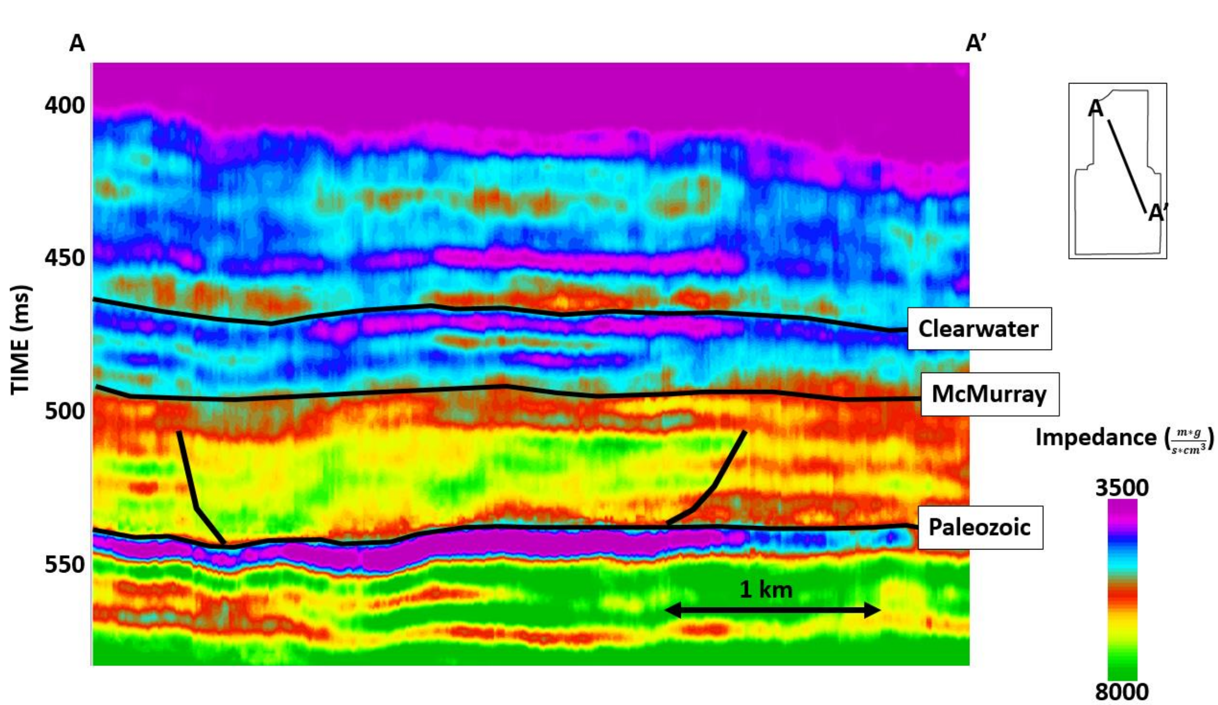

Figure 5-25. Pre-stack inverted P impedance section interpreted to show the large McMurray channel. Channel edges are annotated.

5.3 Post-stack PP-PS joint inversion

Using a similar algorithm to pre-stack and post-stack inversion, both the PP and PS seismic data were inverted simultaneously. Multicomponent joint inversion inputs PP and PS seismic volumes, P-impedance, S-impedance and density models (Figures 5-12, 5-13 and 5-14) and finally PP and PS wavelets and inverts for P-impedance, S-impedance and density. These are equivalent outputs as pre-stack inversion. Margrave et al. (2001) showed that the RMS error in joint inversion results was much less than the RMS error of only PP inversion, when compared with well logs. The input seismic volumes utilized in PP-PS joint inversion must be in the same time domain. In this case, the PS data is registered into the PP domain, as explained in Chapter 4, section 4.3. The methodology of initial model creation is the same for pre-stack inversion as for post-stack PP-PS joint inversion. Therefore, the input models for both pre-stack and joint inversion were the same, which reduces inherent uncertainty when comparing inversion results.

5.3.1 PP-PS joint inversion outputs and analysis

P-impedance, S-impedance, density and V_p/V_s ratio from the joint inversion are shown in Figures 5-26, 5-27, 5-28 and 5-29 respectively. Qualitatively, the PP-PS joint inversion results appear to have a slightly lower signal to noise ratio than the pre-stack inversion results. However, the joint inversion results contain more high frequencies than the pre-stack inversion and therefore yield better vertical resolution. Comparing crossplots of well log to inversion volume, the correlation coefficient for the joint inversion is higher than the pre-stack inversion (Figure 5-30 and 5-31). These crossplots utilize a number of wells from throughout the survey area to best represent the entire inverted volume. The multi-well crossplot for the pre-stack inversion P impedance has a correlation coefficient of 0.560 and the crossplot for the joint PP-PS inversion has a correlation coefficient of 0.671. The joint inversion has a much higher correlation to well control, which indicates a more precise result. The presence of increased high frequency content in the PP-PS joint inversion plays a key role in the increased correlation coefficient.

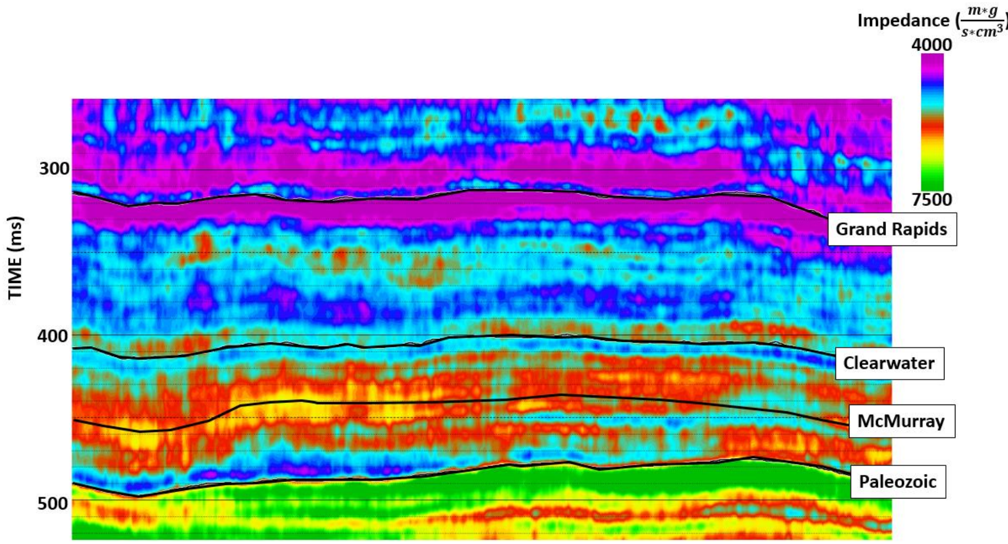

Figure 5-26. Post-stack PP-PS joint inversion P-impedance example.

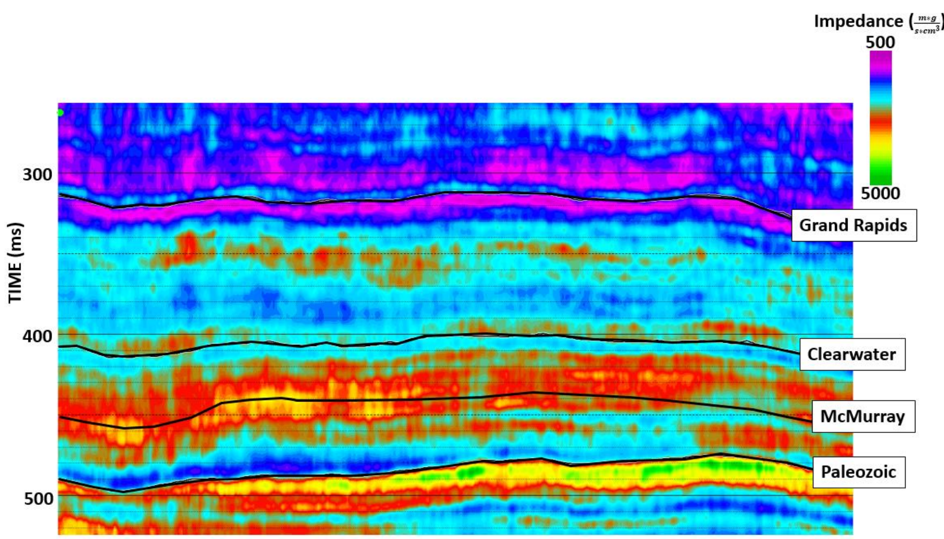

Figure 5-27. Post-stack PP-PS joint inversion S-impedance example.

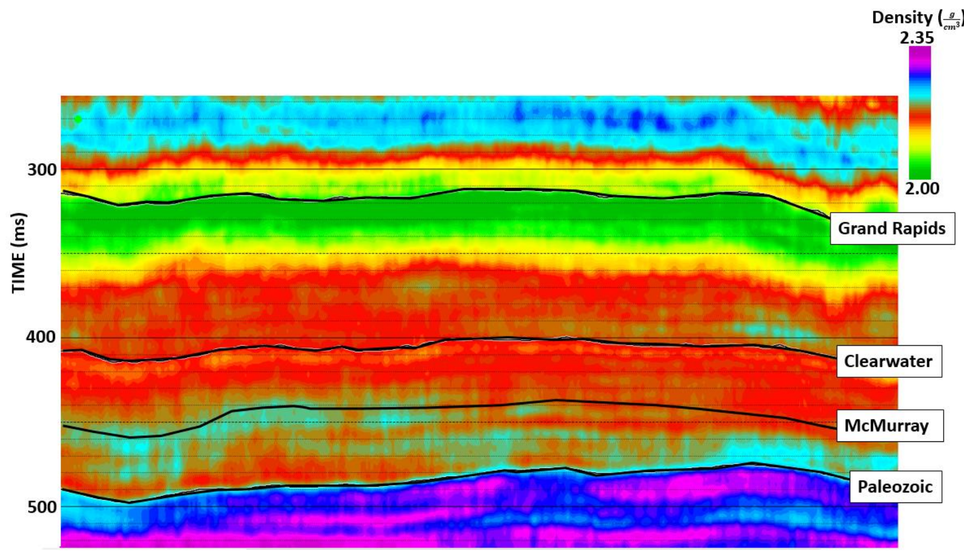

Figure 5-28. Post-stack PP-PS joint inversion density example.

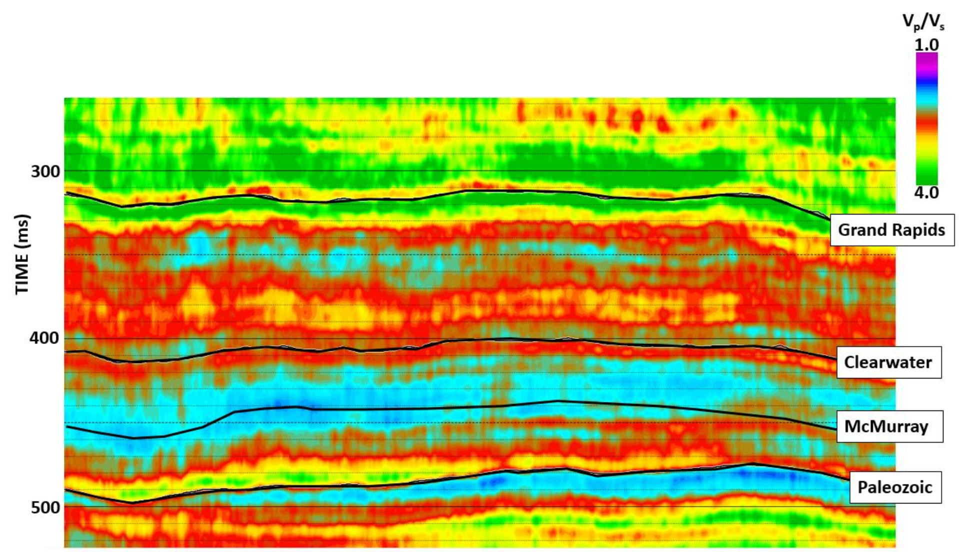

Figure 5-29. V_p/V_s derived from post-stack joint PP-PS inversion.

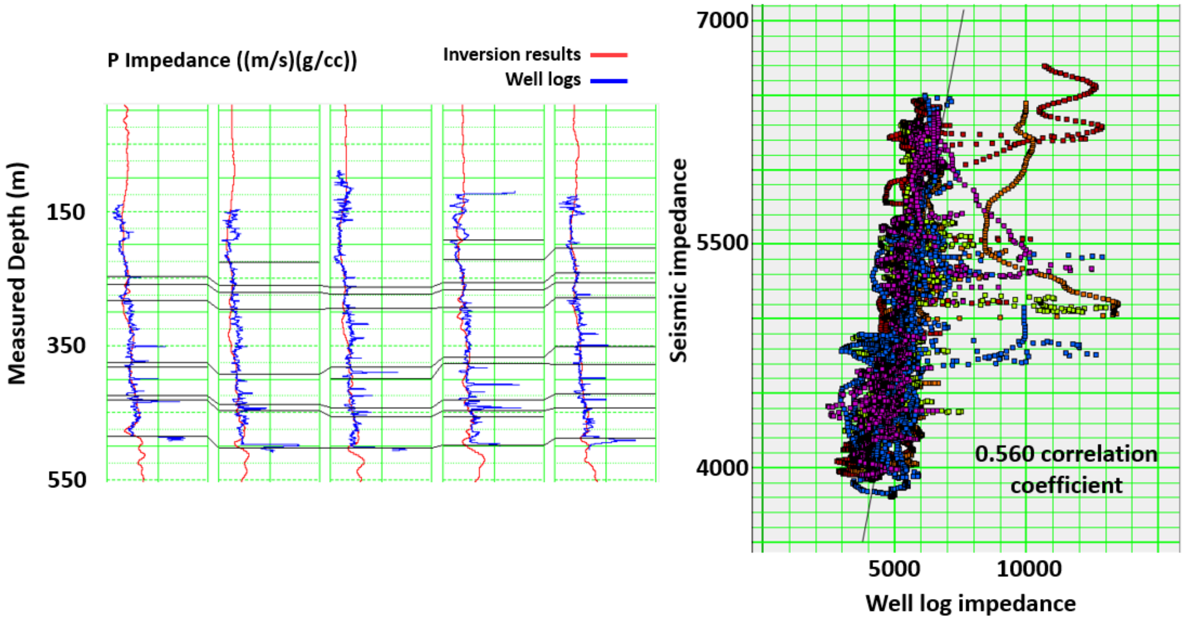

Figure 5-30. Multiple blind well tests for pre-stack P-impedance and crossplot.

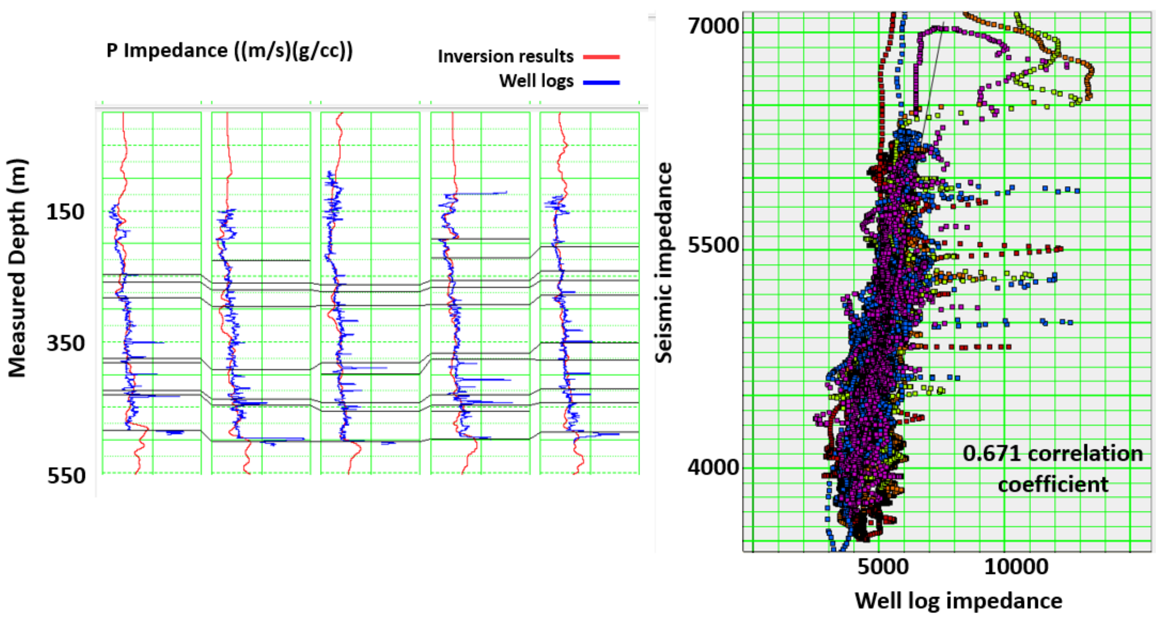

Figure 5-31. Multiple blind well tests for joint inversion P-impedance and crossplot.

5.4 Geomechanical volume generation and analysis

5.4.1 Calculation of geomechanical properties

Poisson's Ratio and Young's Modulus were calculated from the joint inversion outputs (equation 5-3 and equation 5-4). In these equations, ν is defined as Poisson's ratio, E is defined as Young's Modulus, Z_s is S-impedance and ρ refers to density.

$$Poisson's\ Ratio, \nu = \frac{\frac{1}{2}(\frac{V_P}{V_S})^2 - 1}{(\frac{V_P}{V_S})^2 - 1} \tag{5-3}$$

$$Young's\ Modulus, E = \frac{2Z_S^2(1+\nu)}{\rho} \tag{5-4}$$

Because seismically derived geomechanical properties are obtained dynamically, they can be compared with static laboratory measurements to obtain an empirical relationship between static and dynamic measurements (Montmayeur and Graves, 1986). A key application for creating and interpreting geomechanical volumes in the oil sands is formation strength estimation, particularly in the caprock. Anderson et al. (1973), for example, found that fracture pressure (an analogue of strength) can be determined from well log properties. Onyia (1988), found correlations between seismic velocities, porosity, resistivity and rock strength. Another valuable application of geomechanical volumes is to use them as an interpretation tool. A joint interpretation using traditional seismic, well logs, inversion volumes and geomechanical volumes can constrain the analysis much more than using a smaller subset of these data.

5.4.2 Geomechanical property analysis

Example sections for Poisson's Ratio and Young's Modulus are shown in Figure 5-32 and 5-33 respectively. Since the PP-PS joint inversion results have a higher correlation to well logs, the joint inversion outputs were used as inputs to the geomechanical property calculations. Poisson's Ratio, which is defined as the ratio of transverse strain to axial strain, can vary between -1 and 0.5 (Greaves et al. 2011). In most natural materials however, Poisson's Ratio is between 0 and 0.5. Two end member examples of Poisson's ratio are rubber, which has a Poisson's Ratio of 0.5, and cork, which has a Poisson's Ratio of 0.0. In our seismically derived volume, the Poisson Ratio ranges from 0.38 to 0.45, a fairly narrow range. The Poisson Ratio section example (Figure 5-31) has some interesting characteristics. The Colorado Group marine mudstones have a higher

Poisson's Ratio than the Mannville Group sandstones and shales. Since the main focus of our geomechanical study will be on the caprocks, we will observe the properties in the Clearwater Formation and Colorado Group predominantly.

Young's Modulus is defined as the ratio of stress applied to the observed strain in a material (IUPAC, 1997) and is a measure of the stiffness of a material. The Young's Modulus (Figure 5-32) in our volume ranges from 1 GPa to 15 GPa. Other materials with similar moduli include: rubber, which has a Young's Modulus of 0.01 GPa and human bone which has a Young's Modulus of 14 GPa (Engineering Toolbox, 2012 and Rho, 1993). Values of Young's Modulus in Figure 5-32 shows that marine shales (caprocks) have a lower stiffness than the sand dominated sediments.

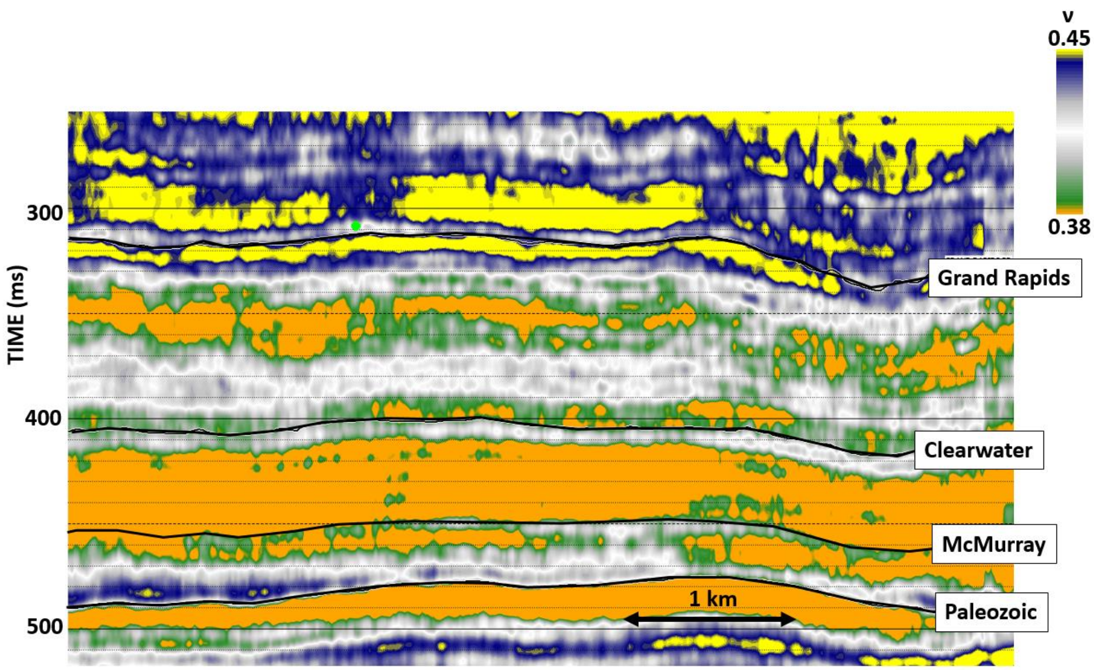

Figure 5-32. Poisson's Ratio section example.

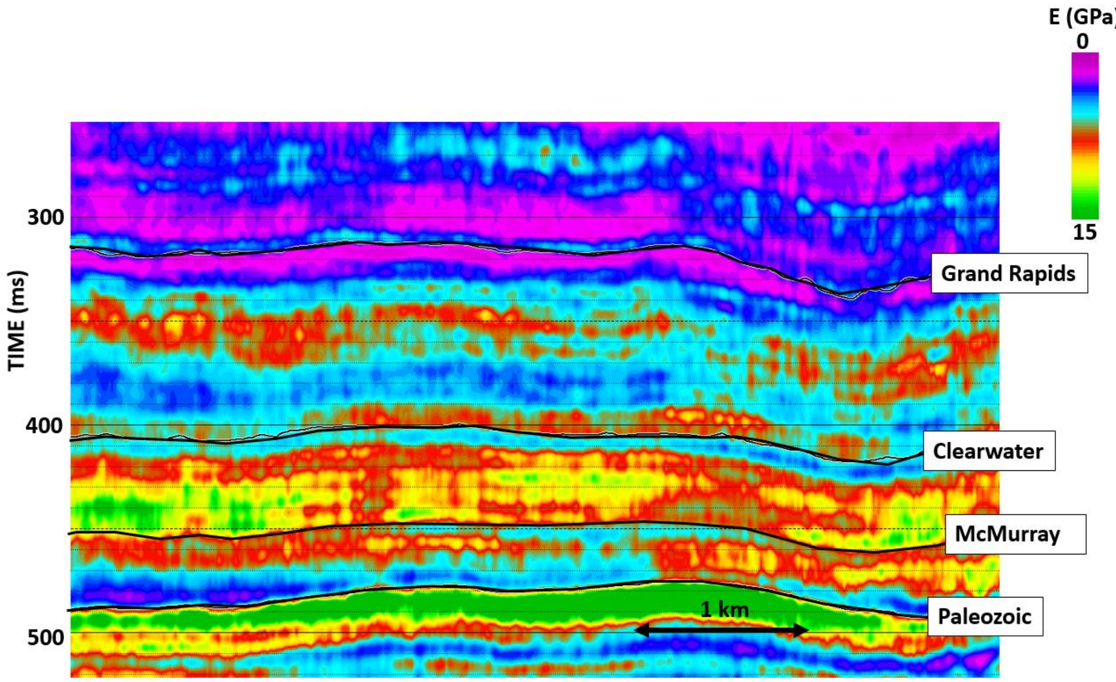

Figure 5-33. Young's Modulus section example.

5.4.3 Clearwater Formation geomechanical analysis

To understand the regional variability of the Clearwater Fm properties, interval average maps for the geomechanical properties were generated. The Young's Modulus of the Lower Clearwater is fairly variable in the project area (Figure 5-34), ranging from 6 to 14 GPa. Interval RMS Poisson's Ratio, has a nearly identical character to Young's Modulus (Figure 5-34), implying that Poisson's Ratio and Young's Modulus are inversely linearly related in the Lower Clearwater Fm. Unfortunately this means that the two maps cannot be interpreted as independent datasets.

In order to understand if there is a correlation between Young's Modulus, Poisson's ratio and any well log attribute two relatively close well logs with different geomechanical values were selected (Figure 5-35 and 5-36). The log character for both wells is very similar. The Lower Clearwater Formation is a marine shale with lower porosity than the surrounding sandstones. The well logs do not appear to relate any specific lithological property with the geomechanical volumes. The best method to properly evaluate and empirically compare the seismically derived geomechanical volumes to the geology would be to undertake static and dynamic core analyses.

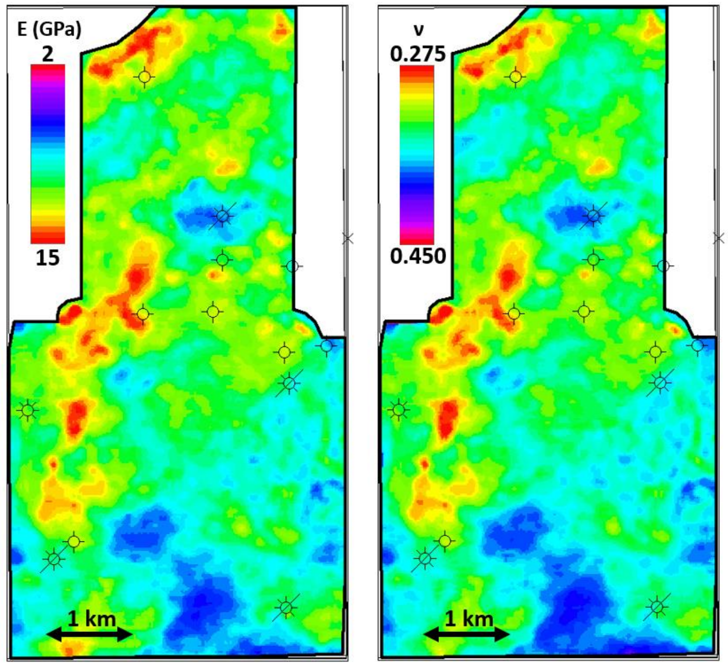

Figure 5-34. Lower Clearwater interval average Young's Modulus (left) and Poisson Ratio (right).

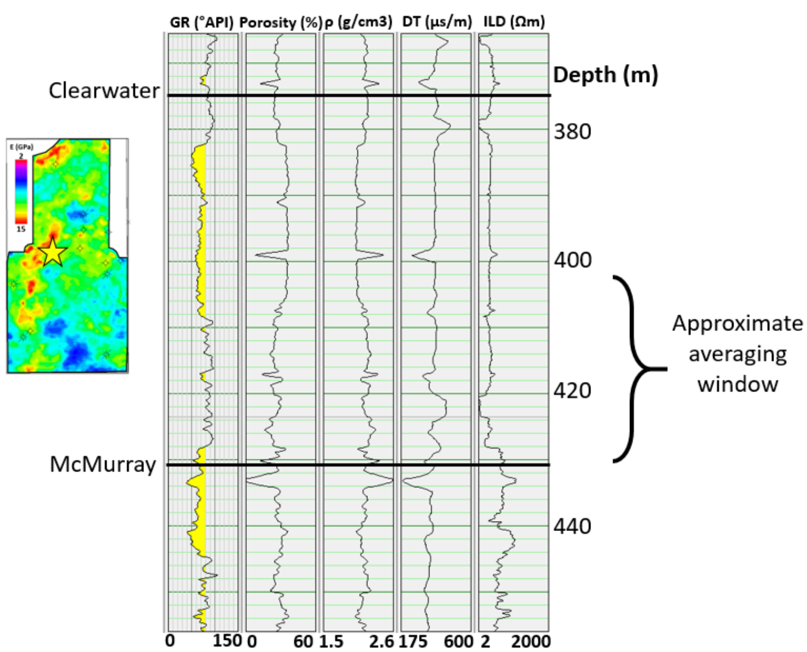

Figure 5-35. Well log from a region with relatively high Young's Modulus and low Poisson's Ratio.

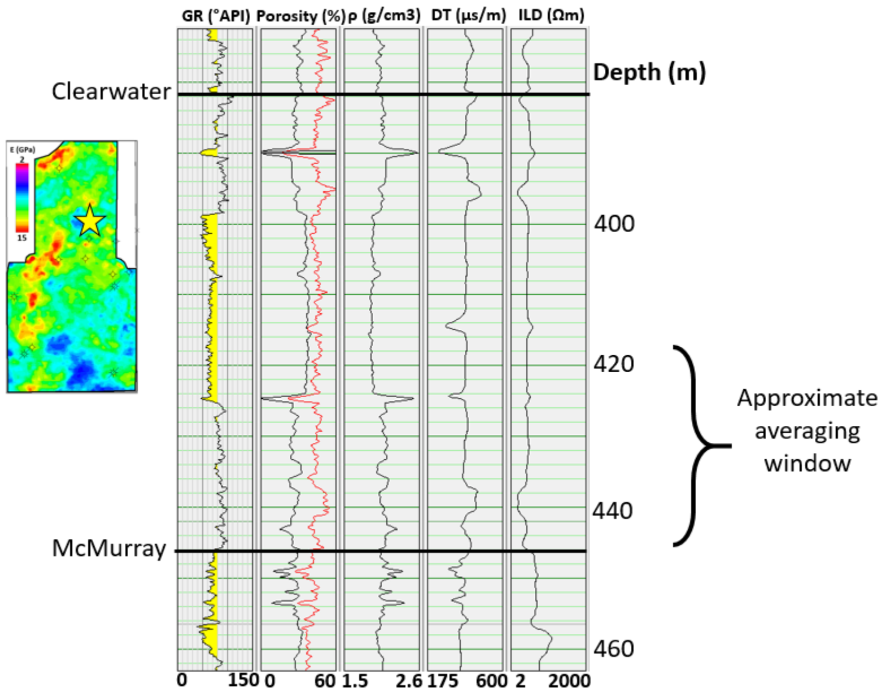

Figure 5-35. Well log from a region with relatively low Young's Modulus and high Poisson's ratio. The red porosity log is neutron porosity and the black porosity log is density porosity.

5.5 Linear and nonlinear multiattribute analysis

All or a subset of the inversion outputs and their permutations were used together in order to obtain any given well log attribute through multi-attribute analysis and neural networks. Relationships between well log data and seismic data were found at well locations, and these relationships were used to predict a given property throughout the entire seismic volume. Hampson et al. (2001) were able to accurately predict well log properties using least-squares minimization, and two types of neural networks: multilayer feedforward network and the probabilistic neural network. Rops and Lines (2015) made viscosity predictions using multiattribute analysis of well logs from the Athabasca Oil Sands.

5.5.1 Linear multiattribute analysis

The most basic multiattribute transform that was used to predict well logs properties was least-squares minimization. A target log value was written as a linear combination of several attribute values. Figure 5-36 shows a graphical representation of the target log expression. A relevant property to predict using several seismic volumes is the gamma ray log. In the Athabasca region, the gamma ray log is the primary lithological indicator. Figure 5-37 shows the different attributes that were used to predict gamma ray logs at each seismic bin location. Predicted gamma ray logs were based on prestack inversion outputs: P and S-impedance, density and V_p/V_s. While there exists no explicit expression for gamma ray value as a function of seismic parameters, there may be an implicit relationship. Crossplotting gamma ray well logs with seismic parameter well logs will show if there is any such empirical relationship.

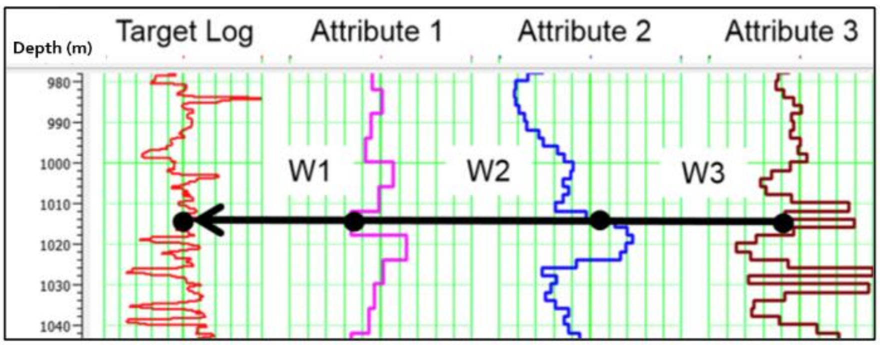

Figure 5-36. Graphical representation of multiattribute analysis. The target log value can be written as a linear combination of log values for other attribute. W1, W2 and W3 are scalar multipliers. (Hampson-Russell, 2013).

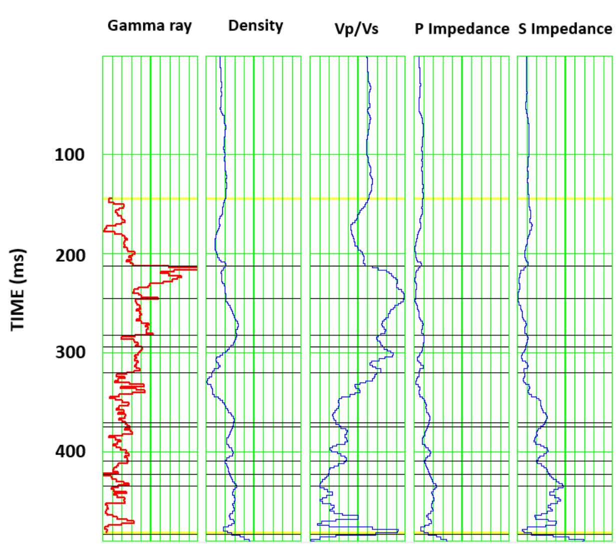

Figure 5-37. Gamma ray log and several seismic properties. A linear combination of the blue curves will be used to predict the red curve.

5.5.1.1 Least-squares minimization training

For a first-pass test of multiattribute analysis, 3 well logs were used to train the data. The all-well error and the validation error decreases as each seismic attribute is added (Figure 5-38). The attributes are added such that the most effective gamma ray predictor comes first and the least effective gamma ray predictor comes last. In this case, V_p/V_s is the most effective gamma ray predictor followed by S-impedance, P-impedance and density. The all-well error is the RMS prediction error calculated using all of the wells. The validation error is the RMS prediction error, calculated by leaving out an individual well to test it blindly. The validation error is a better tool to estimate which attributes to use in the prediction. All four attributes decrease validation error, so in predicting gamma ray logs all attributes were used. In cases where many attributes are used, it is possible to over-fit the training data. In these cases, attributes must be left out in order to find the lowest validation error. The least-squares minimization technique finds that the gamma ray value of well logs was predicted by the square of P impedance, S-impedance, density and V_p/V_s. The validation error (Figure 5-38) tells us that the prediction has an RMS error of 23.75 °API when using the 4 seismic derived attributes.

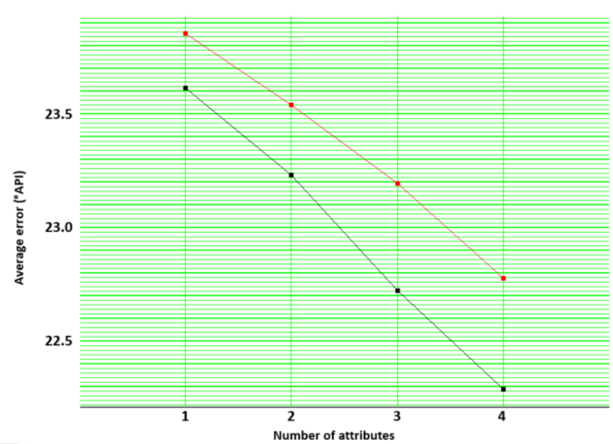

Figure 5-38. All well error (black) and validation error (red) for predicting gamma ray response. Prestack inversion outputs and 3 wells used for training.

5.5.1.2 Least-squares minimization analysis

Figure 5-39 displays the true gamma ray log and the predicted gamma ray log for the three wells used in the analysis. The gamma ray log prediction is not effective in the Colorado and Grand

Rapids intervals (200-350 ms) (Figure 5-39). However, within the reservoir interval (450-500 ms) the prediction is fairly good, predicting gamma ray trends fairly accurately. A top to bottom well crossplot (Figure 5-40) has a correlation coefficient of 0.52. This correlation coefficient value does not indicate a great correlation, but does imply the existence of a linear relationship. Figure 5-41 shows an example section through the gamma ray volume. Qualitatively, blind wells show relatively good correlation between the gamma ray well logs and seismically derived gamma ray, especially at a long wavelengths and within the McMurray Fm (Figure 5-42).

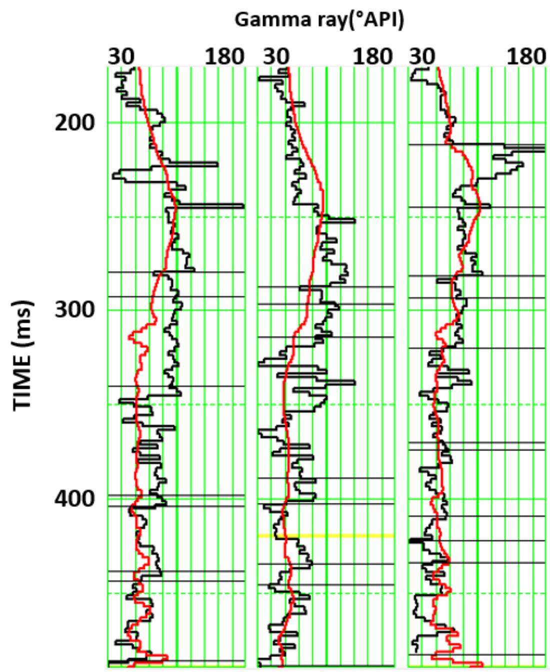

Figure 5-39. Predicted (red) and true (black) gamma ray logs for multiattribute analysis.

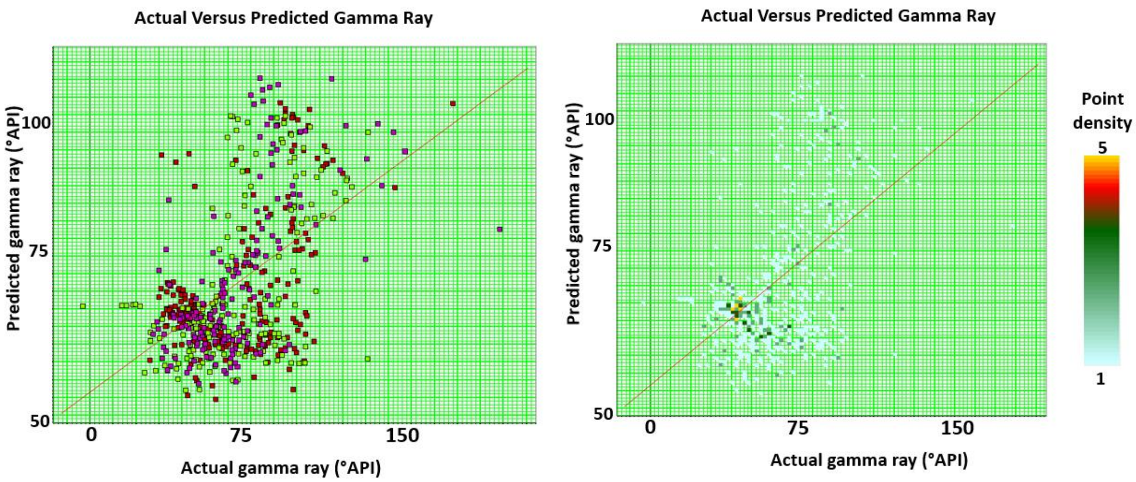

Figure 5-40. Actual versus predicted gamma ray log crossplot and crossplot density chart for multiattribute analysis. Crossplot contains entire logged interval, correlation coefficient is 0.52.

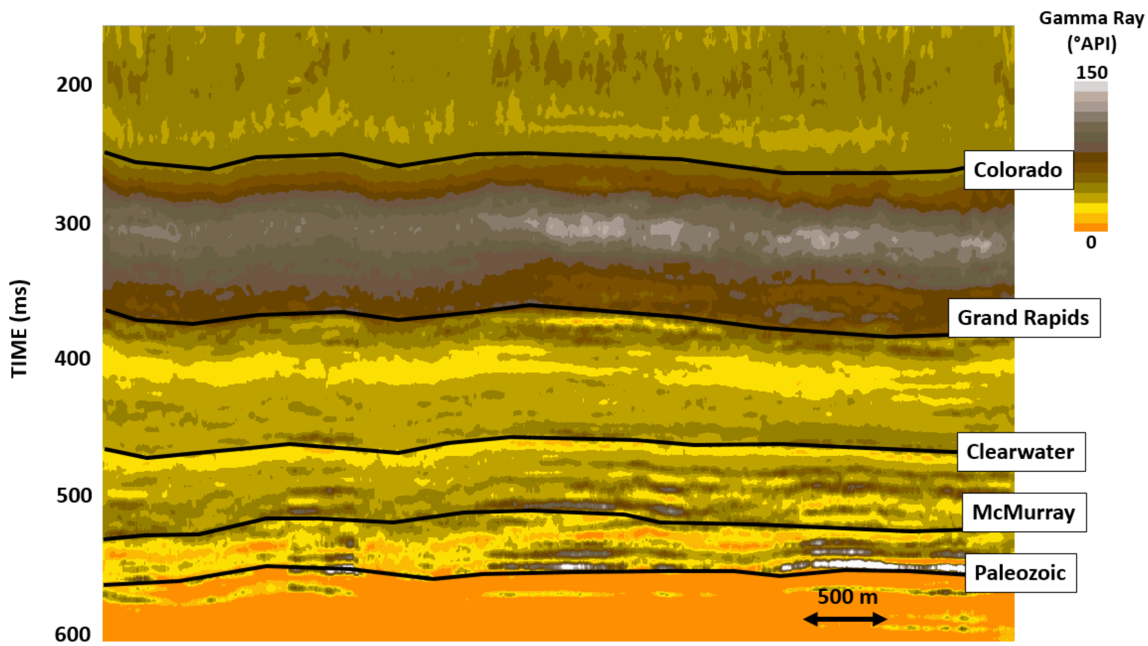

Figure 5-41. Cross section through gamma ray volume created with multiattribute analysis

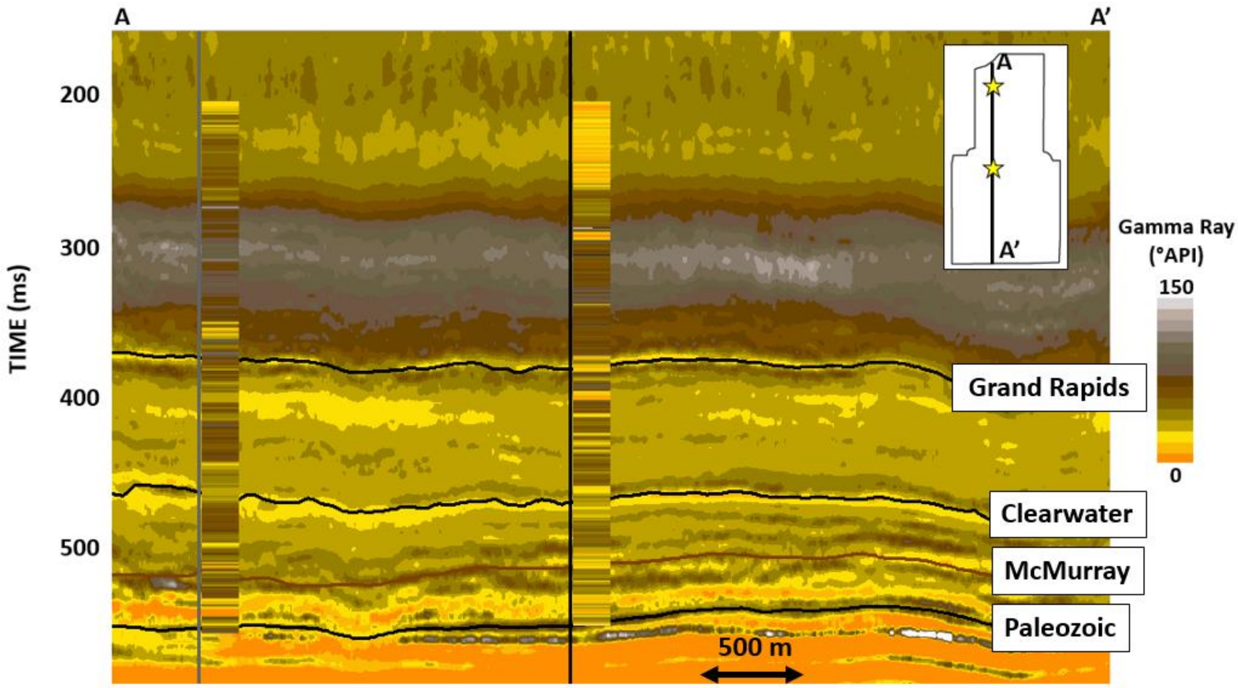

Figure 5-42. Blind well logs superposed onto gamma ray volume.

5.5.2 Nonlinear multiattribute analysis

A neural network is a nonlinear parallel processing algorithm, solving problems in a similar way to how a brain performs. A neural network has multiple layers of input and output parameters (Figure 5-43). Each neural unit is connected to a number of inputs and outputs, these inputs and outputs are weighted to determine the value of the neuron. Neural networks can learn in supervised and unsupervised ways. In supervised learning, a set of outputs are known and the neural network determines the relationship between the inputs and outputs. In unsupervised learning, the outputs are not provided. Supervised learning methods are typically used in applying neural networks to seismic parameters. The type of neural network used in this study is the probabilistic neural network (PNN).

A Neural Network

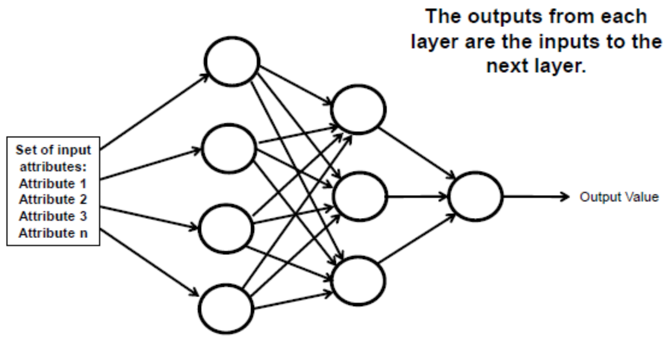

Figure 5-43. A schematic of a basic neural network (Hampson-Russell, 2013). Each circle is a "neuron."

An accurate volume of gamma ray values was generated in a study by Herrera et al. (2006) using the probabilistic neural network. The probabilistic neural network can be used in both mapping and classification. In mapping, the PNN directly predicts a well log value whereas in classification the PNN places an output into a certain category. When predicting gamma ray values, the classification problem defines several ranges of gamma ray values, each of these ranges being a category. The neural network will attempt to predict the appropriate category for each seismic sample. The probabilistic neural network uses a mathematical interpolation technique to predict a well log property.

5.5.2.1 Neural network prediction

The same three well logs, and the same four seismically derived attributes used in the least-squares prediction, were used to calculate gamma ray value for the PNN. Figure 5-44 shows the predicted and true gamma ray logs for the PNN. The predicted and actual logs qualitatively match very well. A crossplot can give a more quantitative measure of the success of the prediction (Figure 5-45). The correlation coefficient of the crossplot for the PNN is 0.90 which implies a very close prediction. A blind well crossplot (Figure 5-46), has a cross correlation of 0.67, indicating a strong linear relationship. Overall the non-linear prediction tool does a much better job at predicting gamma ray values from seismic data than the least-squares linear prediction method.

An example cross section through the neural network gamma ray volume is shown in Figure 5-47. Interpretation of the gamma ray volume is fairly trivial, as in the Cretaceous clastic rocks of the Athabasca Oil Sands, porous sands usually have low gamma ray and shaly zones have higher gamma ray values. Figure 5-48 shows an interval average gamma ray map for the Upper McMurray Formation. Porous reservoir sands would be expected in the low gamma ray anomalies. The main low gamma ray anomalies are in the vicinity of the McMurray B2 aged channel, as expected.

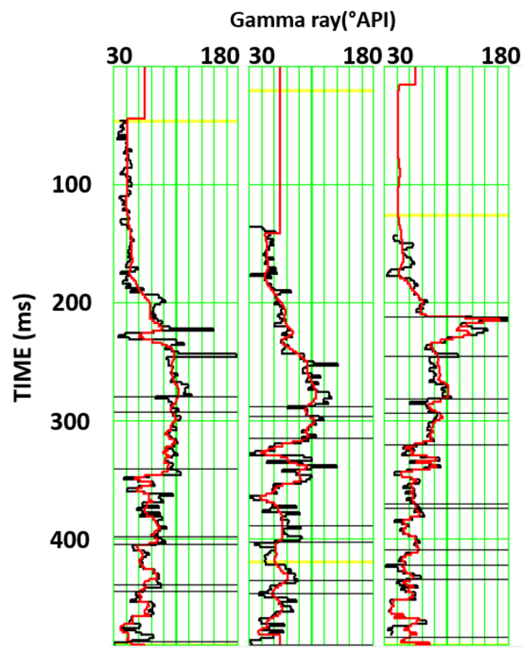

Figure 5-44. Predicted (red) and true (black) gamma ray logs for probabilistic neural network.

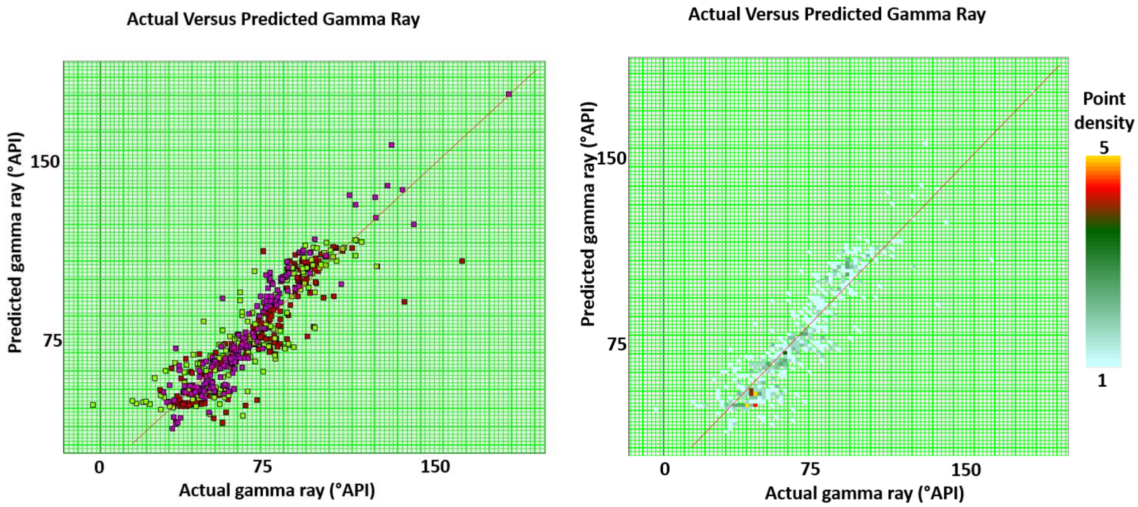

Figure 5-45. Actual versus predicted gamma ray log crossplot and crossplot density chart for probabilistic neural network. Crossplot contains entire logged interval, correlation coefficient is 0.90.

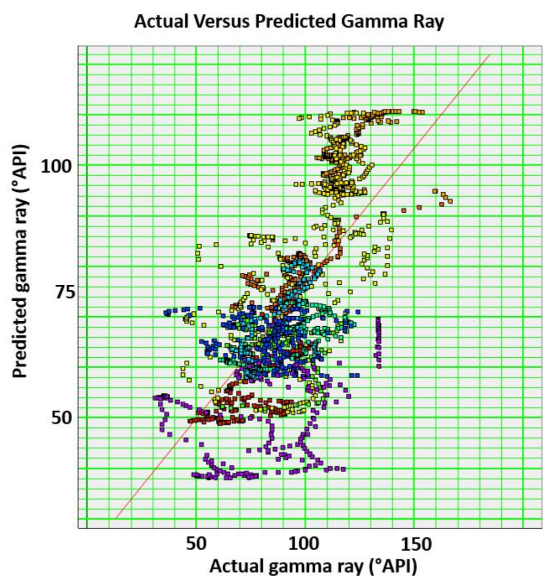

Figure 5-46. Blind well crossplot for PNN gamma ray prediction, cross correlation is 0.67.

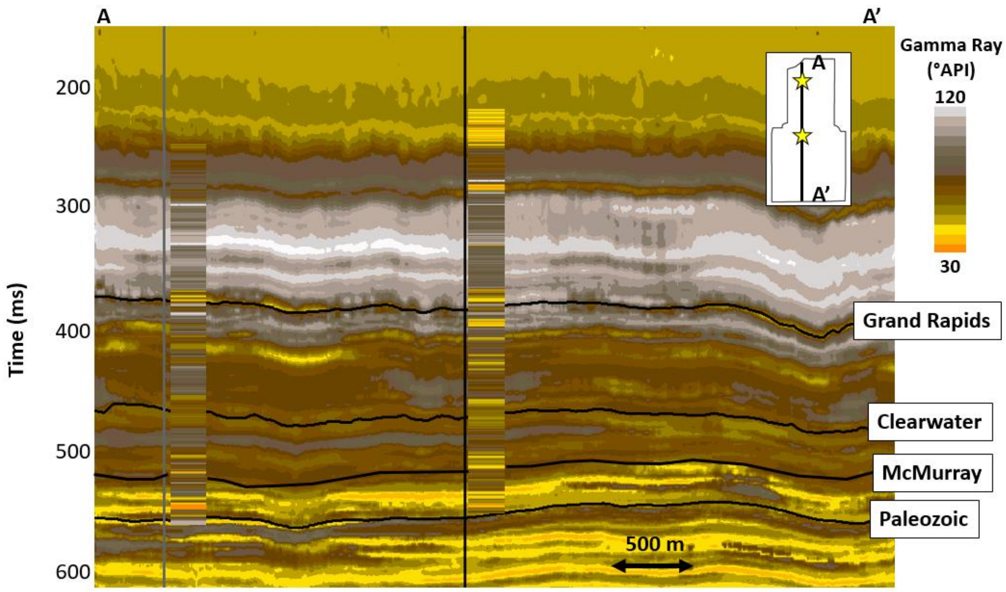

Figure 5-47. Cross section through gamma ray volume output obtained by probabilistic neural network.

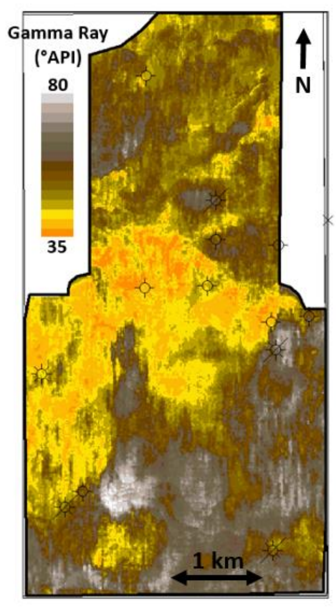

Figure 5-48. Interval average gamma ray map for Upper McMurray Fm.

5.5.2.2 Neural network classification

The probabilistic neural network can work as a prediction tool or a classification tool. Directly predicting a well logs property using a neural network was done to predict a gamma ray value. Rather than directly predicting the gamma ray log value, the probability of a certain class of gamma ray value can be predicted. A class can be defined as a range of well log values. Gamma ray well log values were split into 5 different ranges: 0-40 °API, 40-80 °API, 80-120 °API, 120-160 °API and 160-200 °API. Each of these 5 ranges of values is a class, the 40-80 °API class represents clean reservoir sands and the 80-120 °API and 120-160 °API classes represent non-reservoir facies. The classification PNN is similar to a discriminant analysis problem (Hampson-Russell, 2013).

The probabilistic neural network provides a volume of data for each gamma ray category, where each sample is the probability of that sample being in the category. For example, Figure 5-49 shows a cross section through the 40-80 °API data volume. This image depicts the likelihood that the gamma ray value is between 40-80 °API, or class 2. This range of gamma ray values more or less falls into the lithological category of reservoir facies. In Figure 5-49, the McMurray Fm, ~450 ms to ~500 ms, is comprised of predominantly 40-80 °API sediments, however there are some obvious anomalies with very low probability of being reservoir facies. Most notably, in the center-left of the image, there are 3 zones with nearly 0% probability of being reservoir facies. To study these features more in depth, the other PNN classification volumes can be viewed. Figures 5-50 and 5-51 show the probability of samples being between 80-120 °API and 120-160 °API respectively. Clearly there is much more 80-120 °API content in the Lower Cretaceous strata than 120-160 °API content.

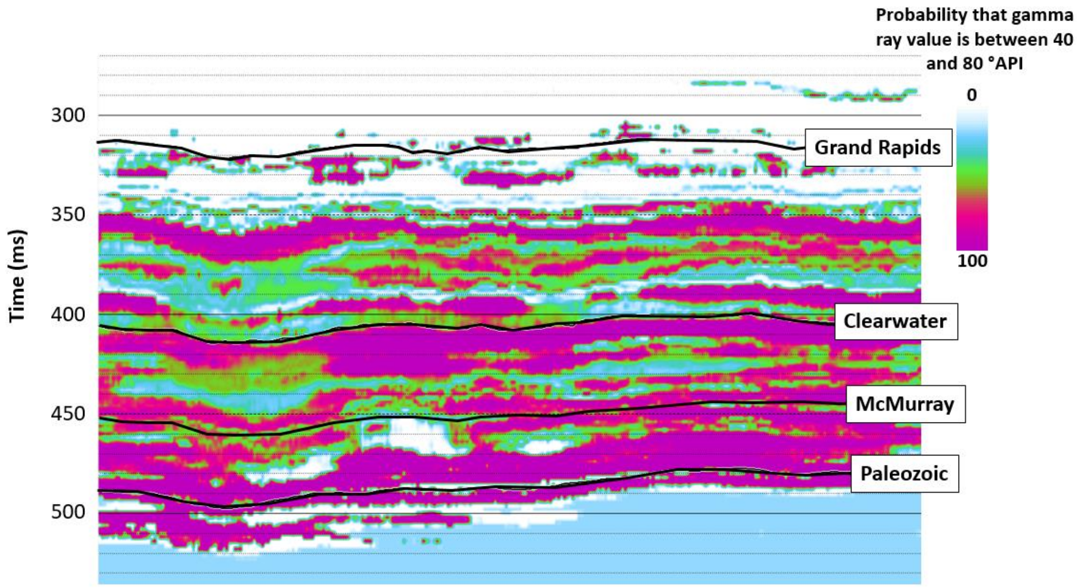

Figure 5-49. Probability cross section from PNN classification process. Colour is the likelihood that a sample falls between 40 and 80 °API.

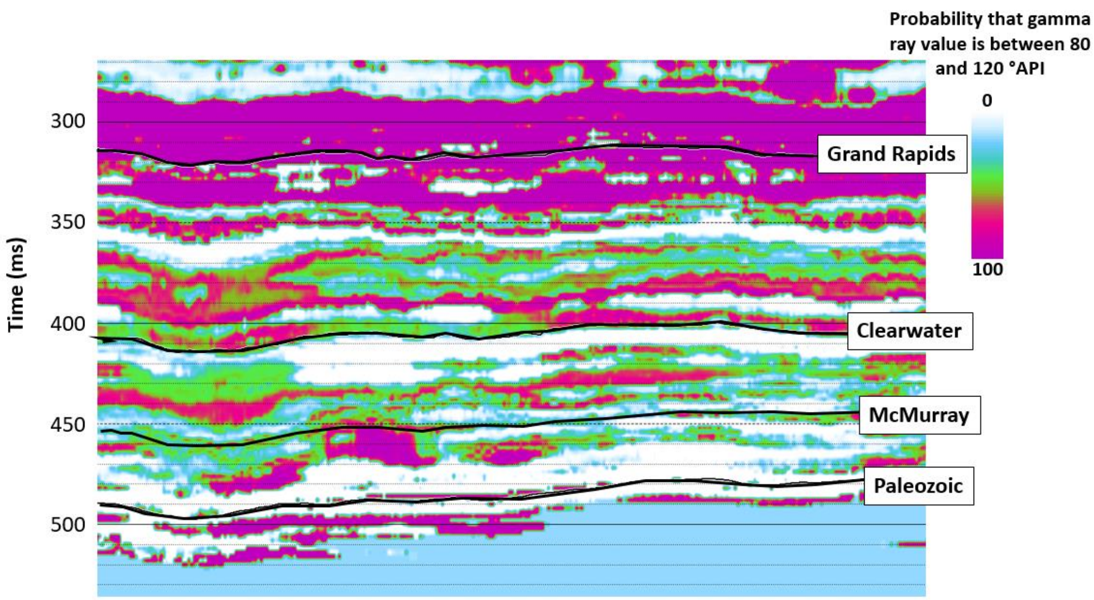

Figure 5-50. Probability cross section from PNN classification process. Colour is the likelihood that a sample falls between 80 and 120 °API.

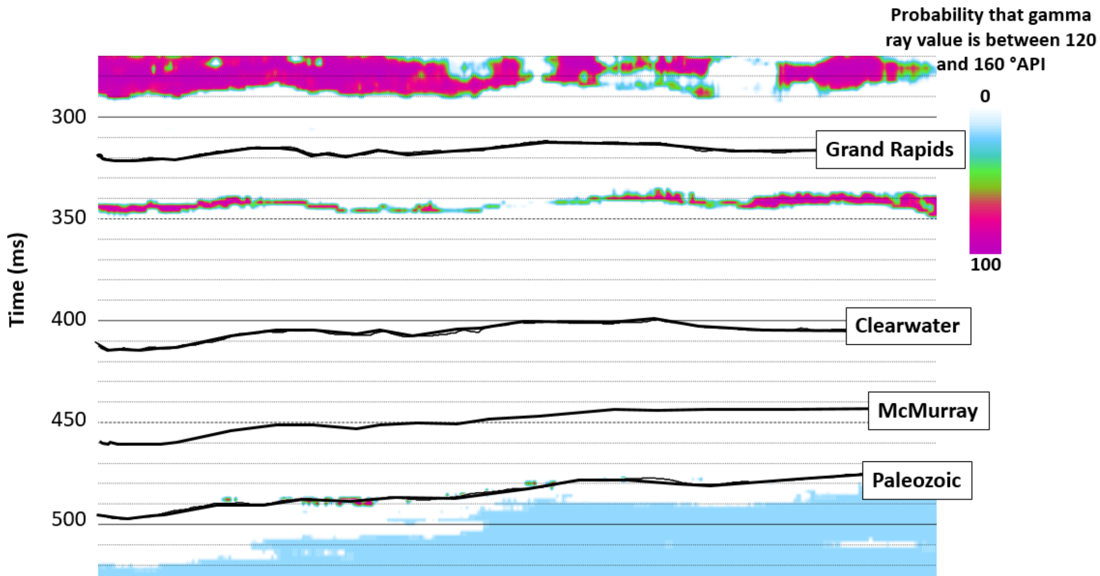

Figure 5-51. Probability cross section from PNN classification process. Colour is the likelihood that a sample falls between 120 and 160 °API.

There is significant class 4 (120-160 °API) content in the Colorado Group, which makes sense from the known geology, the Colorado group is a marine shale and should contain more passive radioactivity than the coarser grained material. The non-reservoir facies anomaly identified on Figure 5-49 is mirrored on Figure 5-50. There is a high probability of these anomalies existing as class 3 (80-120 °API) sediments according to Figure 5-50.

In addition to a volume produced for each class, the PNN classification process created a most likely class and probability of a most likely class volume. The value of the most likely class is shown in Figure 5-52 and the probability of the most likely class is shown in Figure 5-53. The certainty of the most likely class (Figure 5-53) is very high, with the exception of zones below the Paleozoic Unconformity. There is no well control deeper than this level which likely accounts for the uncertainty of the PNN in this part of the section. The discrete class values in Figure 5-52 are as expected, with shale facies (class 3, 4) predominantly present in the Colorado group and reservoir facies (class 2) concentrated in the Grand Rapids and McMurray Formations. It is important to quality control the PNN classification process and compare to the well log data. A crossplot between the PNN most likely class values and a blind well log show a correlation coefficient of 0.595 (Figure 5-54). Considering the discrete nature of the PNN classification process, this is a strong relationship implying a good neural network output.

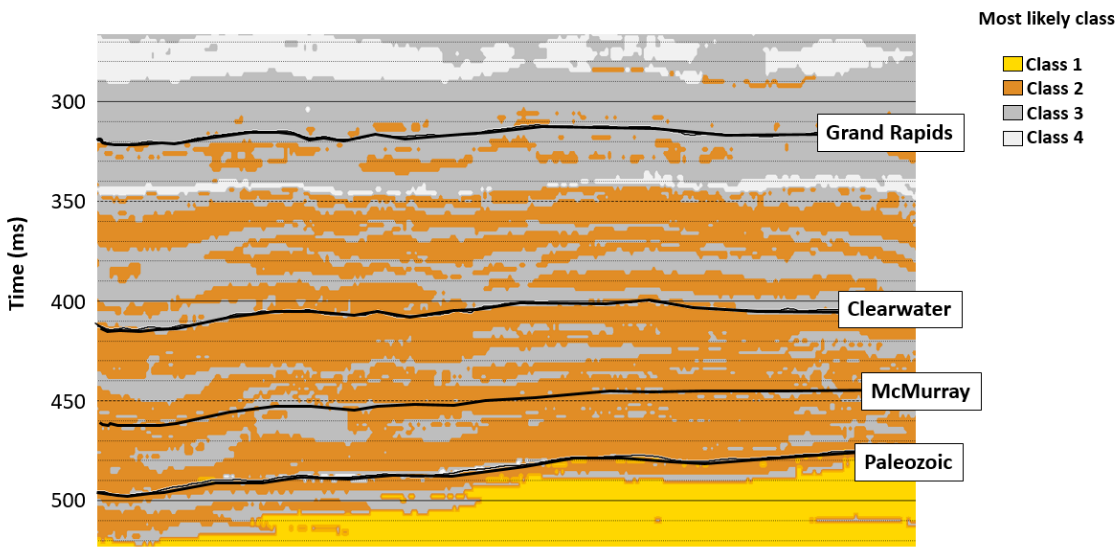

Figure 5-52. The most likely gamma ray class from PNN.

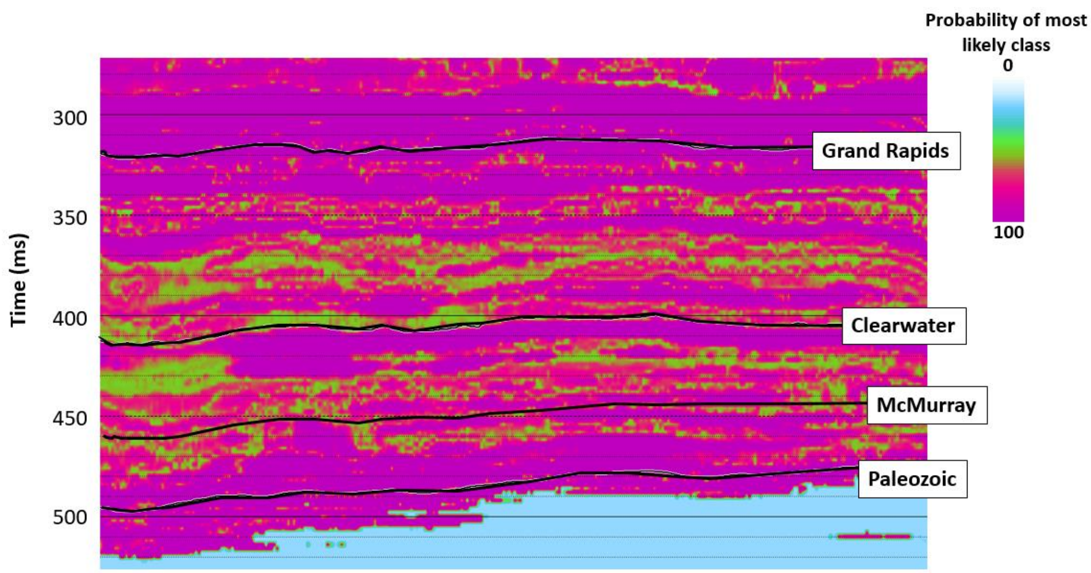

Figure 5-53. The probability of the most likely class from PNN.

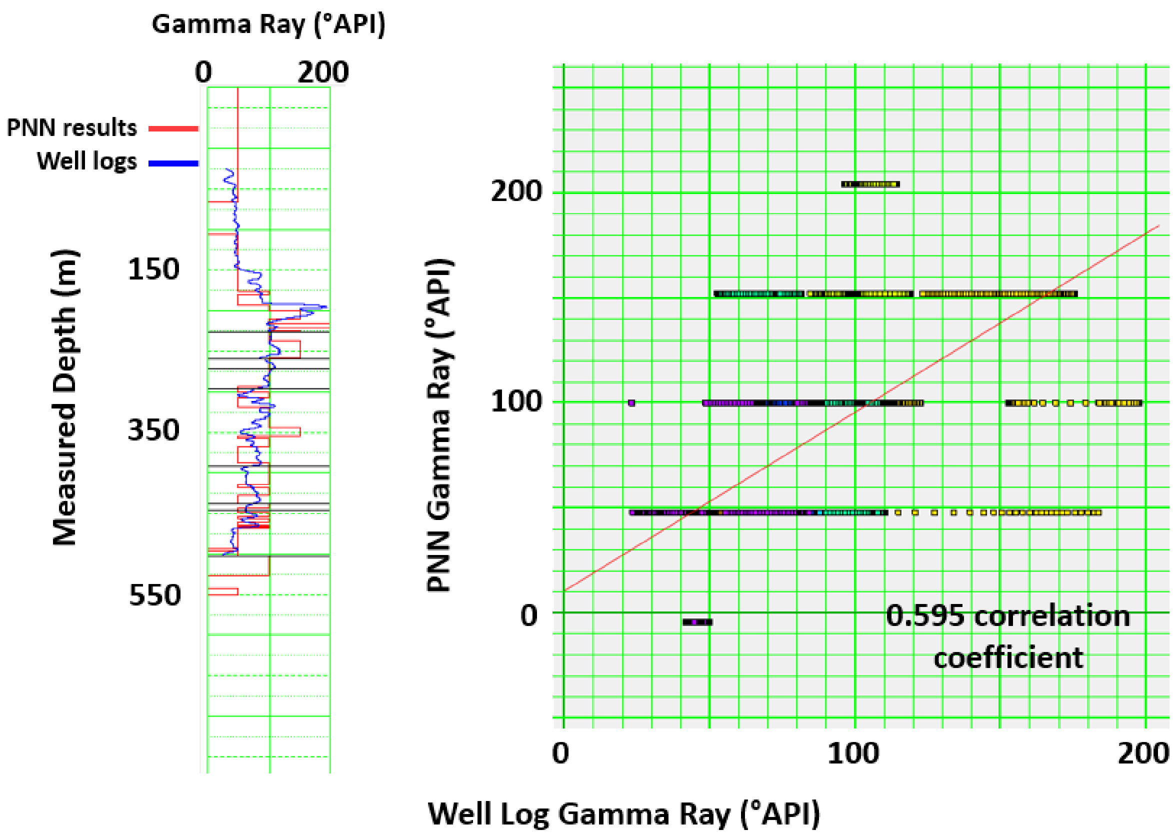

Figure 5-54. Blind well crossplot between PNN most likely class and well log gamma ray values.

5.5.2.3 Interpretation of neural network volumes

An interval RMS map through the entire McMurray Formation to Paleozoic Unconformity window shows that the vast majority of the McMurray Formation is made up of class 2 sediments (Figure 5-55). A more confined window, encompassing the Upper McMurray and the class 3 probability in the same window is shown in Figure 5-56. The zones with low class 2 probability have high class 3 probability. The interpretation here is that the low class 2 probability (high class 3 probability) zones contain more mudstone content than the surrounding sediments. A cross section with a superposed gamma ray well log further confirms the interpretation that class 2 PNN samples represent reservoirs sands and class 3 PNN samples represent mudstones (Figures 5-57 and 5-58 respectively). Particularly within the reservoir interval (McMurray Fm to Paleozoic) the high gamma ray zones correlate to high class 3 certainty and the low gamma ray zones correlate to high class 2 certainty.

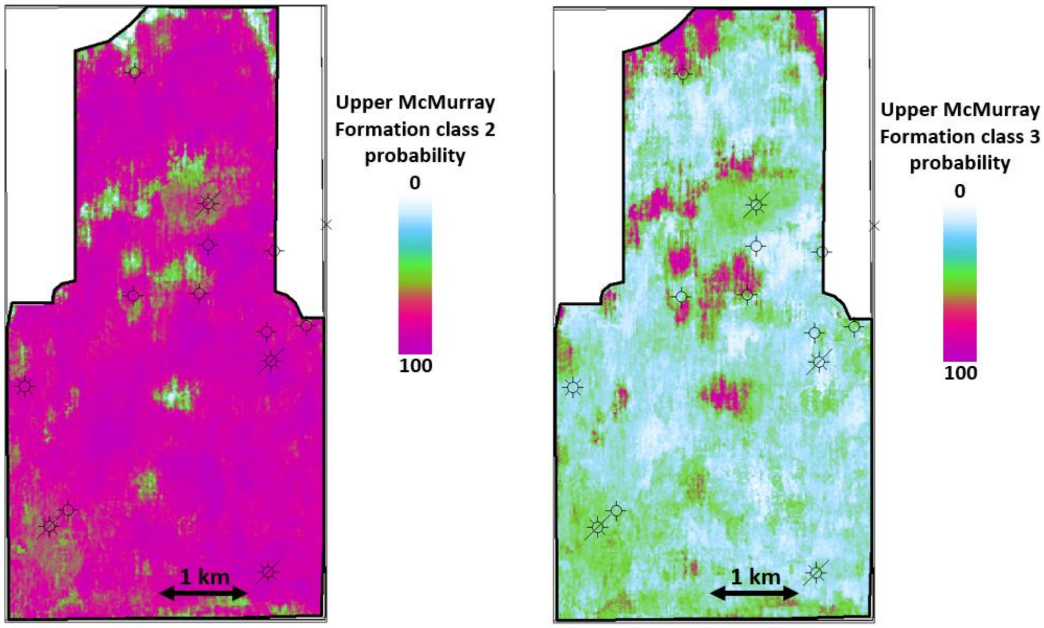

Figure 5-56. Upper McMurray class 2 (left) and class 3 (right) probability from probabilistic neural network classification process.

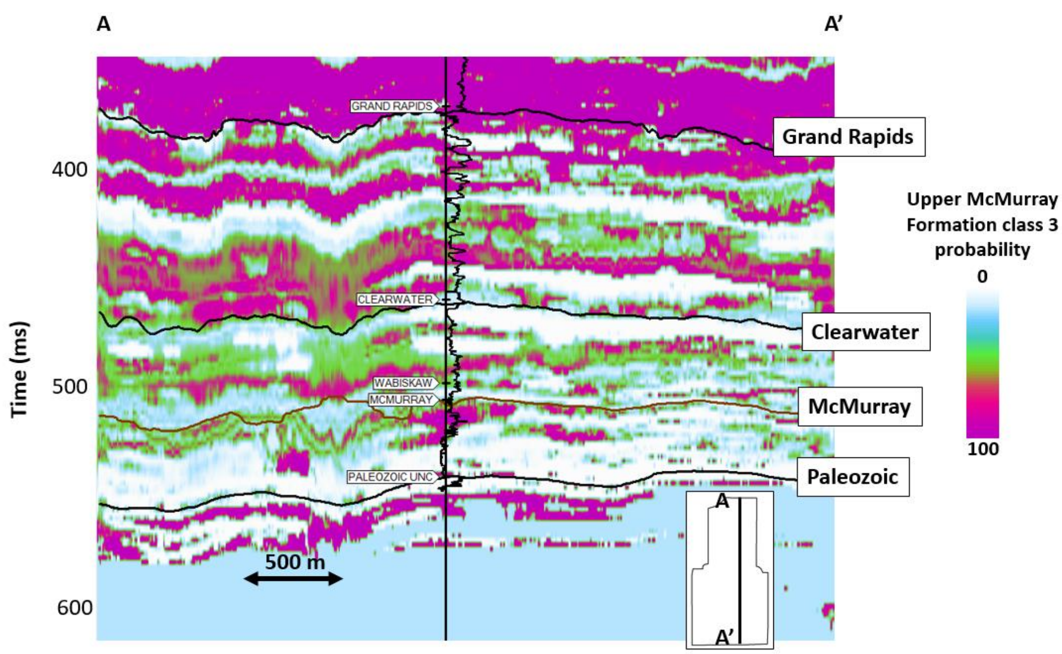

Figure 5-57. Cross section through class 2 probability volume with superposed gamma ray log.

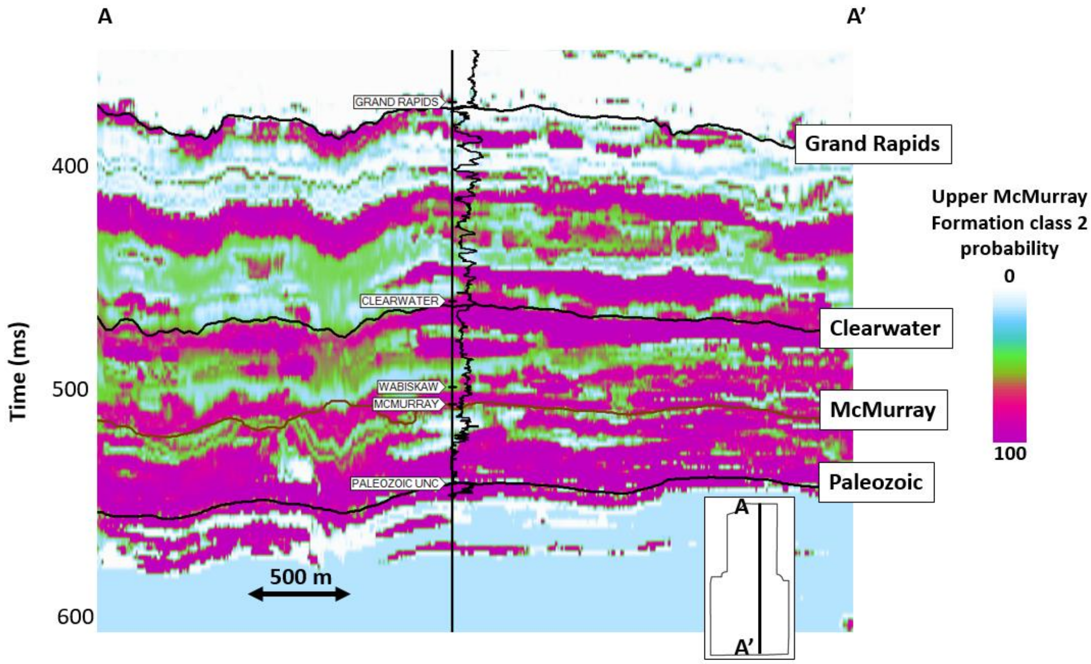

Figure 5-58. Cross section through class 3 probability volume with superposed gamma ray log.

5.6 Discussion

Many different inversion and higher order calculations from seismic data were made to study the zone of interest. Post-stack PP impedance inversion, the simplest of these processes, was performed first. A strong linear relationship between the P impedance volume and a blind well was found, indicating an accurate inversion result. In the McMurray Formation, good reservoir was correlated to high RMS-impedance. This result provided an effective tool for delineating the best zones for exploration in the project area. It was also found that geologic interfaces were much more apparent on the P impedance sections than the stacked seismic section. Challenging seismic horizon picks on stacked data were made much more easily using the P impedance volume.

Adding complexity to seismic inversion, pre-stack PP inversion was performed after the post-stack inversion analysis. Angle gathers were preconditioned, and an angle dependent wavelet was obtained. Strong linear relationships were found between the pre-stack inversion results and blind well logs, with the exception of density. The density volume had a correlation coefficient of 0.44 when compared to a blind well, implying a weak to moderate linear relationship. The reason for a low accuracy in density inversion was the available source-receiver offsets in the seismic survey. Comparing the pre and post stack P impedance volumes showed that the pre-stack inversion generated better resolution within the McMurray Formation. Internal geometry of the McMurray channel was also better imaged on the pre-stack inversion compared to the post-stack inversion.

The last inversion algorithm used on the 3D seismic data was PP-PS joint inversion. Joint inversion simultaneously inverts the PP and PS seismic data and P impedance, S-impedance and density volumes are output. The blind well quality control crossplots for the joint inversion proved to be better correlated than the pre-stack inversion. Thus the joint inversion outputs were used as the primary volumes going forward.

A straightforward permutation of the joint inversion outputs was used to calculate Poisson's Ratio and Young's Modulus. A correlation between interval RMS Poisson's ratio and Young's modulus does not appear to correlate with any lithological changes in the Clearwater Fm.

Prediction of lithology via the gamma ray response, was done using multiattribute analysis and the PP-PS joint inversion outputs. The linear multiattribute analysis, a least-squares minimization technique, generated a gamma ray volume that when tested against a blind well log had a correlation coefficient of 0.52. The nonlinear multiattribute analysis, a probabilistic neural network, when predicting gamma ray had a blind well correlation coefficient of 0.67. The non-linear prediction tool was more accurate and precise than the linear prediction. It was found that the largest low gamma ray anomalies on an average gamma ray map existed in approximately the location of the McMurray channel and zones with high average P impedance. The probabilistic neural network can also be used to place samples into a class rather than actually predicting the output values. The classification algorithm was accurately able to place each seismic sample into either good reservoir or poor reservoir, based on correlation with well control.

CHAPTER 6: CONCLUSIONS

The bituminous sand deposits of Northeastern Alberta are an immense resource. With 163 billion barrels recoverable (Energy Information Administration, 2015) the majority of oil production growth in Canada will likely come from these reservoirs. In this thesis project, a 3D multicomponent seismic survey was used to study a small non-operated region of the Athabasca Oil Sands. The 17 km^2 3D seismic volume was processed into stacked PP and PS datasets and pre-stack PP gathers. The stacked seismic outputs had regional interpretations made based on correlation with well control. Several inversion and multi-attribute analysis algorithms were applied to the seismic data in order to better understand the lithology of the reservoir and caprock.

6.1 PP-PS seismic data processing

The 3D 3C seismic volume used in this thesis project was acquired in the Athabasca Oil Sands in 2013. Joint seismic data processing was done on the vertical and radial geophone components. Stacked PP and PS seismic sections were generated through the processing. Pre-stack PP seismic data was processed for use in inversion algorithms. The main processing techniques used on the PP seismic data were: geometry and bin assignment, refraction and elevation statics, radial denoise, amplitude corrections, Gabor deconvolution, velocity analysis and NMO correction, residual statics, stacking, PSPI migration and FXY signal enhancement. The PS processing followed a similar flow with some notable exceptions. In the PS processing, inline and crossline geophone components from the field were rotated into radial and transverse components. Instead of source and receiver statics being calculated at the same time, P wave source statics are applied then common receiver stacks are generated to obtain shear wave receiver statics. Additionally in PS processing, asymptotic conversion point and common conversion point binning and stacking must be done. The stacked PP and PS seismic datasets had high signal to noise ratio and regionally extensive reflection horizons present.

6.2 General PP and PS seismic data interpretation

Regionally pervasive reflection horizons were interpreted on the post stack PP and PS seismic data volumes. These events were correlated to well control to correlate tops to the seismic data. On the PP data, good reflection quality was found for the Paleozoic Unconformity, the Clearwater Formation and the Grand Rapids Formation and poorer reflection quality for the

McMurray Formation and the Colorado Group. On the PS data, all events had good reflection quality with the exception of the top of the Colorado Group.

Structure and isochron maps were analyzed for key intervals. It was found that within the main reservoir (McMurray Fm), a structurally high, thick isochron trend existed across the project area from SW to NE. This feature was interpreted as a channel incision and fill. The regional McMurray seismic sequence was found to be truncated through this anomaly on both the PP and PS seismic datasets and clear channel edges were present on PP seismic amplitude stratal slices.

A tool found to be useful in studying the McMurray formation was RMS amplitude mapping. Taking a window on the Upper McMurray and calculating the RMS amplitude in this window showed that the distribution of natural gas could be identified using seismic data. High RMS amplitude values in the Upper McMurray correlated with natural gas presence, and thus interpretation was supported through neutron and density porosity log crossover on well logs.

6.3 Inversion and rock physics

Model-based post-stack PP impedance inversion was the simplest inversion technique applied to the 3D 3C seismic data in this project. An input model, based on the regional seismic interpretation and a good well log was generated and a post-stack wavelet was extracted from the seismic data statistically. Iterative P impedance inversion was performed and it was found that RMS P impedance correlated to the presence of good quality reservoir wells. The P impedance inversion also had more consistent imaging of geological boundaries, allowing for easier horizon picking.

Following the post-stack PP inversion, pre-stack PP inversion was performed. Angle gathers were preconditioned to allow for pre-stack inversion and angle dependent wavelets were extracted from these gathers. The model-based inversion process output density, P and shear impedance volumes. Strong linear relationships were found between the impedance volumes and data from blind well logs; these strong correlations indicate an accurate inversion result. The density volume had a modest correlation to a blind well. The correlation coefficient between the density from inversion and well log density was 0.44. The explanation for having precise inversion results for the impedances but not for the density stems from the available value in the angle gathers. The offsets available were not large enough to accurately recover the amplitude versus offset effects of density. However both the post-stack and pre-stack inversion results showed improved imaging within the McMurray reservoir. The internal geometry of the McMurray channel was much clearer on the impedance volumes than the conventional seismic data. The pre-stack inversion results showed better detail in the McMurray than the post-stack outputs.

PP-PS joint inversion was found to provide the most accurate volumes of P impedance, S impedance and density. These properties were inverted for simultaneously from PP seismic data and PS seismic data registered to PP time. The cross correlations of blind wells were found to be higher for the PP-PS joint inversion than the PP pre-stack inversion.

The geomechanical properties, Poisson's Ratio and Young's Modulus were calculated from the PP-PS joint inversion outputs. The hydrocarbon trap and seal, the Clearwater Formation, was studied using the geomechanical properties. Lithological variation was not found to correlate strongly with changes in geomechanical properties.

Linear and non-linear multiattribute analysis was used to predict gamma ray values from seismic data. Relationships between the PP-PS joint inversion outputs and three well logs were trained. First, a least-squares minimization technique was used to predict gamma ray values directly. A correlation coefficient of 0.52 was found between a blind well log and the least-squares gamma ray volume. It was found that a probabilistic neural network made a better prediction than the linear multiattribute analysis. An improved correlation coefficient of 0.67 between a blind well log and the PNN derived gamma ray value was found. Low gamma ray anomalies, representing good quality reservoir, were present in approximately the position of the Large McMurray channel interpreted on the seismic data. These gamma ray anomalies also correlated with the high P impedance anomalies found in the inversion volumes.

REFERENCES

Aki, K., and Richards, P.G., 1980, Quantitative Seismology – Theory and Methods, W. H. Freeman and Co.

Alberta Geological Survey (2015), Alberta table of formations, Alberta Energy Regulator, URL <http://ags.aer.ca/document/Table-of-Formations.pdf> [Accessed June 6, 2015]

Alford, R.M., 1986, Shear data in the presence of azimuthal anisotropy: Dilley, Texas, SEG Technical Program Expanded Abstracts, 476-479

Alkhalifah, T., 1997, Velocity analysis using nonhyperbolic moveout in transversely isotropic media, Geophysics, Vol. 62, No. 6, 1839-1854

Anderson, R.A., Ingram, D.S., and Zanier, A.M., 1973, Determining fracture pressure gradients from well logs, Journal of Petroleum Technology, SPE 4135

Ando, M., Ishikawa, Y., and Wada, H., 1980, S-wave anisotropy in the upper mantle under a volcanic area in Japan, Nature, Vol. 286, 43-46

Andriashek, L.D., 2003, Quaternary geological setting of the Athabasca Oil Sands (in situ), area, Northeast Alberta, Alberta Energy and Utilities Board, Alberta Geological Survey

Baturin-Pollock, C., Sitek, N., Chan, D., and Hurst, T., 2010, Geology and resource assessment of the Grand Rapids, Southern Cold Lake, Alberta, Canada, Search and Discovery Article #10288, AAPG

Bondár, I., 1992, Seismic horizon detection using image processing algorithms, Geophysical Prospecting, Vol. 40, No. 7, 785-800

Bott, R., 1999, Our petroleum challenge, sixth edition, Canada's oil and gas industry, Petroleum Communication Foundation

Castagna, J.P., Batzle, M.L., and Eastwood, R.L., 1985, Relationships between compressional-wave and shear-wave velocities in clastic silicate rocks: Geophysics, 50, 571-581

Chase, M.K., 1992, Random noise reduction by FXY prediction filtering, Exploration Geophysics, Vol. 23, No. 1 51-56

Chopra, A., and Sharma, R. K., 2016, Synthetic seismograms for PS seismic data, Search and Discovery Article # 41793, AAPG

Cooke, D.A., and Schneider, W.A., 1983, Generalized linear inversion of reflection seismic data, Geophysics, Vol. 48, No. 6, 665-676

Cox, M., 1999, Static Corrections for Seismic Reflection Surveys, Society of Exploration Geophysicists

Crude oil forecast, markets & transportation, 2015, Canadian Association of Petroleum Producers

Drees, N.C.M., 1994, Devonian Elk Point Group of the Western Canada Sedimentary Basin, Geological Atlas of the Western Canada Sedimentary Basin, Canadian Society of Petroleum Geologists and Alberta Research Council, Chapter 10

Engineering Toolbox, Elastic properties and Young's Modulus for some materials, Retrieved 2012-01-06

Fenton, M.M., Schreiner, B.T., Nielsen, E., and Pawlowicz, J.G., 1994, Quaternary geology of the western plains: Geological atlas of the Western Canada Sedimentary Basin, Canadian Society of Petroleum Geologists and Alberta Research Council, Chapter 26

Fomel, S., and Backus, M.M., 2003, Multicomponent seismic data registration by least squares, SEG Annual Meeting

Gazdag, J., and Sguazzero, P., 1984, Migration of seismic data by phase shift plus interpolation, Geophysics, Vol. 49, No. 2, 124-131

Gazdag, J., 1978, Wave equation migration with the phase-shift method, Geophysics, Vol. 43, No. 7, 1342-1351

Gingras, M., and Rokosh, D., 2004, A brief overview of the geology of heavy oil, bitumen and oil sand deposits, 2004 CSEG National Convention

Glass, D.J., 2010, Clearwater Formation, Lexicon of Canadian Stratigraphy, Volume 4, CSPG, Natural Resources Canada

Glass, D.J., 2009, Wabiskaw Member, Lexicon of Canadian Stratigraphy, Volume 4, CSPG, Natural Resources Canada

Google Maps, 2016, Ganges Delta map. Retrieved from https://www.google.ca/maps/@22.7694397,89.6672185,458903m/data=!3m1!1e3

Gray, F.D., Anderson, P.F., and Gunderson, J.A., 2006, Prediction of shale plugs between wells in heavy oil sands using seismic attributes, Natural Resources Research, Vol. 15, No. 2, 103-109

Gray, F.D., Anderson, P.F., Logel, J., Delbecq, F., Schmidt, D., and Schmid, R., 2012, Estimation of stress and geomechanical properties using 3D seismic data, First Break Technical Article, Volume 30

Gray, F.D., Wagner, K.A., and Naidu, D.J., 2016, 3C-4D locates mobile bitumen in oil sands reservoirs, CSEG Annual Convention abstracts 2016

Greaves, G.N., Greer, A.L., Lakes, R.S., and Rouxel, T., 2011, Poisson's Ratio and modern materials, Nature Materials, Vol. 10

Hampson, D., and Russell, B., 2013, Joint simultaneous inversion of PP and PS angle gathers, CSEG Recorder, Vol. 38, No. 6

Hampson, D., Russell, B., and Bankhead, B., 2005, Simultaneous inversion of pre-stack seismic data, 2005 CSEG National Convention Abstracts

Hampson-Russell, 2016, Introduction to pre-stack inversion, Hampson-Russell Help System, HRS-9/R2.1.1

Hampson-Russell, 2016, Parabolic radon transform theory, Hampson-Russell Help System, HRS-9/R2.1.1

Hardage, B.A., Pendleton, V.A., Simmons, J.L., Stubbs, B.A., and Uszynski, B.J., 1998, 3-D instantaneous frequency used as a coherency/continuity parameter to interpret reservoir compartment boundaries across an area of complex turbidite deposition, Geophysics, Vol. 63, No. 5, 1520-1531

Hayes, B.J.R., Christopher, J.E., Rosenthal, L., Los, G., and McKercher, B., 1994, Cretaceous Mannville Group of the Western Canada Sedimentary Basin: Geological atlas of the Western Canada Sedimentary Basin, Canadian Society of Petroleum Geologists and Alberta Research Council, Chapter 19

Hein, F.J., Langenberg, C.W., Kidston, C., Berhane, H., and Berezniuk, T., 2001, A Comprehensive Field Guide for Facies Characterization of the Athabasca Oil Sands, Northeast Alberta, Alberta Energy and Utilities Board, Alberta Geological Survey

Hein, F.J., Marsh, R.A., and Boddy, M.J., 2008, Overview of the oil sands and carbonate bitumen of Alberta: regional geologic framework and influence of salt-dissolution effects, Search and Discovery Article # 10144

Henley, D.C., and Margrave, G.F., 2001, A ProMAX implementation of nonstationary deconvolution, CREWES Research Report, vol. 13, 203-222

Henley, D.C., 2011, Now you see it, now you don't: a radial trace filtering tutorial, CREWES Research Report, Volume 23

Herwanger, J.V., Bottrill, A.D., and Mildren, S.D., 2015, Uses and abuses of the brittleness index with applications to hydraulic stimulation, Unconventional Resources Technology Conference 2015

Ion, D., and Galbraith, M., 2011, A practical approach for estimating receiver statics in 2D/3C seismic data processing, 2011 CSPG CSEG CWLS Convention Abstracts

Isaac, J.H., 1996, Seismic methods for heavy oil reservoir monitoring, Ph.D. thesis, University of Calgary, Department of Geology and Geophysics

IUPAC, 1997, Modulus of elasticity, Compendium of Chemical Terminology, 2nd Edition,

Kelly, B.M., 2012, Processing and interpretation of time-lapse seismic data from a heavy oil field, Alberta, Canada, Ph.D. thesis, University of Calgary, Department of Geology and Geophysics

Krief, M., Garat, J., Stellingwerff, J., and Ventre, J., 1990, A petrophysical interpretation using velocities of P and S waves (full waveform sonic): The Log Analyst, 31, No. 6

Lawton, D.C., and Howell, C.E., 1992, P-SV and P-P synthetic stacks, Society of Exploration Geophysicists, SEG Annual Meeting, New Orleans, Louisiana

Leckie, D.A., Bhattacharya, J.P., Bloch, J., Gilboy C.F., and Norris, B. 1994, Cretaceous Colorado/Alberta Group of the Western Canada Sedimentary Basin: Geological atlas of the Western Canada Sedimentary Basin, Canadian Society of Petroleum Geologists and Alberta Research Council, Chapter 20

Margrave, G.F., Gibson, P.C., Grossman, J.P., Henley, D.C., and Lamoureux, M.P., 2004, Gabor deconvolution: theory and practice, EAGE 66th Conference and Exhibition, Paris, France

Margrave, G.F., 2006, Methods of seismic data processing, Geophysi cs 557 Course Lecture Notes, The Department of Geology and Geophysics, University of Calgary

Masson, R., and Remillard, B., 1995, Alberta's new oil sands royalty system, International Conference of Petroleum Fiscal Regimes Proceedings

MEG Energy Corp., 2016, Stead-Assisted Gravity Drainage, Retrieved from: http://www.megenergy.com/operations/steam-assisted-gravity-drainage-sagd, June 20, 2016

Mehrotra, A. K., and Svrcek, W.Y., 1986, Viscosity of compressed Athabasca bitumen, The Canadian Journal of Chemical Engineering, Vol. 64, 844-847

Mei, S., Bechtel, D.J., Grobe, M., and Palombi, D., 2015, Paleotopographic reconstruction and subcrop geological mapping of the Sub-Cretaceous Unconformity in central Alberta: Methodology and Results, Alberta Energy Regulator, Alberta Geological Survey

Montmayeur, H., and Graves, R.M., 1986, Prediction of static elastic/mechanical properties of consolidated and unconsolidated sands from acoustic measurements: correlations, Society of Petroleum Engineers, SPE 15644

Nickel, M., and Sonneland, L., 2004, Automated PS to PP event registration and estimation of a high-resolution V_p-V_s ratio volume, SEG International Exposition and 74th Annual Meeting

Oldale, H.S., and Munday R.J., 1994, Devonian Beaverhill Lake Group of the Western Canada Sedimentary Basin: Geological atlas of the Western Canada Sedimentary Basin, Canadian Society of Petroleum Geologists and Alberta Research Council, Chapter 11

Pemberton, S.G., Flach, P.D., and Mossop, G.D., 1982, Trace fossils from the Athabasca Oil Sands, Alberta, Canada, Science, Vol. 217, Issue 4562, 825-827

Rho, J.Y., 1993, Young's Modulus of trabecular and cortical bone material: ultrasonic and microtensile measurements, Journal of Biomechanics, Vol 26, No. 2, 111-119

Rider, M., and Kennedy, M., 2011, The Geological Interpretation of Well Logs, Third Edition, Rider-French Consulting Limited

Ronen, J., and Claerbout, J.F., 1985, Surface-consistent residual statics estimation by stack power maximization, Geophysics, Vol. 50, No. 12, 2759-2767

Schafer, A.W., 1992, A comparison of converted-wave binning methods using a synthetic model of the Highwood Structure, Alberta, CREWES Research Report, 4

Schneider, C.L., Mei, S., Grobe, M., and Haug, K., 2012, Beneath the oil sands: stratigraphy and structural features of the Devonian of Northeast Alberta, GeoConvention 2012: Vision

Souraki, Y., Ashrafi, M., Karimaie, and Torsaeter, O., 2012, Experimental analyses of Athabasca bitumen properties and field scale numerical simulation study of effective parameters on SAGD performance, Department of Petroleum Engineering and Applied Geophysics, Norwegian University of Science and Technology

Stewart, R.R., Gaiser, J.E., Brown, R.J., and Lawton, D.C., 1999, Converted-wave seismic exploration: a tutorial, CREWES Research Report, 11

Stewart, R.R., Gaiser, J.E., Brown, R.J., and Lawton, D.C., 2002, Converted-wave seismic exploration: methods, Geophysics, Vol. 67, No.5, 1348-1363

Stewart, R.R., Gaiser, J.E., Brown, R.J., and Lawton, D.C., 2003, Converted-wave seismic exploration: applications, Geophysics, Vol. 68, No.1, 40-57

Taner, M.T., and Koehler, F., 1969, Velocity spectra – digital computer derivation and applications of velocity functions, Geophysics, Vol. 34, No. 6, 859-881

Taner, M.T., Koehler, F., and Sheriff, R.E., 1979, Complex seismic trace analysis, Geophysics, Vol. 44, No. 6, 1041 -1063

Tessmer, G., and Behle, A., 1988, Common reflection point data-stacking technique for converted waves, Geophysical Prospecting 36, 671-688

Todorivic-Marinic, D., Gray, D., and Dewer, J., 2015, Strategies to fill in the details for an oil sands reservoir: Kinosis example: CSEG Recorder, January 2015, 18-24

Tsvankin, I., 1997, Reflection moveout and parameter estimation for horizontal transverse isotropy, Geophysics, Vol. 62, No. 2, 614-629

Vigrass, L.W., 1968, Geology of Canadian heavy oil sands, AAPG Bulletin, Vol. 52, Issue 10, 1984-1999

Willmer, T., and Quinn, G., 2015, Characterization of the Albian Lower Grand Rapids Formation, Cold Lake, Alberta, CSEG Recorder, Vol 40. No. 1

Yilmaz, O., 2001, Seismic data analysis: processing, inversion and interpretation of seismic data, Second Edition, Society of Exploration Geophysicists